

Modeling and Simulation of the Interaction Between Particles and Pulmonary Mucus

Dissertation zur Erlangung des Grades des Doktors der Naturwissenschaften
der Naturwissenschaftlich-Technischen Fakultät
der Universität des Saarlandes

Matthias Ernst

Saarbrücken

-2017-

Dissertation eingereicht am: 02.02.2017

1. Gutachter: Prof. Dr. Claus-Michael Lehr

2. Gutachter: Prof. Dr. Stefan Diebels

Tag des Kolloquiums: 01.06.2017

Dekan: Univ.-Prof. Dr. Guido Kickelbick

Berichterstatter: Prof. Dr. Claus-Michael Lehr

Prof. Dr. Stefan Diebels

Vorsitz: Prof. Dr. Christian Wagner

Akad. Mitarbeiter: Dr. Thomas John

Eidesstattliche Versicherung

Hiermit versichere ich an Eides statt, dass ich die vorliegende Arbeit selbstständig und ohne Benutzung anderer als der angegebenen Hilfsmittel angefertigt habe. Die aus anderen Quellen oder indirekt übernommenen Daten und Konzepte sind unter Angabe der Quelle gekennzeichnet. Die Arbeit wurde bisher weder im In- noch im Ausland in gleicher oder ähnlicher Form in einem Verfahren zur Erlangung eines akademischen Grades vorgelegt.

Ort, Datum

(Unterschrift)

1 Abstract

The aim of this thesis was to simulate the interaction of particles with the protective barrier of the lung, the mucus layer. Beginning with different diffusion models to simulate the particle movement inside the mucus network, we also measured and compared the rheological properties of mucus from different organs of the same species. Using the results from these experiments, we simulated the deformation of the mucus structure. We used computational fluid dynamic (CFD) methods to simulate the air flow in the upper airways during inhalation and to calculate the kinetic energy of aerosol particles, which are transported by the convective air flow to deposit at the mucus layer. Finally, we did some experiments with fluorescence recovery after photobleaching (FRAP) methods to visualize the diffusion of particles in mucus and also the structure of this biological barrier. By applying our model, we were able to determine the diffusivity of particles in complex, heterogeneous materials, only by assuming few parameters. So, in this thesis we showed various models to simulate the interaction, mainly the diffusion, of particles with pulmonary mucus, beginning with the inhalation and deposition of the particles in the lung and at the mucus layer.

Das Ziel dieser Thesis war die Simulation der Interaktion von Partikeln mit der schützenden Barriere der Lunge, der Mukusschicht. Angefangen mit verschiedenen Diffusionsmodellen um die Partikelbewegung innerhalb des Mukus-Netzwerks zu simulieren, haben wir auch die rheologischen Eigenschaften von Mukus aus verschiedenen Organen der gleichen Spezies gemessen und verglichen. Wir simulierten die Deformation der Mukus-Struktur mithilfe der Ergebnisse dieser Experimente. Wir benutzten CFD Methoden um den Luftstrom in den oberen Atemwegen während der Inhalation zu simulieren und um die kinetische Energie von Aerosol-Partikel zu berechnen, die durch den konvektiven Luftstrom transportiert werden um sich auf der Mukusschicht abzusetzen. Letztendlich führten wir noch Experimente mit FRAP Methoden durch, um die Diffusion von Partikel in Mukus und auch die Struktur dieser biologischen Barriere darzustellen. Durch die Anwendung unseres Modells sind wir in der Lage die Diffusivität von Partikeln in komplexen, heterogenen Materialien, alleine mit der Annahme weniger Parameter zu bestimmen. In dieser Thesis zeigten wir unterschiedliche Modelle um die Interaktion, hauptsächlich die Diffusion, von Partikeln mit pulmonalem Mukus zu simulieren, angefangen bei der Inhalation und Ablagerung von Partikeln in der Lunge und auf der Mukusschicht.

1 Abstract	1
2 Table of Contents	2
3 Introduction	5
3.1 Background and significance of the research	5
3.2 State of research and rising problems	6
3.3 Aim of the studies	7
3.4 Workflow and structure of the thesis	8
4 Modeling and Simulation of Particle Diffusion in Mucus	9
4.1 Modeling particle diffusion in mucus and transient subharmonic behavior based on permeable membranes	9
4.1.1 Introduction	9
4.1.2 Model & numerical methods	15
4.1.3 Results & Discussion	31
4.2 A model to predict particle diffusion in mucus for short and long time limits	40
4.2.1 Introduction	40
4.2.2 Model & experimental findings	41
4.2.3 Results & Discussion	43
4.3 Modeling and Simulation of Fickian diffusion based on concentration gradients and comparison with a Brownian diffusion model	49
4.3.1 Introduction	49
4.3.2 Fickian and Brownian diffusion models	49
4.3.3 Results & Discussion	52
4.4 Conclusions	62

5 Mechanical and Rheological Properties of Mucus	64
5.1 Introduction	64
5.1.1 Macro- and microrheology of mucus	64
5.1.2 Viscoelastic properties of mucus	64
5.2 Macro- and microrheological properties of native porcine respiratory and intestinal mucus	66
5.2.1 Material & Methods	66
5.2.2 Results & Discussion	67
5.3 Calculation of the necessary deformation energy to expand the mucus pores	73
5.3.1 Computation of the deflection and deformation of mucin fibers	73
5.3.2 Brownian diffusive energy and comparison with the necessary deformation energy	80
5.4 Conclusions	81
6 Computational Fluid Dynamics (CFD) Simulations of the Air Flow in the Human Lung	82
6.1 Introduction	82
6.1.1 Structure of the human lung	82
6.1.2 Development of lung models	83
6.1.3 Particle deposition processes	86
6.1.4 Computational Fluid Dynamics (CFD)	87
6.2 Computation of the velocity profile and the kinetic energy	89
6.2.1 Velocity profile	89
6.2.2 Calculation of the kinetic energy and comparison with the necessary deformation energy	92
6.3 Conclusions	96

7	Fluorescence Recovery after Photobleaching (FRAP) for Studying Particle-Mucus Interactions	97
7.1	Introduction	97
7.2	Materials & Methods	98
7.3	Imaging and Evaluation	99
7.3.1	Imaging of the particle-mucus interaction	99
7.3.2	Evaluation of the particle diffusivity in mucus	100
7.4	Conclusions	105
8	Assumptions and Hypotheses	106
9	Summary and Outlook	108
10	References	111
11	List of Abbreviations	116
12	List of Tables	119
13	List of Figures	120
14	List of Equations	123
15	Publications and Presentations	125
16	Curriculum Vitae	126
17	Acknowledgments	127

3 Introduction

3.1 Background and significance of the research

The interface between the atmospheric air and the blood is built by epithelial cells. To protect these from foreign substances, such as viruses, bacteria, and dust, they are covered by a layer of mucus. The aim of the drug application by aerosols and particulate systems through the lungs is the non-invasive uptake of drugs and therapeutics by the lung epithelial. Thereby, the protective barriers, thus the mucus layer, have to be overcome by the drug-loaded particles.

In the past, predominantly invasive drug delivery methods, such as injection, were used to administer drugs into the systemic circulation of humans. So, the focus on research in the last years was to develop novel delivery systems to achieve a non-invasive drug administration by overcoming biological barriers, e.g. the skin or the respiratory tract. In particular, the lung became a highly promising target for drug carrier systems, due to the relatively large surface and low enzymatic activity. Beside these advantages, drug administration at the lung surface also can be non-toxic and well tolerated by patients, who will be able to inhale ideally biodegradable drug carrier systems instead of getting them injected. Otherwise, there are protective mechanisms in the lung, which prevent a longer residence of deposited aerosol particles at the lung epithelia by rather effective clearance processes, such as the mucociliary clearance [1,2].

3.2 State of research and rising problems

Several groups deal with the experimental determination of the diffusivity of different sized and coated particles in mucus. Their studies lead to a better knowledge of the treatment of mucus and particles to achieve an efficient drug delivery through biological barriers. Nevertheless, these experiments are often very expensive and time-consuming, and they have to consider ethical aspects in yielding sufficient results. Furthermore, there are several restrictions in the experimental settings, such as the limited time range in particle tracking experiments. However, the investigation and improvement of drug delivery processes in the lung is still a current topic in research and aim of this work. Subsequently, the following chapters deal with different processes, which describe the inhalation, deposition and diffusion of particles and their interaction with the mucus layer in the upper airways. In addition, mucus from different organs of one mammalian species has also been investigated, concerning its rheological properties.

3.3 Aim of the studies

Aim of the studies is on the one hand to develop preferably realistic diffusion models to simulate diffusive transport processes of particles, overcoming the mucus barrier and finally to compare the simulated results with recently performed experimental studies. So, by applying these models, time-consuming and expensive experiments should be replaced by simulations, which are as realistic as possible. To achieve comparable simulation results, stochastic differential equations (SDE), partially differential equations (PDE), and analytical approximations will be used. By numerically solving these differential equations and applying analytical approximating equations, the Brownian diffusion, which mainly describes the random walk of particles, can be simulated. Furthermore, the Fickian diffusion, which is based on concentration gradients and comparable to heat transfer problems, has been simulated, using the Finite Element Method (FEM), and finally compared with Brownian diffusion. By assuming as few parameters as possible, our presented models are able to predict the diffusivity of particles in mucus for a broad range of time scales.

On the other hand, the deposition, more precisely the convective flow, of aerosol particles in the lung during inhalation will be simulated by using computational fluid dynamics (CFD). To investigate and simulate the interaction between these particles and the mucus, besides the diffusion, also the mechanical and rheological properties of mucus will be determined. The results of these simulations will be used to simulate deformation processes of the mucus after the particle impact. Finally, we will be able to determine the probability of a particle to mechanically penetrate the mucus layer after deposition and to pass this layer by diffusion processes. Subsequently, also the time of a particle needed to pass through the mucus and in particular, the necessary requirements on the particle and mucus properties will be determined. The last section of this work deals with the experimental investigation of particle-mucus interactions by a novel fluorescence method to achieve some experimental diffusion parameters and to compare these with our simulated results.

3.4 Workflow and structure of the thesis

In the first part of this thesis the Brownian diffusion of particles in mucus will be simulated by numerical and analytical methods, based on permeable membranes, and compared with some experimental results from literature. In addition, we develop models to simulate the Fickian diffusion of particles in mucus, based on concentration gradients.

The second part of the thesis deals with the rheological and mechanical properties of mucus. In this part, the rheological properties of porcine mucus from different organs will be examined by different methods, e.g. optical tweezer, and the mechanical deformation of mucus due to the aerosol particle impact will be simulated.

In the third part, the flow profile and deposition of the inhaled aerosol particles in the upper airways of the lung will be simulated. The resulting kinetic energy of the inhaled particles and their Brownian diffusive energy will then be compared with the necessary deformation energy of mucus to investigate the possibility of the particles to penetrate the mucus layer by deposition (impaction) and diffusion.

Finally, the last part of this thesis deals with a novel method to visualize the interaction between mucus and particles, using the fluorescence recovery after photobleaching (FRAP).

To conclude the thesis, we will declare the necessary parameters, which are needed to describe the transport of particles to the lung epithelial cells, beginning with the inhalation and deposition of aerosol particles, and ending with the mechanical and diffusive processes in the mucus layer. We will determine the role of the mucus structure as well as the role of physical and chemical particle properties for the non-invasive administration of drugs and therapeutics.

4 Modeling and Simulation of Particle Diffusion in Mucus

4.1 Modeling particle diffusion in mucus and transient subharmonic behavior based on permeable membranes

Parts of this chapter have been published in Ernst, M., T. John, M. Günther, C. Wagner, U. F. Schäfer, and C.-M. Lehr (2017). A Model for the Transient Subdiffusive Behavior of Particles in Mucus. The Biophysical Journal 112:172-179.

4.1.1 Introduction

Biological barriers are crucial in protecting our body from environmental influences. Well-known outer barriers are intestinal, pulmonary, nasal, buccal, cervico-vaginal and dermal barriers. Except for the dermal barrier, all these are covered by a mucus layer, providing an additional barrier to the epithelial cell layer. For particle-based drug delivery systems, this mucus layer generates an extra challenge. Mucus is a complex, heterogeneous polymer-scaffold with viscoelastic properties. It consists of mainly mucins, which are large semi-flexible glycoproteins, and of an interstitial fluid with low viscosity (see Fig. 1). Either these glycoproteins are dissolved or membrane bound. Thus, solid drug delivery systems and penetration of particulate matter, such as viruses, bacteria, and dust are affected. The main component of mucus is the interstitial fluid, which essentially consists of water, depending on its site of secretion. Moreover, thickness, composition and rheological properties of the mucus layer depend on physiological conditions, regions, species, and functions of the respective organs. However, in the bronchial regions of the lung, pulmonary mucus is present, where its function is the clearance of particulate xenobiotics, mucosal insults, water balance, ion transport, and ion regulation. [1-12].

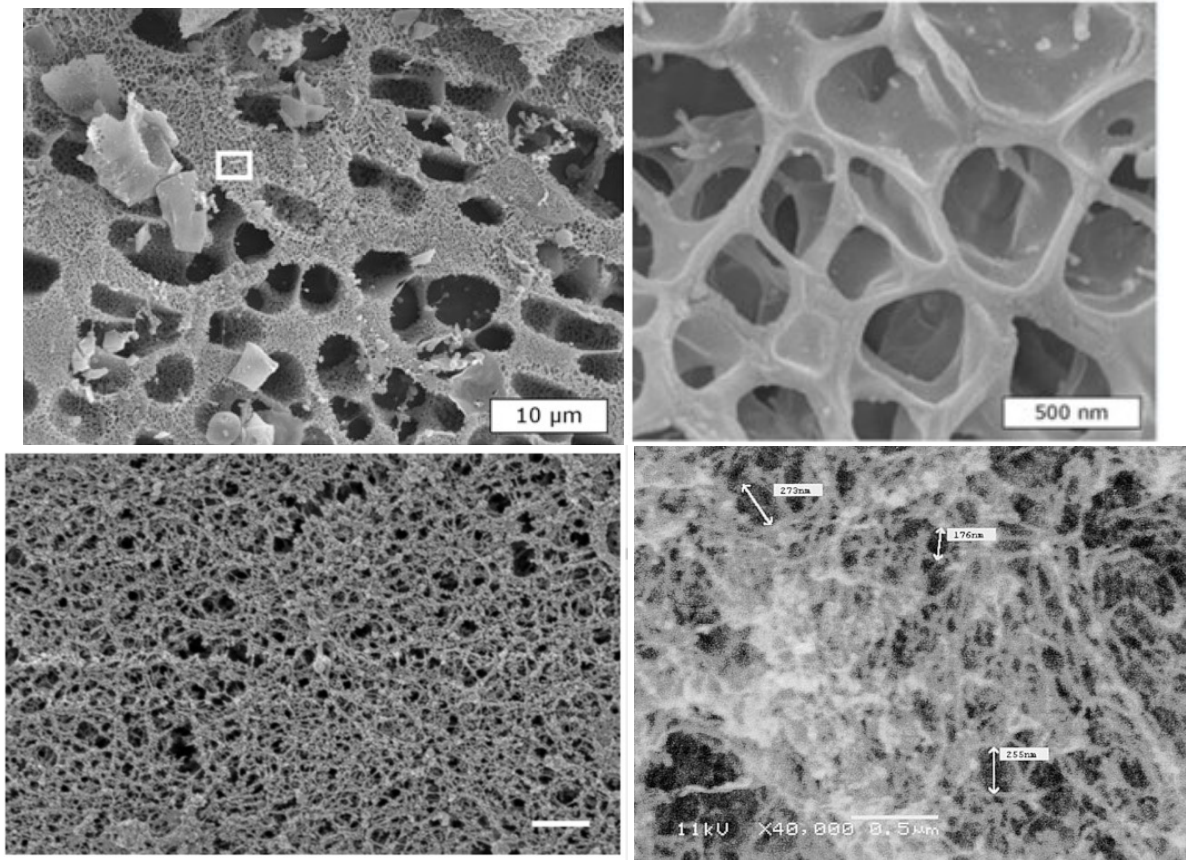


Figure 1: Scanning electron microscopic image of horse pulmonary mucus, Kirch et al. [8] (upper Figures), human airway mucus, Schuster et al. [11] (lower Figure, left side), and sputum from cystic fibrosis patients, Sanders et al. [13] (lower Figure, right side). Each scale bar in the lower Figures represents 500 nm.

Mucus as a complex, biological system can be a dynamic barrier, due to the continuously secretion and translocation of the mucus layer, it can be an interactive barrier, due to various interactions with foreign substances, and it naturally can be a steric barrier, similar to a size exclusion filter. In particular the steric barrier property of mucus, which leads to a size excluding effect, will be mainly considered in this work. As shown in Fig. 2, there are obvious differences in the steric and the interactive barrier properties: the steric barrier is size-dependent, whereas the interactive barrier depends on the surface properties, e.g. chemical or electrostatic properties, of the mucins as well as that of the particles [10]. Actually, our model combines these barrier models, as the Brownian diffusion will depend on the particle size, but the presented diffusion model also depends on different other parameters, referring to physical-chemical properties, as described later in this work.

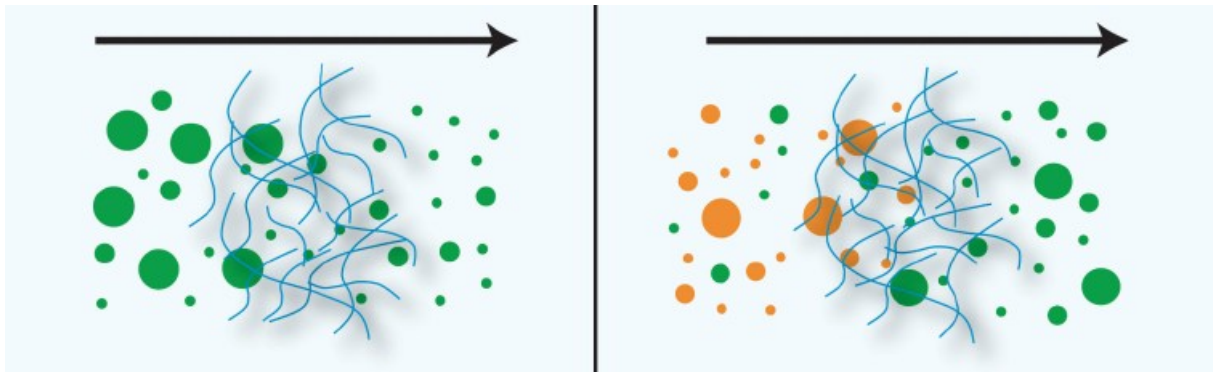


Figure 2: Steric (left) and interactive (right) barrier properties of mucus, Boegh et al. [10]. The interaction in the right Figure is based on the surface properties, e.g. chemical or electrostatic properties, of mucus and the particles.

In Figure 3 the micro-, the meso- and the macroscopic diffusion types are shown, where the former is described by the particle diffusion within a mucus cell (A) and the latter is described by the deformation and reorientation of the mucin fibers due to the particle movement (C). The mesodiffusion is described by a particle motion within the mucus cells and with frequent passages of the particles into neighbored cells (B).

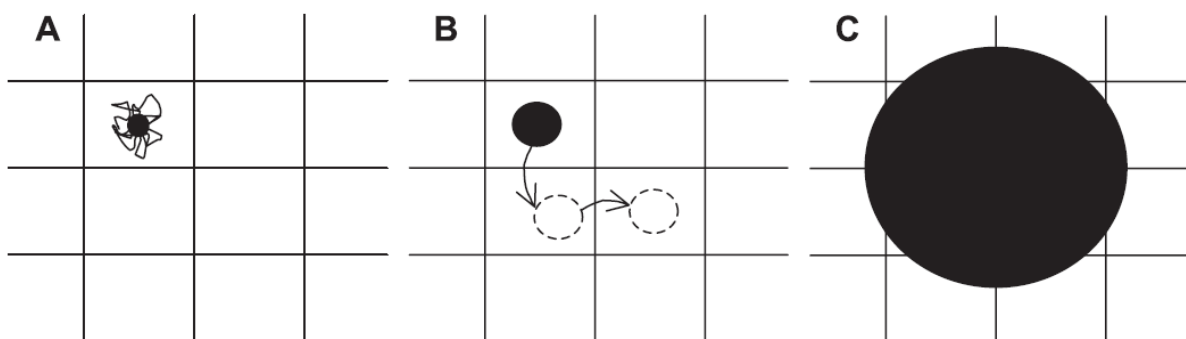


Figure 3: Different types of diffusion, which are the microscopic (A), the mesoscopic (B), and the macroscopic (C) diffusion of particles in a mucus network, Suh et al. [14].

Figure 4 shows the selectivity of mucus as a barrier to small particles, moving more or less freely inside the mesh, to particles, interacting with the mucin fibers, and to large particles, being trapped in the mucus mesh [6]. All these mentioned effects will be included in the presented mucus model.

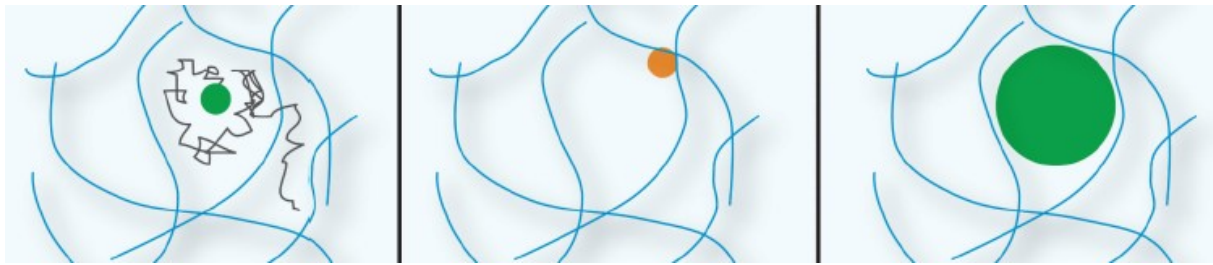


Figure 4: Free movement of particles (left), interaction of particles with mucin fibers (middle), and trapped particles (right), Lieleg et al. [6].

The average thickness of the mucus layer in the bronchial regions is about $55\text{ }\mu\text{m}$ [7]. Naturally, the size of particles and mucus pores, the viscosity of the interstitial fluid and the entire mucus-structure are equally important factors for particle diffusion. The macrorheological viscosity of sputum from cystic fibrosis patients is about 70 Pas at a shear rate of 0.1 s^{-1} [14], and the amplitude of the complex viscosity at $\omega = 1\text{ rad s}^{-1}$ of pulmonary mucus from humans without lung disease is about 10 Pas [11]. In contrast, the microrheological viscosity of the interstitial fluid is similar to that of water, typically in order of few mPas [14].

To reduce systemic side effects by the therapy of bronchial diseases, e.g. cystic fibrosis, local applications of drug delivery systems are desirable. To better overcome the biological barriers in the lung, encountered by inhaled pharmaceuticals, functionalized and non-toxic nanocarriers can be used. Inspired from viruses, nanosized particles with neutrally charged coatings such as polyethylene glycol (PEG) can efficiently penetrate the mucus layer [1,2,11,12]. Currently, quite a few data from studies on different particle systems are available. Particularly, biodegradable particle systems, such as poly-lactic-co-glycolic acid (PLGA) particles are often used, because they are generally regarded as safe (GRAS) [15]. In some cases, particles, which are able to link with the mucin fibers have been developed to extend the time range of being connected to the mucus layer and thus to increase the residence time in this layer. So, the probability of passing the mucus layer will also increase, assuming the clearance effects being reduced. Otherwise, coating particles with PEG has been commonly used to improve the diffusivity of particles in mucus due to the elimination of the particle surface charges and subsequently vanishing attractive and repulsive effects between the mucin fibers and the particles [7,11,12,16-20]. Furthermore, lipid and polymer particles showed an increase of the antimicrobial efficacy in biofilms [21]. To renew the mucus layer, the epithelium is covered by cilia and a low viscous periciliary layer, which is usually treated as watery fluid. The cilia on top of the epithelium reach into the mucus layer by passing the periciliary layer in between. Due to the low viscosity of the periciliary layer, the translocation

of the mucus layer out of the lung is enabled by the propulsion of the cilia (see Fig. 5). Mucus is continuously transported out of the lung through the aligned movement of the cilia, and this process is called the mucociliary clearance. Besides the mucociliary clearance, which requires about 10 min - 20 min in the main bronchi to renew the mucus layer, mucus can also be cleared by enzymatic or bacterial degradation [2,4,7,22]. Unfortunately, also drug carriers, which are trapped in the mucus maybe removed before passing the mucus layer and reaching the epithelial cells [see Fig. 5 (A)]. Otherwise, patients with lung diseases, e.g. cystic fibrosis (CF), suffer from a significantly reduced mucociliary clearance, due to higher viscosities -up to 100000times higher than that of water- and a denser mucus mesh size [7,13,14,19,23-25]. This effect leads to a reduced translocation of the mucus and therewith to a higher risk of infection, but also to a higher probability for drug carriers to stay within the mucus layer. The reduced diffusivity of particles and the increased clearance time for mucus from CF patients come with a different passage time, compared to mucus from healthy lungs, which will be shown in posterior sections.

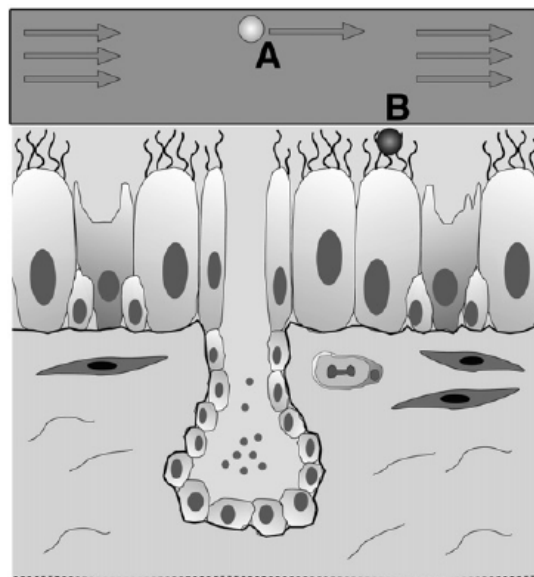


Figure 5: Transport mechanism of particles in the mucus layer during the mucociliary clearance by the cilia propulsion,
Kirch et al. [22].

Several studies deal with the penetration and passing of particles through biological barriers (see Table 1). Not only mucus, but also biofilms or synthetic hydrogels have been investigated, regarding their permeability for different coated and sized particles. Table 1 also shows the measured diffusion coefficients, which will be compared to results from our simulations later in this work.

Table 1: Exemplary studies on particle interactions with different biological barriers. Different particle coatings, sizes, and materials, as well as different biological barriers were used to determine various diffusion coefficients.

Ref.	Material	Coating	Size [μm]	Barrier	Diff. [μm ² s ⁻¹]
[20]	PS	COOH	1.24	PoGaMu	0.003
[20]	PS	PEG(c)	1.06	PoGaMu	0.03
[20]	PS	PEG(a)	1.28	PoGaMu	0.009
[20]	PS	NH3	1.12	PoGaMu	0.004
[16]	PS	-	0.11	HuCVMu	0.0001
[16]	PS	-	0.22	HuCVMu	0.001
[16]	PLGA	-	0.15	HuCVMu	0.0009
[16]	PSA	-	0.2	HuCVMu	0.0005
[16]	PSA	PEG	0.17	HuCVMu	0.2
[18]	PS	COOH	0.11	HuCVMu	0.0001
[18]	PS	PEG	0.12	HuCVMu	0.002
[18]	PS	COOH	0.22	HuCVMu	0.0009
[18]	PS	PEG	0.23	HuCVMu	0.4
[18]	PS	COOH	0.52	HuCVMu	0.0002
[18]	PS	PEG	0.53	HuCVMu	0.2
[19]	PS	PEG(2)	0.1	BM-biofilm	3.2
[19]	PS	PEG(5)	0.1	BM-biofilm	3.1
[19]	PS	COOH	0.1	BM-biofilm	0.2
[19]	PS	DMEDA	0.1	BM-biofilm	0.3
[19]	PS	PEG(2)	0.2	BM-biofilm	1.7
[19]	PS	PEG(5)	0.2	BM-biofilm	1.7
[19]	PS	COOH	0.2	BM-biofilm	0.1
[19]	PS	DMEDA	0.2	BM-biofilm	0.1
[19]	PS	PEG(2)	0.1	HuCFsputum	0.7
[19]	PS	PEG(5)	0.1	HuCFsputum	0.9
[19]	PS	COOH	0.1	HuCFsputum	0.2
[19]	PS	DMEDA	0.1	HuCFsputum	0.2
[19]	PS	PEG(2)	0.2	HuCFsputum	0.5
[19]	PS	PEG(5)	0.2	HuCFsputum	0.5
[19]	PS	COOH	0.2	HuCFsputum	0.3
[19]	PS	DMEDA	0.2	HuCFsputum	0.1
[19]	PS	PEG(5)	0.1	PA-biofilm	2.8
[19]	PS	DMEDA	0.1	PA-biofilm	0.04
[11]	PS	COOH	0.09	HuReMu	0.01
[11]	PS	PEG	0.1	HuReMu	0.2
[11]	PS	COOH	0.19	HuReMu	0.001
[11]	PS	PEG	0.22	HuReMu	0.05
[11]	PS	COOH	0.51	HuReMu	0.0009
[11]	PS	PEG	0.55	HuReMu	0.002

Here, PS means polystyrene, PSA means polysebacic acid, and DMEDA means N,N-dimethylethylenediamine. PEG(2) and PEG(5) is polyethylene glycol with a molecular weight of 2 kDa and 5 kDa, respectively. PEG(a) and PEG(c) is amine-modified PEG and carboxyl-modified PEG, respectively. PoGaMu is porcine gastric mucus, HuCVMu is human cervico vaginal mucus, BM is burkholderia multivorans, PA is pseudomonas aeruginosa, HuCFsputum is sputum from human CF-patients, and HuReMu is human respiratory mucus.

As shown, the diffusivity of particles depends on several parameters, such as the particle size and the properties of the biological barrier, but also on the coating and the surface treatment of the particles.

4.1.2 Model & numerical methods

The Figure 1 suggests a model of mucus, which is based on a porous structure of Newtonian fluid-filled random-sized cells (cavities) with apertures of various sizes. In order to simplify the system to a simple cubic lattice of cavities with connecting apertures, the mucus is characterized by a mean cavity extension L and a mean aperture diameter [see Fig. 6(A)].

Therefore, L refers to the edge size of one cell (cavity) in the cubic lattice of cavities, respectively the distance between the cavity interfaces. Such system is still anisotropic in the sense of the 3D diffusion equation, due to the fact that the boundary conditions are not separable. Hence, the details of the scaffold structure are condensed by the "boundary homogenization" method assuming permeable membranes in all spatial directions, and quantified by a certain permeability of the membranes for the particles [see Fig. 6(B) and (C)].

In this work, we modify the model from Dudko et al. [26, 27] and link it to data of particle diffusion experiments in mucus [11, 14]. We adapt model parameters for comparison to obtain physically interpretable quantities. In addition, to support the model, another very efficient way of simulating particle trajectories through permeable membranes is introduced. That approach is based on the simulation of particle trajectories in presence of Robin boundaries. In this section, we recover the model from Dudko et al. [26, 27] and discuss the assumptions of condensing the scaffold structure to simulate diffusion in an environment with periodic permeable membranes. Additionally, we present a heuristic approximation, which yields a simple analytic expression for the $MSD(\tau)$ as the function of only a few physical interpretable parameters, related to the physical properties of the mucus and the immersed particles. To justify the approximated formula, we introduce a simulation of Brownian particles in presence of permeable membranes as Robin boundaries. This approach aims to provide a better interpretation of the experimentally achieved data and may contribute new insights for improving the design of particle-based drug delivery systems. Therefore, finally we estimate the maximum particle size to penetrate the mucus layer by passive Brownian

motion. Further thoughtful experimental improvements and data analysis approaches are discussed in the conclusion.

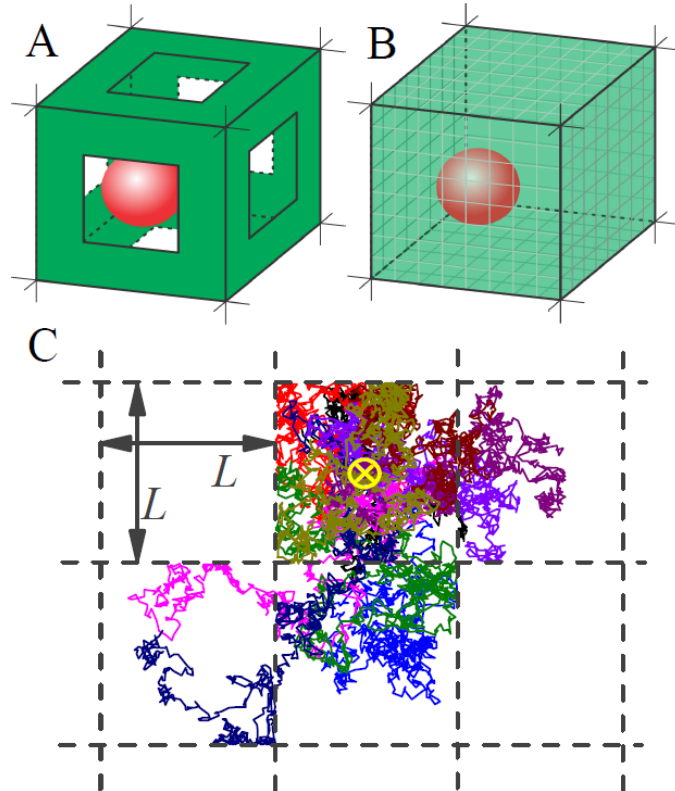


Figure 6: (A) A three-dimensional (3D) representation of a unit cell as single cubic cavity with edge size L , and with reflecting walls and apertures, the precursor for the mucus model. The red sphere depicts a tracer particle. (B) Representation of the model using permeable membranes as interfaces. (C) Exemplary trajectories of particles as two-dimensional (2D) projection to visualize the Brownian diffusion inside the cavity and the restricted passing through the membranes, shown as dashed lines. To represent the trajectories, we use the initial position as the center of the cavity, indicated by the yellow cross; otherwise, in the simulations, the initial positions are random.

The simulation of stochastic processes, e.g. the so-called Wiener process, which is used to describe the random walk of a particle, can be done by solving stochastic differential equations (SDE) by numerical methods. The mentioned Wiener process is a stochastic process with the following conditions:

- 1) The mean has to be zero.
- 2) The process is continuous.
- 3) For all $0 = t_0 < t_1 < \dots < t_n$, the random variables $X(t_{i+1}) - X(t_i)$ are independent.
- 4) For all $s < t$, $X(t) - X(s)$ is $N(0, t-s)$ - distributed.

The Wiener process is $N(0,1)$ - distributed, which means that the probability density function (pdf) is Gaussian distributed with a mean of zero and a variance of one, as described in Eq. 1:

$$pdf = \frac{1}{\sqrt{2\pi\sigma^2}} \exp\left(-\frac{(x-\mu)^2}{2\sigma^2}\right) \quad (1)$$

with the position x , the mean μ and the variance σ^2 .

The Wiener process also underlies the central limit theorem, which is defined as follows [28-34]:

If $(X_n)_{n \geq 1}$ is a sequence of independent, identically distributed random variables S_n with mean μ and finite variance $\sigma^2 > 0$, $\frac{S_n - n\mu}{\sqrt{n\sigma^2}}$ converges towards $N(0,1)$ for $n \rightarrow \infty$.

In simple terms, a distribution of random variables converges to a normal distribution for a sufficiently high number of observations ($n \rightarrow \infty$).

Inside the mucus cells (cavities), the particles diffuse normally and unrestrictedly with a diffusion coefficient given by the Stokes-Einstein relation [5,35,36]:

$$D_0(\eta, R) = \frac{k_B T}{6\pi\eta R} \quad (2)$$

with the Boltzmann-constant k_B , the absolute temperature T , the hydrodynamic radius R of the particle, and the dynamic viscosity η of the interstitial fluid.

The Brownian motion is a stochastic process with the conditions of a Wiener process, as mentioned before. In the certain case of Brownian motion, the variance of the Wiener process is defined as follows:

$$\sigma^2 = \sqrt{2D_0\Delta\tau} \quad (3)$$

where $\Delta\tau$ is the duration of the discrete time step. The mean of this process is zero and due to the random walk of the Brownian particles, the variance has to be multiplied by a Gaussian distributed random number.

For drug delivery and the understanding of how viruses can affect the body, it is important to study drug and particle transport through mucus (see [4, 5] and the references therein). Various models assumes Fick's second law and predicts therefore a time-independent

diffusion coefficient D, however as the function of specific mucus, particle or drug properties. In particular, for particles, microrheological experiments can be performed to obtain local information about the mucus. Some experiments showed a nonlinear mean squared displacement $MSD(\tau)$ of these particles as function of the time lag [11, 14]. Erickson et al. suggested a mathematically motivated model of a time-scaled and a fractional subdiffusion approach to describe a "subdiffusive" behavior in $MSD(\tau)$ data [37].

In particular, the studies of Dudko et al. introduced a physically motivated model of normal Brownian diffusion of molecules or particles in a scaffold structure to mimic a heterogeneous material made from reflecting walls and apertures [26, 27]. However, these studies do not refer to mucosal model systems. Based on normal diffusion, their model also predicts a nonlinear "subdiffusive" $MSD(\tau)$, but as a transient effect between intervals of normal diffusive behavior. The mathematical properties of the model are discussed in [26,27,38–44]. The homogenization of the boundaries yields to an isotropic system for diffusing particles. The three-dimensional system is reduced to a one-dimensional system, as it is discussed in detail in [26, 27]. Especially an exact analytic expression for the Laplace transform of $MSD(\tau)$ is given, but the inverse Laplace transform must be performed numerically.

Despite of the studies from Erickson et al., who justify their model with the experimental data for HIV-virions in human cervical mucus [37,45], in this work, we recover the model from Dudko et al. [26,27] to compare it with experimental data for coated and uncoated particles in mucus from the respiratory tract [11,14].

The scaffold structure of mucus in Fig. 1 indicates a "cage-effect". Some studies call it a transient "cage-effect", which is assumed as the reason of the restricted diffusion for longer time scales and length scales respectively [46-49]. Existing theoretical approaches deal with three-dimensional [27,41,42], two-dimensional [39,44], and one-dimensional systems [26,40] to describe the restricted diffusion of particles. The publication of Hansing et al. [50] used a comprehensive theoretical model to include the inter-particle and particle-boundary interactions.

The model is isotropic due to the homogeneous membranes. Therefore we only consider the one dimensional (1D) unbiased diffusion of particles exemplary in the x-direction from this point onward. A very common statistical characterization of the stochastic motion of particle trajectories is the $MSD(\tau)$ of particle positions with respect to its initial position, given as follows:

$$MSD_{1D}(\tau) = \langle (x(\tau) - x(0))^2 \rangle \quad (4)$$

where the $\langle \cdot \rangle$ denotes the ensemble average and τ the time interval. In case of a random initial position, the particular choice of the initial time is not important. The system becomes ergodic. To improve the statistics from experimentally obtained trajectories, and sometimes, in numerical simulations, frequently an additional time-average is performed [49].

The MSD is also defined as the 2nd moment of the probability density function (pdf), given by [26]:

$$MSD_{pdf}(\tau) = \int (x(\tau) - x(0))^2 pdf(x, \tau) dx \quad (5)$$

The pdf of the particle displacement in a diffusion process with Brownian particles, moving freely inside a fluid-filled mucus cell, is defined by a mean μ in $[0; L]$ with the edge size of the cell, respectively the distance between the boundaries, L , and a variance $\sigma^2 = \sqrt{2D_0\Delta\tau}$, as already defined in Eq. 3.

The suitable combination of two analytical limits yields in the mentioned heuristic analytic equation for the MSD as in [27]. At small length scales and times ($\tau \rightarrow 0$), the diffusion of a particle is not affected by the walls, and the motion is unbounded and characterized by a linear $MSD(\tau)$, according to the Einstein-Smoluchowski-equation [51-53]:

$$MSD_{1D}(\tau) = 2D_0\tau \quad at \tau \rightarrow 0 \quad (6)$$

As the second analytical limit, we consider the $MSD(\tau)$ of diffusing but trapped particles in an interval with completely reflecting walls. As common in experiments, the average of a uniform distribution of the initial position in the interval $[0; L]$ is taken into account. The analytical $MSD_L(\tau)$ is given as follows (see appendix in [54] and [27]):

$$MSD_L(\tau) = \frac{L^2}{6} - \frac{16L^2}{\pi^4} \sum_{\substack{m=1 \\ (odd)}}^{\infty} \frac{1}{m^4} \exp\left\{-\frac{m^2\pi^2 D_0}{L^2}\tau\right\} \quad (7)$$

Note that the same equation is reported in [27] as Eq. 2.8, however, there is an error in the coefficient of the sum. The series in Eq. 7 converges very quickly, and the calculation can be truncated after a few elements ($m < 15$), but still maintains a reasonable accuracy. The suitable combination of both limits yields in the mentioned heuristic analytic equation for the

MSD [27]. The analytically small time interval limit ($\tau \rightarrow 0$) of Eq. 7 obeys Eq. 6. In the limit of a long time interval ($\tau \rightarrow \infty$), the MSD is saturated to a constant value of $L^2/6$ [see Fig. 7 (A) with $p_M = 0$].

In the case of permeable membranes, the particles can diffuse without constricting even for periodic repetitions. Based on the central limit theorem, the diffusion at longer time periods is considered as normal with a smaller diffusion coefficient $D_{\text{eff}} < D_0$. In order to quantify the permeable membranes, we introduce the permeability p_M as a parameter in our numerical simulations. Note that p_M is directly related to D_{eff} . An approximate approach to calculate D_{eff} as function of the aperture size and the mean cavity size L can be found in [39, 44]. The limiting cases of total reflection and total transmission are represented by $p_M = 0$ ($D_{\text{eff}} = 0$) and $p_M = \infty$ ($D_{\text{eff}} = D_0$), respectively [see Fig. 7 (A)]. p_M is neither the permeability in units of m^2 defined using Darcy's law nor the probability of transmission/reflection if a particle hits the membrane. However, the probability of reflection is introduced as $r(p_M)$ in our numerical simulations (see below).

The effective diffusion coefficient can be calculated with the MSD data in the normal diffusive regime ($\alpha = 1$) at $\tau \rightarrow \infty$ and is given by:

$$D_{\text{eff}} = \frac{\text{MSD}(\tau \rightarrow \infty)}{2\tau} \quad (8)$$

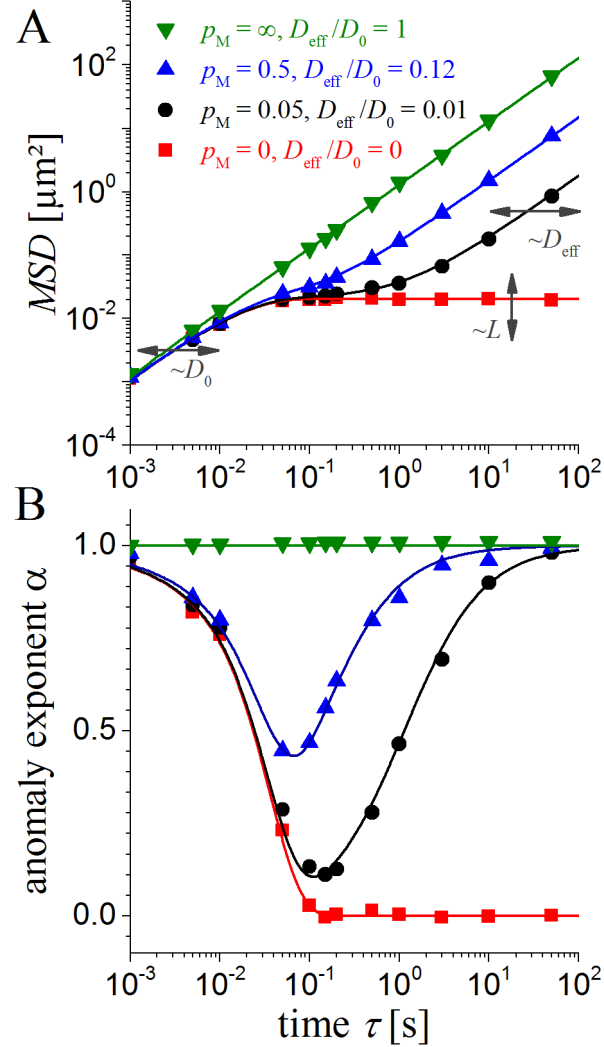


Figure 7: (A) Calculated MSD from particles with a diameter of 200 nm in mucus using a membrane distance of $L = 0.35 \mu\text{m}$ and $D_0 = 0.65 \mu\text{m}^2/\text{s}$ for various permeability of the membranes p_M and the belonging D_{eff} in the legend. Data from numerical simulations of Brownian diffusion are shown as symbols ($\Delta t = 1 \text{ ms}$), and are from an analytic approximation using Eq. 9 as lines. (B) The calculated anomaly exponent α to $\text{MSD}(\tau) \sim \tau^\alpha$ using Eq. 10 with the same legend as in (A).

Our numerical simulation will prove the following heuristic approach: a good analytic approximation to calculate the $\text{MSD}(\tau)$ in case of caged diffusion in presence of periodic permeable membranes is the appropriate superposition of the solutions for free and trapped diffusion, Eq. 6 and Eq. 7, respectively. The diffusion coefficients D_0 and D_{eff} , as well as the cavity size L are the only involved parameters.

$$\text{MSD}_{app}(\tau) = \left(1 - \frac{D_{\text{eff}}}{D_0}\right) \text{MSD}_L(\tau) + 2D_{\text{eff}}\tau \quad (9)$$

This combination fulfills the short and long time limits as discussed above. It can be shown that the relative difference to the simulated results in the transient region is mostly less than 10 % and never more than 20 % (see Fig. 8).

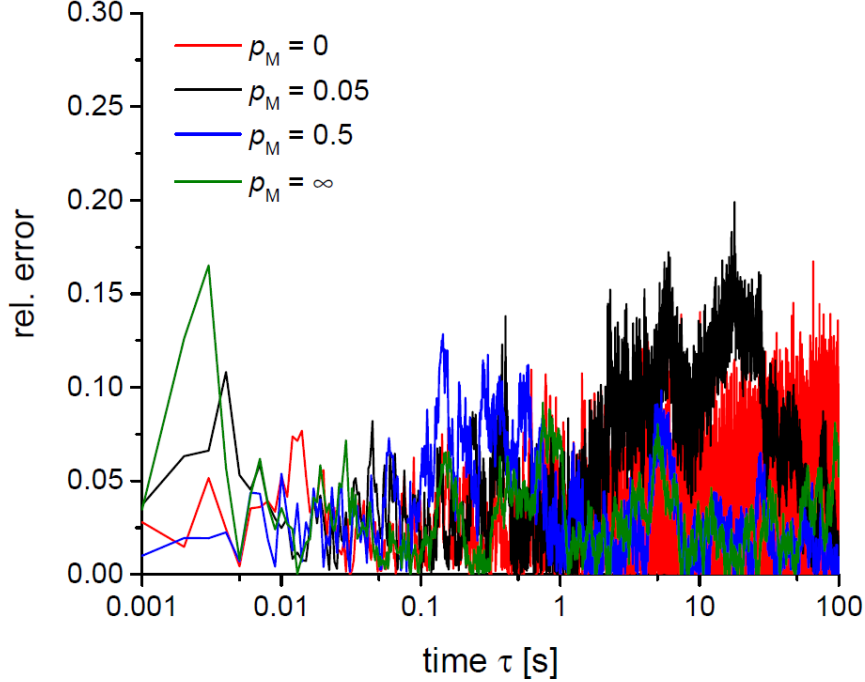


Figure 8: Relative error between the MSD from the numerical simulations of the Brownian diffusion and the results from Eq. 9.

The following Figure 9 shows the relation of the time-averaged relative error between the numerical simulation and the analytic approximation for different p_M -values. As obvious, the higher p_M , the lower is the error between the analytic equation and the numerical simulation.

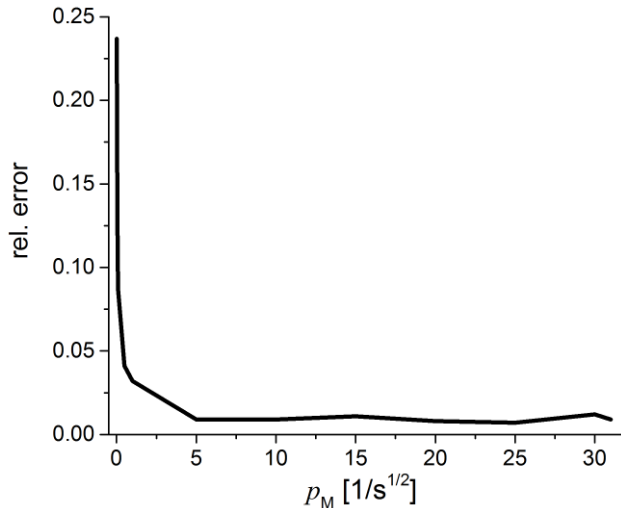


Figure 9: Time-Averaged relative error between the MSD from the numerical simulations of the Brownian diffusion and Eq. 9 as a function of p_M .

So, our developed analytic approximation of the numerical simulation converges with higher permeability p_M , but also with a lower duration of the time step $\Delta\tau$.

Our numerical simulation also confirms the following intuitive relation from the boundary homogenization [38,44]: the smaller the permeability p_M of the membranes, the lower D_{eff} will be, and vice versa. Naturally, the particle radius determines the free diffusion coefficient $D_0(\eta, R)$ by Eq. 2 and the permeability through the membrane, the effective diffusion coefficient $D_{\text{eff}}(p_M(R), L, D_0)$ respectively. Bigger particles cannot pass the apertures between the cavities easily, thereby resulting in a reduced permeability, i.e., D_{eff} becomes smaller. Hence, the only essential parameters for $\text{MSD}(\tau)$ in Eq. 9 and in the simulations are D_0 from the unrestricted diffusion at short times, D_{eff} from the restricted diffusion at long times, and L as the cavity size [see Fig. 7(A)]. A direct consequence of the model is that the $\text{MSD} \sim \tau^\alpha$, $\alpha < 1$ appears only as a transient phenomenon, which should not be misinterpreted as subdiffusion or abnormal diffusion (see Fig. 7(A) and Ref. [44]).

It is common to plot the $\text{MSD}(\tau)$ in a double logarithmic scale to visualize deviations from the normal diffusive behavior. Berezhkovskii et al. provided in [40] a good method to discriminate between anomalous diffusion (subdiffusion) and transient subdiffusive behavior by calculating anomaly exponents α in three different ways. In case of anomalous diffusion, α is constant and independent of the method of determination. In our study, we characterize the transient "subdiffusive" behavior by determining a time-dependent anomaly exponent $\alpha(\tau)$, from the dimensionless logarithmic derivative of the $\text{MSD}(\tau)$. This is given as follows [40,55,56]:

$$\alpha(\tau) = \frac{d \log(\text{MSD}(\tau))}{d \log(\tau)} = \frac{\tau}{\text{MSD}(\tau)} \frac{d \text{MSD}(\tau)}{d \tau} \quad (10)$$

and shown in Fig. 7 (B).

Note that another possible characterization of the nonlinear $\text{MSD}(\tau)$ is given by a time dependent diffusion coefficient $\text{MSD}(\tau) = 2D(\tau)\tau$. Both characterizations are localized to a specific time lag τ and do not represent the overall nature of the system.

In all experiments, the accessible time range is limited by both the frame rate of the camera and the maximal recorded time interval that the diffusing particle is within the depth of field of the microscope for detection, e.g., τ is between 0.05 and 5 s [11,14]. In Fig. 7, we used various D_{eff} and a reasonable interstitial fluid viscosity of $\eta = 3.5 \text{ mPas}$, which is similar to

that of water. Hence, the predicted time range of transition ("subdiffusion") appears within the typically experimental conditions.

The presented model focuses on a qualitative description, using only as few parameters as possible. Therefore, we can neither cover the broad range of existing mucus variations nor the various types of particle coatings. Using only three physical interpretable parameters, we can reproduce the measured "subdiffusive" behavior. However, the "subdiffusion" reflected by a $MSD \sim \tau^\alpha$, $\alpha < 1$, is identified as a transient behavior. It naturally appears due to the continuous transition from normal, unrestricted diffusion ($MSD \sim \tau$) at short times to a normal, restricted diffusion at long-time scales, longer distances respectively, caused by the repeated confinement of the particles. The two limiting normal diffusion regimes are quantized by the diffusion coefficients, D_0 and D_{eff} , respectively. The third necessary parameter in the model is the mean cavity size L . The transition regime should not be identified as anomalous diffusion in the sense of space-time scale invariant, continuous-time random walks, or as a fractional Brownian motion [40]. Only one length scale is added to the system, the mean cavity size L .

In order to substantiate the suggested approximation in Eq. 9, we performed numerical simulations of the system. The used SDE, which describes Brownian diffusion, is the Langevin equation, given as [52,57]:

$$m_p \frac{d^2}{dt^2} x(t) = F_{ext} + F_{thermal} + F_{Stokes} \quad (11)$$

with the particle position $x(t)$, the particle mass m_p , the Stokes force

$$F_{Stokes} = -6\pi\eta R \left(\frac{d}{dt} x(t) - u \right), \quad (12)$$

and the thermal force

$$F_{thermal} = \sqrt{12\pi\eta R k_B T} \xi(t) \quad (13)$$

with the velocity u of the surrounding fluid and the standard Gaussian noise $\xi(t)$.

The Brownian motion of the nanosized particles in a liquid is described by an overdamped movement, as the inertia of the particles does not play a role ($m_p \rightarrow 0$). We assume no external forces F_{ext} acting on the particles. Additionally, neither drift nor any ballistic regime

will appear during the particle movement and we also neglect the velocity of the surrounded fluid, as we assume the interstitial fluid to be static. Under these assumptions, the unrestricted (free) motion of the particles at all times is then described by the massless Smoluchowski-approximation of the Langevin equation [52,57]:

$$\frac{d}{dt}x(t) = \sqrt{2D_0}\xi(t) \quad (14)$$

A very efficient way to simulate this stochastic equation at discrete times is given by the Euler-Maruyama method [52,58-60], as follows:

$$\begin{aligned} x_{k+1} &= x_k + \Delta x_k \quad \text{with} \\ \Delta x_k &= \sqrt{2D_0\Delta\tau}g; \quad k = 1, \dots, N-1 \end{aligned} \quad (15)$$

where N is the maximum number of time steps and $g \in N(0,1)$ is a Gaussian distributed random number. We use a uniformly distributed initial position $x_0 \in [0,L]$.

In presence of reflecting walls or permeable membranes, the particle motion must comply with the boundary conditions in each iteration. The treatment of diffusion through permeable membranes is still a topic of current research. We adapt the algorithm, referred as the Robin boundary condition, from [59,60] for partially reflecting and absorbing walls. The permeable membranes in our simulations are described by a random reflecting and passing of the wall, independent of the angle of impact. Hence, the iteration scheme from Eq. 15 has to be modified. When the particle trace hits the membrane, the probability of reflection must depend on the spatial resolution of the simulation, the duration of the discrete time step respectively. It becomes clear that a shorter $\Delta\tau$ leads to a more fractional trajectory, and there are more hits to an (imaginary) wall in the same time span. To preserve the ratio of transmissions per unit time, the probability of reflection at each hit must be reduced. According to [59,60], we introduced the reflection probability r :

$$r = 1 - p_M \sqrt{\Delta\tau} \quad (16)$$

with the permeability $p_M \in [0,\infty]$ of the membrane in units of $s^{-1/2}$. The iteration scheme in Eq. 15 and the reflecting probability in Eq. 16 requires a sufficiently small $\Delta\tau$ to achieve accurate statistical quantities, at least to preserve a $r \in [0;1]$. This requirement results in a small time step $\Delta\tau$, particular in the limiting case of $p_M \rightarrow \infty$, and consequently $D_{\text{eff}} \rightarrow D_0$. The modified iteration scheme is given as follows:

$$x_{k+1} = x_k + \begin{cases} \Delta x_{k,r} & \text{with } r, \text{if a membrane is crossed} \\ \Delta x_k & \text{otherwise.} \end{cases} \quad (17)$$

The displacement of the particle for being reflected by the periodic membranes at $x = jL$, $j \in \mathbb{Z}$, is given as follows:

$$\Delta x_{k,r} = \begin{cases} -\Delta x_k + 2L - 2 \text{mod}(x_k, L), & \Delta x_k > 0 \\ -\Delta x_k - 2 \text{mod}(x_k, L), & \Delta x_k < 0 \end{cases} \quad (18)$$

using the modulus function mod. The $\Delta x_k > 0$ represents a particle motion from left to right and $\Delta x_k < 0$ is the reverse. For more details, please see the supplementary material. Some exemplary trajectories in 2D are shown in Fig. 6(C). In this Figure, the x and y components of each trajectory are two independent 1D simulations. The particles are mostly caged in the current cavity, but they can also pass through the borders/membranes with a certain probability $1-r$.

In Figure 10 the relation between the permeability p_M , respectively the reflection probability $r(p_M)$, and the effective diffusion coefficient $D_{\text{eff}}(p_M)$ is given. As shown, D_{eff} increases with a higher distance between the membranes L , in particular for low p_M -values. Here, the approximation at $D_{\text{eff}} = D_0$ is obvious for high p_M -values, when the particles can move freely without appearing permeable membranes, respectively with membranes, described by a reflection probability of $r = 0$.

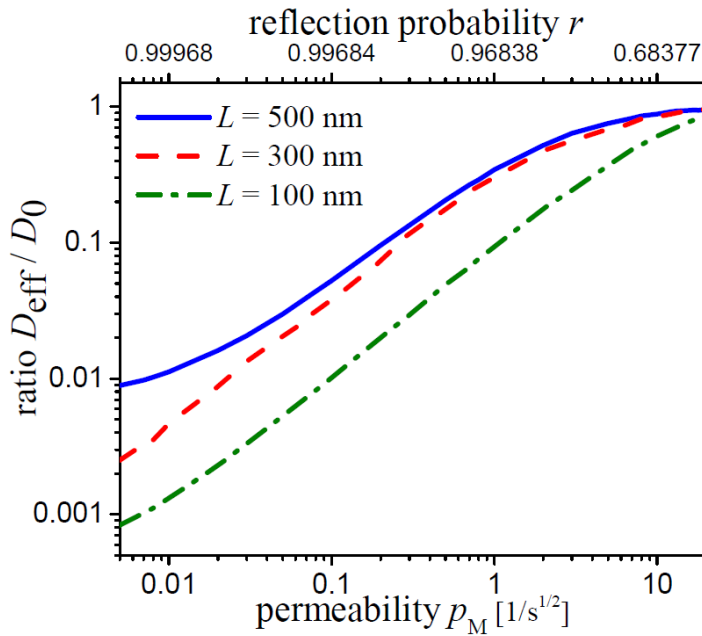


Figure 10: Calculated ratio D_{eff}/D_0 with $D_0 = 0.32 \mu\text{m}^2 \text{s}^{-1}$ ($R = 100 \text{ nm}$, $\eta = 7 \text{ mPas}$) as function of p_M , respectively r , and various membrane distances L . A $\Delta t = 1 \text{ ms}$ was used in the numerical simulations of Brownian diffusion.

There is an approximation of the ratio D_{eff}/D_0 for $p_M \rightarrow \infty$ to a value of one and also an approximation for $p_M \rightarrow 0$ to a value of zero. As obvious, the higher the distance between the permeable membranes L , the lower is the needed p_M to achieve a $D_{\text{eff}} = 0$.

Similar to the analytical solution of MSD_{app} from Eq. 9, we developed a further analytic approximation equation to yield the MSD_{anal} of particles diffusing in an array of cavities, also separated by permeable membranes. Contrary to the numerical simulations, which can be described by Eq. 9, now, we keep the probability of a particle to pass the permeable membrane to be constant for each time step in the numerical iteration scheme from Eq. 17 and Eq. 18. However, to simulate this kind of diffusion by a stochastic Wiener process, we used the same iteration scheme, but as already mentioned, with a constant instead of a random permeation probability of a particle for each time step. The analytical solution to describe this numerical iteration scheme, respectively to calculate the MSD , is hence given as:

$$\text{MSD}_{\text{anal}}(\tau) = r \text{MSD}_L(\tau) + (1-r)2D_0\tau \quad (19)$$

with the reflection probability, as described in Eq. 16. Henceforward, we name the numerical simulation of particle diffusion, based on random permeation probabilities, respectively the diffusion, described by Eq. 9, as Brownian diffusion. The diffusion, described by Eq. 19,

respectively the numerical simulation, based on constant permeation probabilities, will be named as Fickian diffusion from this point onward. Latter can be easily compared with the cell-window model, whereat the former diffusion model is comparable to the cell-array model (see section 4.3.2).

Figure 11 shows the analytical solution for the MSD_{anal} , as described in Eq. 19, and the corresponding anomaly exponent α , which is the slope of the MSD-curve in a double logarithmic plot. The data from numerical simulations of the Fickian diffusion are shown as symbols. The legend indicates the following conditions:

- $p_M = \infty, D_{\text{eff}}/D_0 = 1$ (green inverted triangles)
- $p_M = 0.5, D_{\text{eff}}/D_0 = 0.02$ (blue upward triangles)
- $p_M = 0.05, D_{\text{eff}}/D_0 = 0.002$ (black circles)
- $p_M = 0, D_{\text{eff}}/D_0 = 0$ (red squares)

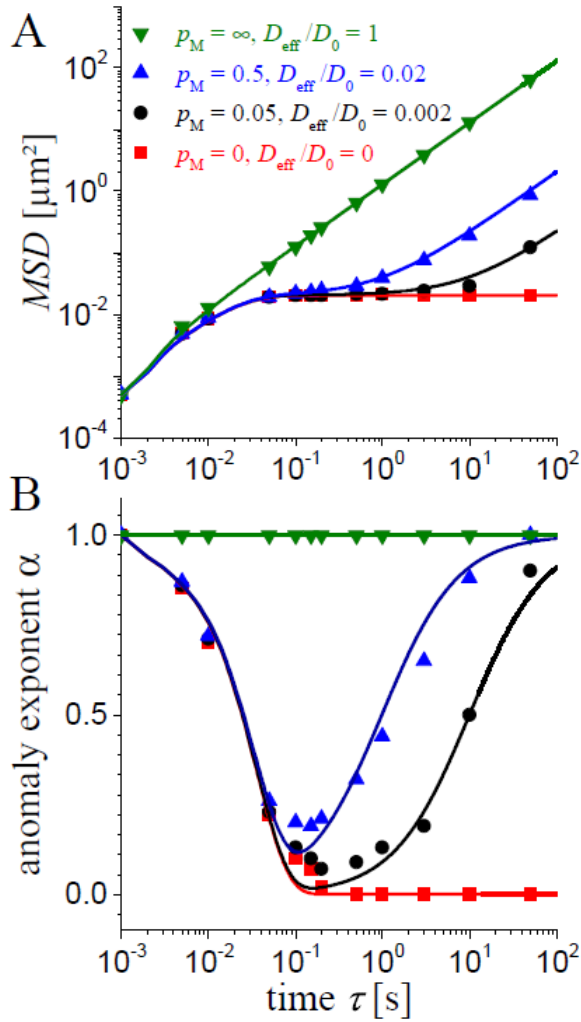


Figure 11: (A) Calculated MSD from particles with a diameter of 200 nm in mucus using a membrane distance of $L = 0.35 \mu\text{m}$ and $D_0 = 0.65 \mu\text{m}^2/\text{s}$ for various permeability of the membranes p_M and the belonging D_{eff} in the legend. Data from numerical simulations of Fickian diffusion are shown as symbols ($\Delta t = 1 \text{ ms}$), and are from an analytic approximation using Eq. 19 as lines. (B) The calculated anomaly exponent α to $MSD(\tau) \sim \tau^\alpha$ using Eq. 10 with the same legend as in (A).

The combination in Eq. 19 again fulfills the short and long time limits as already discussed, and shows that the relative difference to the simulated results in the transient region is mostly less than 15 % and we have never found the deviation to be more than 35 % (see Fig. 12).

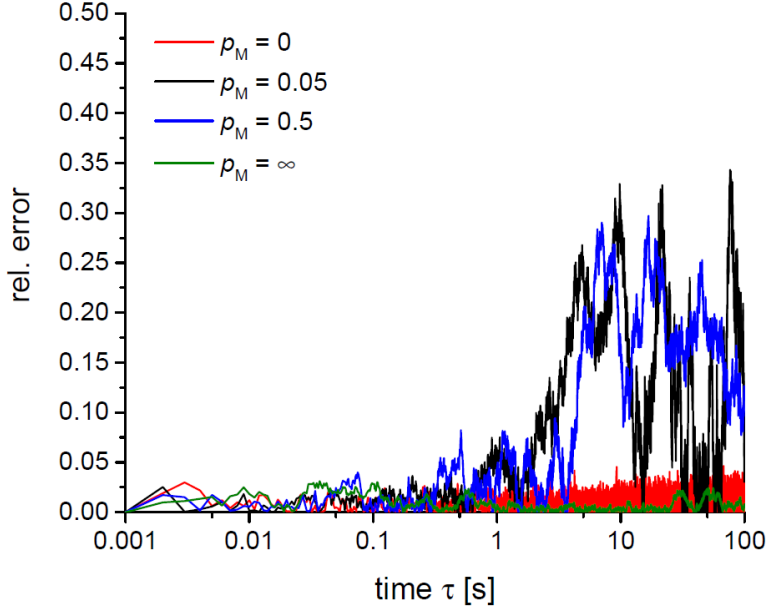


Figure 12: Relative error between the MSD from the numerical simulations of the Fickian diffusion and the results from Eq. 19.

The following Figure 13 shows the relation of the time-averaged relative error between the numerical simulation and the analytic approximation from Eq. 19 for different p_M -values. Since here, the dependency is not that obvious as in Fig. 9, however, the higher p_M , the lower is the error between the analytic equation and the numerical simulation.

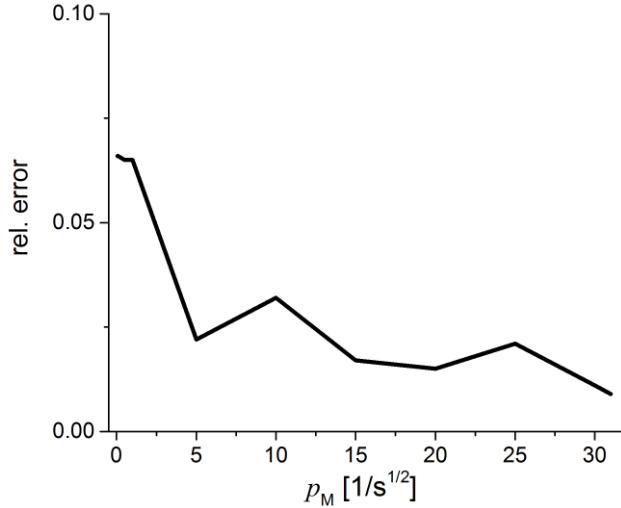


Figure 13: Averaged relative error between the MSD from the numerical simulations of the Fickian diffusion and Eq. 19 as a function of p_M .

Again, our developed analytic approximation of this numerical simulation converges with higher permeability p_M and a lower duration of the time step $\Delta\tau$.

Surprisingly, when the ratio between D_{eff} and D_0 is plotted against different values of p_M with a distance L of 100 nm, 300 nm and 500 nm (see Fig. 14), for the Fickian diffusion we get a completely different shape of the curve, compared to the Brownian diffusion (see Fig. 10).

Here, the approximation at $D_{\text{eff}} = 0$ is obvious for low p_M -values, when the particle movement is almost totally restricted ($r = 1$).

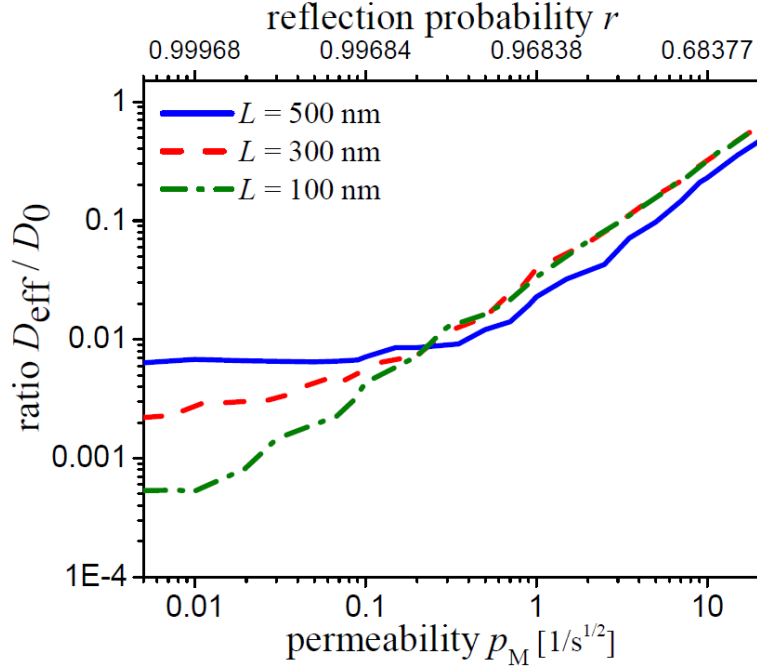


Figure 14: Calculated ratio D_{eff}/D_0 with $D_0 = 0.32 \mu\text{m}^2 \text{s}^{-1}$ ($R = 100 \text{ nm}$, $\eta = 7 \text{ mPas}$) as function of p_M , respectively r , and various membrane distances L . A $\Delta t = 1 \text{ ms}$ was used in the numerical simulations (Fickian diffusion).

As obvious, the p_M -value for $D_{\text{eff}} = 0$ depends also on the distance between the permeable membranes L . So, the Brownian diffusion converges to a $D_{\text{eff}} = D_0$ for high permeabilities, whereas the Fickian diffusion converges to a $D_{\text{eff}} = 0$ for low permeabilities.

As already mentioned, this analytical equation (Eq. 19) does not describe the Brownian, but the Fickian diffusion of particles within confined geometries. So, we developed analytical solutions for both numerical simulations and in the next section, we will compare the Brownian diffusion with the Fickian diffusion. Additionally, we will also compare the simulated Fickian and Brownian diffusion with experimental studies.

The numerical simulation of long trajectories opens up the possibility to determine the relation between the permeability p_M used in the simulation and the ratio of effective to free diffusivity $D_{\text{eff}} = D_0$. For various fixed lattice constants L , see Fig. 10, respectively Fig. 14. As expected, the relation is strictly increasing, nonlinear and saturates in unity for large permeability, respectively in zero for low permeability. A general analytic derivation of this relation is still an open question [59,60]. Note that the p_M is neither in direct relation to the

permeability P nor the trapping rate κ in [26,27,44]; the physical units are different. Our simulations are also different from those former approaches [26,27,44], due to the explicit usage of permeable membranes instead of a 2D or 3D simulation of standard Brownian motion in a cubic lattice with apertures of fixed size and reflecting walls.

Finally, the presented model predicts a transient "subdiffusive" behavior in the experimentally accessible time range between 0.05 and 5 s for realistic parameter assumptions. For instance, for a particle diameter of 200 nm, a cavity extension of $L = 350$ nm, and using a permeability $p_M = 0.05$, this results in an effective mucus viscosity of 100 times more as it of the interstitial fluid (see bullets and black line in Fig. 7 and Fig. 11, respectively). A transient "subdiffusive" time range also remains for other particle diameters due to the following conclusion: smaller particles belong to a larger D_0 (see Eq. 2), and result in a larger expected D_{eff} . Hence, the $\text{MSD}(\tau)$ curve will shift upwards in the double logarithmic plot and for fixed L , the time range with "subdiffusion" will shift slightly to smaller values. The opposite is in the case for bigger particles. Hence, a transient "subdiffusive" behavior is predicted for any particle diameter if $D_{\text{eff}} < D_0$. However, if the particles become very small, as they can pass the membranes/the scaffold structure very easily (p_M will increase), D_{eff} will be in the order of magnitude of D_0 and the "subharmonic" region will disappear.

4.1.3 Results & Discussion

In this section, model predictions with measured $\text{MSD}(\tau)$ are compared by adapting the required parameters to obtain a good visual agreement. The physical meaning of our results are discussed and they are compared with independent measurements, if available. There are results from other theoretical studies, where a similar shape of the MSD -curves and anomaly exponent α , as shown in Fig. 7 and Fig. 11, were predicted , but using other assumptions and models [27,40-42,44,48,50,55]). We used particle tracking data from uncoated, polystyrene (PS) particles in human sputum from cystic fibrosis (CF) patients [14] and from coated PEGylated, as well as carboxylated polystyrene particles in pulmonary mucus from humans without lung disease [11]. A comprehensive model with including inter-particle and particle-boundary interactions can be found in [50], where the simulated results and the observed transient "subdiffusive" behavior are compared with experimental studies.

Usually, sputum has a lower viscosity than mucus. However, sputum from cystic fibrosis patients is characterized by a denser mesh compared to pulmonary, healthy mucus [14].

In both Figures 15 (simulated Brownian diffusion) and 16 (simulated Fickian diffusion), calculated MSD curves (using Eq. 14-18) of 100nm- and 200 nm-sized particles are shown as a dashed line and the solid lines refer to experimental MSD for different particles (see [14]). Reasonable parameters D_0 , D_{eff} and L are assumed to represent the data.

Focusing on the slope at short and long time lags τ , the predicted transition to normal diffusive behavior with a slope $\alpha = 1$ is evident, both in the numerical and in the experimental data. At short times, the predicted diffusion becomes normal ($\alpha \leq 1$) and the MSD is proportional to the diffusion coefficient D_0 from the Stokes-Einstein relation in Eq. 2. At long times, the predicted diffusion becomes normal again but with an effective diffusion coefficient D_{eff} . The "subdiffusive" regime with $\alpha \approx 1/2$ appears as a transient effect and agrees with experimental observations. In Figure 15, we used three parameters (L , p_M , D_0) to adjust visually the calculated MSD-curves to the experimental MSD-curves: a $D_0 = 0.013 \mu\text{m}^2/\text{s}$, a membrane distance of $L = 0.5 \mu\text{m}$, and a $p_M = 0.5$, resulting in a $D_{\text{eff}} = 0.012 \mu\text{m}^2/\text{s}$ for the 100 nm-particles and $D_0 = 0.007 \mu\text{m}^2/\text{s}$, $L = 0.2 \mu\text{m}$, and $p_M = 0.3$, resulting in an effective diffusion coefficient $D_{\text{eff}} = 0.002 \mu\text{m}^2/\text{s}$ for the 200 nm-particles. In particular, the D_{eff} of the 200 nm-particles is significantly lower than D_0 in accordance with the apparent "subdiffusive" behavior. Here, the MSD curve of the 200 nm-particles shows a very pronounced transition regime with a transient "subdiffusive" behavior, compared to the 100 nm-particles, where the D_{eff} is almost equal to D_0 . In case of the simulated Fickian diffusion (see Fig. 16), we only changed the permeability p_M to be 8 for the 100 nm-particles ($D_{\text{eff}} = 0.009$) and $p_M = 5$ for the 200 nm-particles ($D_{\text{eff}} = 0.003$). The assumed D_0 of the 100 nm-particles is in both cases double that of the 200 nm-particles, according to Eq. 2 with the equal interstitial fluid viscosity η . The assumed high frequent number of permeable membranes per length scale (low L -value) is in good accordance with the dense structure of sputum from CF patients.

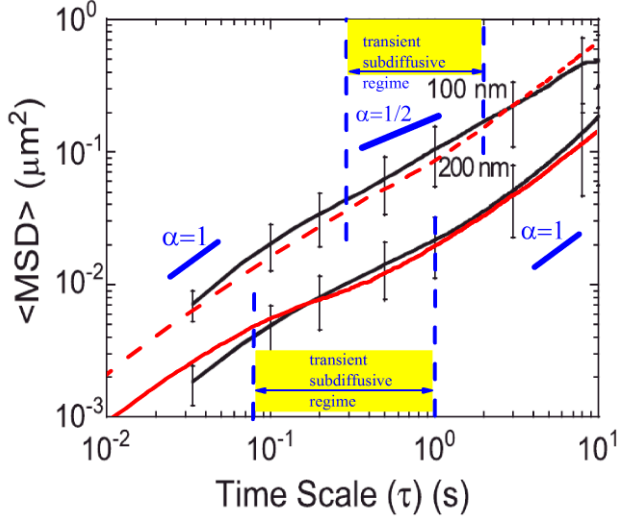


Figure 15: Comparison of experimental data and the calculated MSD for 100 nm- and 200 nm-particles, indicated as a dashed and a straight line, respectively. A membrane distance $L = 0.5 \mu\text{m}$, a diffusion coefficient $D_0 = 0.013 \mu\text{m}^2/\text{s}$, and a permeability $p_M = 0.5$ were assumed for the 100 nm-particles. A membrane distance $L = 0.2 \mu\text{m}$, a diffusion coefficient $D_0 = 0.007 \mu\text{m}^2/\text{s}$, and a permeability $p_M = 0.3$ were assumed for the 200 nm-particles. These assumptions result in a ratio of $D_{\text{eff}}/D_0 = 0.88$ and $D_{\text{eff}}/D_0 = 0.35$ for the particles with a diameter of 100 and 200 nm, respectively. In the background, a figure taken from [14] with experimental data for polystyrene particles in human sputum from CF patients (solid lines) is shown. The transient time regime of "subdiffusion" is marked.

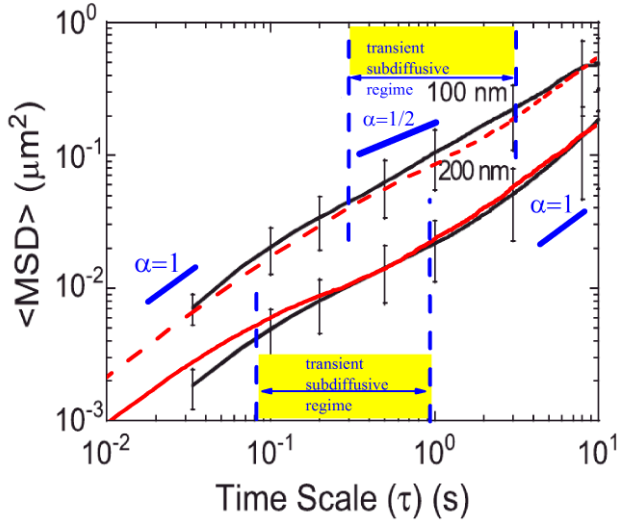


Figure 16: Comparison of experimental data and the calculated MSD for 100 nm- and 200 nm-particles, indicated as a dashed and a straight line, respectively. A membrane distance $L = 0.5 \mu\text{m}$, a diffusion coefficient $D_0 = 0.013 \mu\text{m}^2/\text{s}$, and a permeability $p_M = 8$ were assumed for the 100 nm-particles. A membrane distance $L = 0.2 \mu\text{m}$, a diffusion coefficient $D_0 = 0.007 \mu\text{m}^2/\text{s}$, and a permeability $p_M = 5$ were assumed for the 200 nm-particles. These assumptions result in a ratio of $D_{\text{eff}}/D_0 = 0.7$ and $D_{\text{eff}}/D_0 = 0.45$ for the particles with a diameter of 100 and 200 nm, respectively. In the background, a figure taken from [14] with experimental data for polystyrene particles in human sputum from CF patients (solid lines) is shown. The transient time regime of "subdiffusion" is marked.

Note that according to the isotropy of the model, the 2D- and 3D-MSD is given by the double and triple of the predicted 1D-MSD. In Fig. 15 and Fig. 16 we show, that our simulated 3D-MSD data are well in line with experimental data as reported in [14].

Due to the less dense mesh in healthy mucus, compared to mucus from CF patients, also the diffusivity of 500 nm particles is discussed in the following paragraphs. In sputum from CF patients, these particles are totally trapped, but in healthy mucus, the mean pore size is high enough to allow bigger particles to diffuse through the mucus layer. However, the time, which is needed to pass this layer is significantly higher than that for smaller particles (see section 4.2.3).

In each of the Figures 17 (simulated Brownian diffusion) and 18 (simulated Fickian diffusion), three calculated MSDs are compared with the experimental MSD of different sized carboxylated particles in pulmonary mucus from humans without lung disease [11]. Reasonable values of the parameters D_0 , D_{eff} and L are assumed to represent the data. The different offset in the MSD for the various sized particles is simply due to the different D_0 (see Eq. 2) and the equal assumed interstitial fluid viscosity η . In Figure 17, we assumed the following parameters (D_0 , p_M , L) to adjust visually the calculated MSD-curves to the experimental MSD-curves of particles with a size of 100 nm (straight black line), 200 nm (grey dashed line), and 500 nm (grey dotted line), respectively: ($0.017 \mu\text{m}^2/\text{s}$, 0.5 , $0.5 \mu\text{m}$); ($0.004 \mu\text{m}^2/\text{s}$, 0.1 , $0.15 \mu\text{m}$); ($0.002 \mu\text{m}^2/\text{s}$, 0.05 , $0.15 \mu\text{m}$). The resulting D_{eff} are $0.007 \mu\text{m}^2/\text{s}$, $0.0003 \mu\text{m}^2/\text{s}$, and $0.0002 \mu\text{m}^2/\text{s}$, respectively. In case of the simulated Fickian diffusion (see Fig. 18), we changed the permeability p_M to be 5 for the 100 nm-particles ($D_{\text{eff}} = 0.003$), $p_M = 3$ for the 200 nm-particles ($D_{\text{eff}} = 0.0003$), and $p_M = 1.5$ for the 500 nm-particles ($D_{\text{eff}} = 0.0001$).

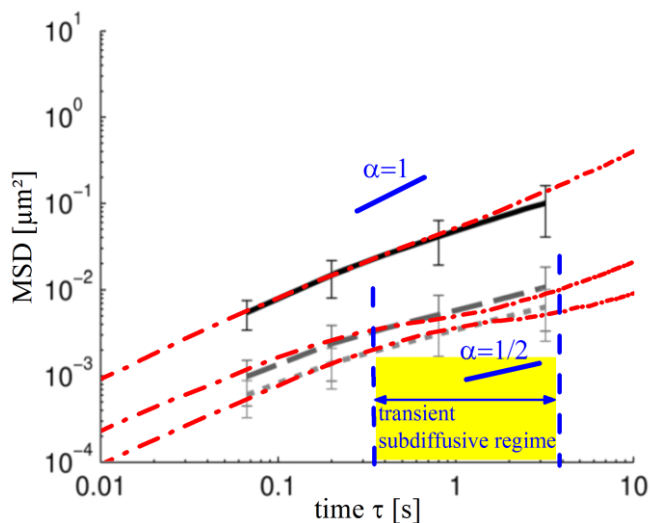


Figure 17: Comparison of calculated MSD for various parameters as dash-dotted lines and measured data as background image from [11]. A membrane distance $L = 0.5 \mu\text{m}$ for the 100nm-particles and $L = 0.15 \mu\text{m}$ for the 200nm- and 500nm-particles was assumed. The parameters of (D_0 , D_{eff}/D_0 , p_M) are given as (top to bottom) ($0.017 \mu\text{m}^2/\text{s}$, 0.4 , 0.5), ($0.004 \mu\text{m}^2/\text{s}$, 0.09 , 0.1), ($0.002 \mu\text{m}^2/\text{s}$, 0.09 , 0.05).

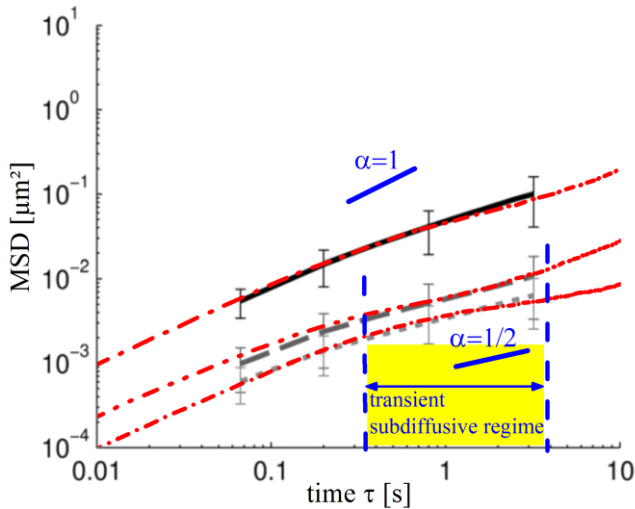


Figure 18: Comparison of calculated MSD for various parameters as dash-dotted lines and measured data as background image from [11]. A membrane distance $L = 0.5 \mu\text{m}$ for the 100nm-particles and $L = 0.15 \mu\text{m}$ for the 200nm- and 500nm-particles was assumed. The parameters of $(D_0, D_{\text{eff}}/D_0, p_M)$ are given as (top to bottom) $(0.017 \mu\text{m}^2/\text{s}, 0.18, 5)$, $(0.004 \mu\text{m}^2/\text{s}, 0.08, 3)$, $(0.002 \mu\text{m}^2/\text{s}, 0.05, 1.5)$.

If the particles are coated by PEG and are thus neutral (uncharged), less adherent or repulsive interaction between particles and mucus is observed [1,2]. Hence, the effective diffusion coefficient D_{eff} increases and becomes comparable to D_0 , and consequently the transient "subdiffusive" regime becomes less pronounced. This is the topic of the following paragraph.

In Figure 19 (simulated Brownian diffusion) and Figure 20 (simulated Fickian diffusion), three calculated MSDs are compared with the experimental MSD of different sized PEGylated particles in pulmonary mucus from humans without lung disease [11]. Reasonable values of D_0 , D_{eff} and L are assumed to represent the data. Again, the different offset in the MSD for the 100nm- and 200nm-particles is due to the different D_0 (see Eq. 2). This is because of the same assumed interstitial fluid viscosity η . We assumed a membrane distance of $L = 500 \text{ nm}$ for the 100 nm- and 200 nm-particles, a $L = 150 \text{ nm}$ for the 500 nm-particles, and the following values of D_0 and p_M : $0.1 \mu\text{m}^2/\text{s}$ and 10 for the 100 nm-particles, $0.05 \mu\text{m}^2/\text{s}$ and 0.5 for the 200 nm-particles, and $0.002 \mu\text{m}^2/\text{s}$ and 0.01 for the 500nm-particles; the resulting D_{eff} are $0.09 \mu\text{m}^2/\text{s}$, $0.02 \mu\text{m}^2/\text{s}$, and $0.0005 \mu\text{m}^2/\text{s}$, respectively. In case of the simulated Fickian diffusion (see Fig. 20), we only changed the permeability p_M to be 15 for the 100 nm-particles ($D_{\text{eff}} = 0.04$), $p_M = 10$ for the 200 nm-particles ($D_{\text{eff}} = 0.02$), and $p_M = 3$ for the 500 nm-particles ($D_{\text{eff}} = 0.0004$).

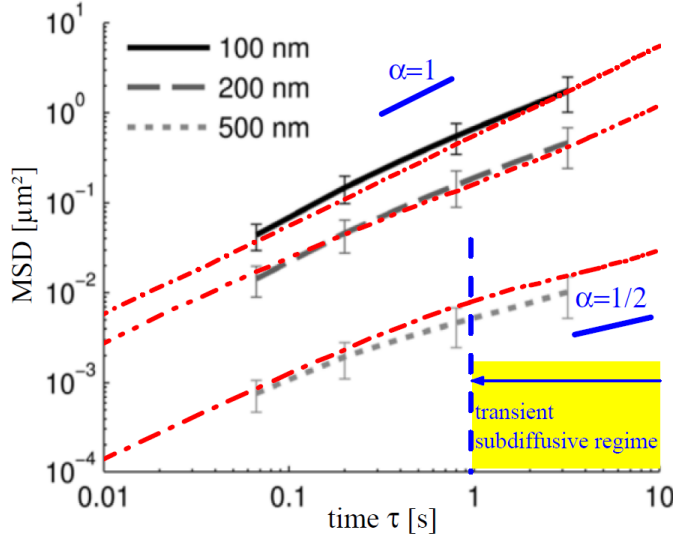


Figure 19: Comparison of calculated MSD for various parameters as dash-dotted lines and measured data as background image from [11]. The experimental particle diameters in the legend are also used in the calculations, as well as a membrane distance $L = 0.5 \mu\text{m}$ for the 100nm- and 200nm-particles and $L = 0.15 \mu\text{m}$ for the 500nm-particles. The parameters of $(D_0, D_{\text{eff}}/D_0, p_M)$ are given as (top to bottom) $(0.1 \mu\text{m}^2/\text{s}, 0.9, 10)$, $(0.05 \mu\text{m}^2/\text{s}, 0.4, 0.5)$, $(0.002 \mu\text{m}^2/\text{s}, 0.2, 0.01)$.

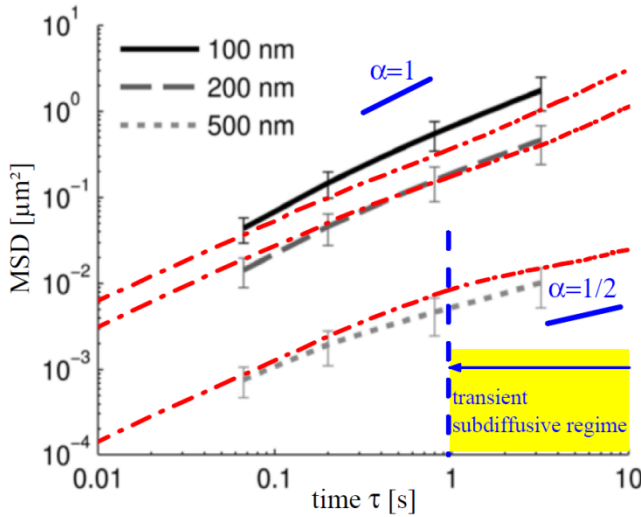


Figure 20: Comparison of calculated MSD for various parameters as dash-dotted lines and measured data as background image from [11]. The experimental particle diameters in the legend are also used in the calculations, as well as a membrane distance $L = 0.5 \mu\text{m}$ for the 100nm- and 200nm-particles and $L = 0.15 \mu\text{m}$ for the 500nm-particles. The parameters of $(D_0, D_{\text{eff}}/D_0, p_M)$ are given as (top to bottom) $(0.1 \mu\text{m}^2/\text{s}, 0.5, 15)$, $(0.05 \mu\text{m}^2/\text{s}, 0.4, 10)$, $(0.002 \mu\text{m}^2/\text{s}, 0.2, 3)$.

Due to the experimental fact of the less dense scaffold of the pulmonary mucus in comparison to sputum from CF patients, we could assume a larger cavity size (membrane distance L). Nevertheless, we assumed the membrane distance to be in a range of $0.2\text{-}0.5 \mu\text{m}$, which is justified by the average pore size (approx. $0.2\text{-}0.6 \mu\text{m}$) of pulmonary mucus given by scanning electronic microscopic images (see Fig.1). However, the influence of the particular choice of L is small because of the transient "subdiffusive" behavior, which is not that pronounced for small particles. Naturally, the effective diffusion coefficient is similar to the

D_0 from the unrestricted motion. It seems there is only a minor influence on the diffusion of the small particles due to the membranes.

The situation is different for the MSD curves of bigger particles. The transient "subharmonic" behavior becomes significantly visible and the influence of the permeable membranes becomes dominant. For the simulations of the diffusion of bigger particles, we assumed a larger viscosity η as for the smaller particles. Consequently, D_0 and D_{eff} are smaller as expected from the indicated particle size (see Eq. 2). This is in accordance with the experimental observation: a larger apparent viscosity of the mucus at small time scales due to a particle size comparable with the cavity size because of increased steric obstruction [3]. The finite sized particles are affected by the scaffold structure at any time scale and the assumption of point like tracer particles in the model is not more justified. In addition, we also assume a smaller distance between the membranes, respectively, the mean cavity size is as much smaller as the particle diameter. This assumption is justified by the average pore size (approx. 0.05-0.2 μm) of pulmonary mucus given by scanning electronic microscopic images (see Fig.1), where the pore sizes are extremely small, compared to the particle size. Despite the fact that, the particles will be trapped in the mucus mesh, because the pore size is as much smaller as the particle size, we assumed a $L < 2R$ in our simulations. Nevertheless, in our model, L as mean cavity size is the first order approximation, and the physical meaning should not be overinterpreted in our simplified model, particularly when our particles are assumed as non-extended tracers. Even though, the presented model does not consider chemical or electrostatic effects. However, we are able to reproduce the experimental data of either uncoated (charged) or coated (uncharged) particles, according to the Figures 15-20.

In Table 2 the computed D_{eff} (*) from our simulations (see Figures 15-20) are compared with the corresponding data from other experiments, as shown in Table 1. Only the best fitting data from these studies are presented in comparison with our results.

Table 2: Comparison of the experimentally determined diffusion coefficients with the simulated ones (see column marked with asterisk, red labeled results are from simulated diffusion of particles in sputum from CF patients).

Ref.	Material	Coating	Size [μm]	Barrier	Diff. [μm² s⁻¹]	D _{eff} [μm² s⁻¹] *
[16]	PS	-	0.22	HuCVMu	0.001	0.002 / 0.003
[16]	PLGA	-	0.15	HuCVMu	0.0009	0.002 / 0.003
[16]	PSA	-	0.2	HuCVMu	0.0005	0.0003
[18]	PS	PEG	0.12	HuCVMu	0.002	0.007 / 0.003
[18]	PS	COOH	0.22	HuCVMu	0.0009	0.002 / 0.003
[18]	PS	COOH	0.52	HuCVMu	0.0002	0.0002 / 0.0001 / 0.0005 / 0.0004
[19]	PS	COOH	0.1	BM-biofilm	0.2	0.09
[19]	PS	DMEDA	0.1	BM-biofilm	0.3	0.09
[19]	PS	PEG(2)	0.1	HuCFsputum	0.7	0.09
[19]	PS	COOH	0.1	HuCFsputum	0.2	0.09
[19]	PS	DMEDA	0.1	HuCFsputum	0.2	0.09
[19]	PS	DMEDA	0.1	PA-biofilm	0.04	0.012 / 0.09 / 0.04
[11]	PS	COOH	0.09	HuReMu	0.01	0.012 / 0.009 / 0.04
[11]	PS	PEG	0.1	HuReMu	0.2	0.09
[11]	PS	COOH	0.19	HuReMu	0.001	0.002 / 0.003
[11]	PS	PEG	0.22	HuReMu	0.05	0.02
[11]	PS	COOH	0.51	HuReMu	0.0009	0.0005 / 0.0004

Here, the red labeled effective diffusion coefficients are from the simulated diffusion of particles in sputum from CF patients (see Figures 15 and 16), whereas the remaining diffusion coefficients are from simulated diffusion of particles in human respiratory mucus (see Figures 17 - 20). Surprisingly, the effective diffusion coefficient of some PEGylated 500nm-particles in human respiratory mucus (see [11]) is significantly higher than the simulated one. This may be due to the small accessible time range in the experiments. In our simulations we showed a transient subdiffusive behavior outside the experimentally accessible time range, which leads to a lower effective diffusion coefficient. However, the advantage of our simulations is obvious.

The presented model allows us to calculate the MSD outside the experimental accessible range of measurements, and gives an estimation of the mean time τ_p for particles to pass the mucus layer of $d_m = 55 \mu\text{m}$ thickness. The estimation is given by $\text{MSD}(\tau_p) \sim d_m^2$ and Eq. 20.

$$\tau_p = \frac{d_m^2}{2D_{eff}} \quad (20)$$

Using the assumed D_{eff} from Table 2, this calculation results in a mean passage time τ_p of several hours (see also Table 3). This passage time is significantly higher than the time of

$\tau_{MC} = 15$ min required to renew the layer, given by the mucociliary clearance [4,7,10]. Even for a free Brownian motion ($MSD \sim D_0$) of 200 nm-particles in a fluid with $\eta = 4$ mPas, the passage time is approximately one hour. It can be summarized that particles with a diameter lower than 40 nm are able to pass through the mucus layer of $d = 55$ μm thickness (with a viscosity of the interstitial fluid of $\eta = 7$ mPas) within a mucus turnover time of 15 min. In chapter 4.2, we will calculate the mean passage time and the percentage of particles, passing the mucus layer after a certain specified time range, for each presented experiment, respectively simulation, from Fig. 15-20.

4.2 A model to predict particle diffusion in mucus for short and long time limits

4.2.1 Introduction

Mucus protects our body from environmental influences as it is a biological barrier for foreign substances to the epithelial cell layer, e.g. in the lung. For particle-based drug delivery systems, the mucus layer generates an extra challenge as drug-loaded particles must overcome this layer. Thus, solid drug delivery systems and the penetration of particulate matter, such as viruses, bacteria, and dust are affected. Mucus is a complex, heterogeneous polymer-scaffold with viscoelastic properties, which consists of mainly mucins and of a low viscous interstitial fluid (see Fig. 1). However, the main component of mucus is the interstitial space, which essentially is filled by a fluid with a viscosity, similar to that of water, in the range of a few mPas. To avoid systemic side effects by the therapy of bronchial diseases, e.g. cystic fibrosis, local applications of drug delivery systems are preferable. In the bronchial regions of the lung, pulmonary mucus is present, where its function is the clearance of particulate xenobiotics, mucosal insults, water balance, ion transport, and ion regulation. Some functionalized and non-toxic nanocarriers, loaded with novel pharmaceuticals, can overcome this biological barrier after being inhaled. Inspired from viruses, nanosized particles with neutrally charged coatings such as PEG can efficiently penetrate the mucus layer in contrast to charged particles. Particularly, the studies from Lai et al., Suk et al., Suh et al. and Schuster et al. showed an enhanced penetration of PEGylated particles, compared to conventionally uncoated or carboxylated particles. For comparison, generally the mean squared displacement as a function of the time lag ($MSD(\tau)$) is measured by particle tracking experiments [1-12,14].

So far, the accessible time range in particle tracking experiments is limited by both the frame rate of the camera and the maximal recorded time interval that the diffusing particle is within the depth of field of the microscope for detection. Therefore, the particle diffusion for very short ($\tau < 0.01 - 0.05$ s) and very long ($\tau > 5 - 10$ s) time periods cannot be determined. Due to the fact that in many experiments, the transition from the transient "subdiffusive" regime - which is defined by a transient decrease of the slope of the MSD curve- to the normal diffusion regime is outside the accessible time range, the diffusion is falsely interpreted as an anomalous diffusion (subdiffusion). To predict the diffusivity of particles in confined geometries -such as mucus- in short and long time limits, and also the observed transient "subdiffusive" behavior, in the prior section we introduced a model, based on permeable membranes and an effective diffusion coefficient D_{eff} , which is lower than the diffusion

coefficient D_0 from the Stokes-Einstein relation. This model allows to simulate the MSD of particles in the short and long time limit. In between these limits, a transient "subdiffusive" regime appears, which is also observed in some experimental studies [11, 14]. So, instead of assuming a totally restricted subdiffusion, we showed the diffusion in confined geometries to be partially restricted with a normal diffusive behavior for short and long times, however, the diffusion is described by the diffusion coefficient from the Stokes-Einstein relation D_0 and by an effective diffusion coefficient D_{eff} , respectively.

4.2.2 Model & experimental findings

The Figure 6 suggests the model of mucus, which is based on a porous structure of Newtonian fluid-filled random-sized cavities with apertures of various sizes. The system has been simplified to a simple cubic lattice of cavities with connecting apertures and is characterized by a mean cavity extension L and a mean aperture diameter [see Fig. 6 (A)]. L is the edge size of one cavity in the cubic lattice, respectively the distance between the cavity interfaces. The shown anisotropic scaffold structure in Fig. 6 (A) is condensed by the "boundary homogenization" method assuming permeable membranes in all spatial directions, and quantified by a certain permeability of the membranes p_M for the particles [see Fig. 6 (B) and (C)]. The resulting three-dimensional isotropic system is then further reduced to a one-dimensional system. Despite the numerical iteration scheme, we showed also an analytic approximation, which is the appropriate superposition of the analytic solutions for free and trapped particle diffusion. Sanders et al. showed a microscopic image of sputum from cystic fibrosis (CF) patients, which illustrate the more dense structure of this sputum [13], compared to pulmonary mucus from healthy humans (see Figure 1). Using only the three physical interpretable parameters L , D_0 , and $D_{\text{eff}}(p_M)$, the measured "subdiffusive" behavior from particle tracking experiments can be reproduced. The "subdiffusive" behavior appears due to the continuous transition from normal, unrestricted diffusion $\text{MSD} \sim \tau$ at short times to a normal, restricted diffusion at long-time scales, longer distances respectively. The two limiting normal diffusion regimes are quantized by the diffusion coefficients, D_0 and D_{eff} , respectively. The permeability of the membranes is characterized by p_M , affecting D_{eff} . The third necessary parameter in the model is the mean cavity size L as the only length scale in the system. So, as we assume different values of the permeabilities p_M and the mean cavity size L , we are able to reproduce the experimental data and predict the diffusive behavior of either

uncoated (charged) or coated (uncharged) particles in mucus with different properties for each time scale.

There exist several studies on the particle diffusion in mucus, for instance the investigations by Suh et al. or Schuster et al. [11,14]. Unfortunately, in these studies, the accessible time range is very short (approx. 2-3 decades) and they cannot determine the probability density function (pdf) of the particle displacement in the mucus layer. The latter is important to know, as it provides the percentage of particles, which are passing a specified thickness after a certain time range. Contrary to the pdf, the mean squared displacement (MSD) provides only the mean passage time of one particle. For this reason, we assumed the three essential parameters $D_{\text{eff}}(p_M)$, D_0 , and L to predict the short and long time diffusion, e.g. the MSD over minimum 5 decades, and to determine the pdf.

In the prior section, we presented the experimental studies to determine the diffusivity of particles in pulmonary mucus and finally we calculated the MSD and the effective diffusion coefficient D_{eff} . By assuming specific values for the distance between the permeable membranes L and the permeability of these membranes p_M , we simulated the particle diffusion in mucus in the short and long time limits. We also predicted the effective diffusion coefficient, assuming different values of p_M and L , which are related to the observed structure and pore size distribution of mucus (see Figure 1) and the particle properties. So, the cavity size L is related to the mucus structure, e.g. the pore size, whereas the permeability p_M is affected by the physical and chemical properties of the particles and the mucus. Additionally, in the posterior section we will compute the probability density function of the particle position within the confined geometry (based on repeated permeable membranes in one dimension). Consequently, by assuming different values of L and p_M , affecting D_{eff} , we are able to simulate the particle diffusion in mucus (MSD) and to predict the mean passage time of particles to pass a defined mucus layer thickness, as well as to determine the percentage of particles, passing the mucus layer within a specified time range.

4.2.3 Results & Discussion

The parameters of L , D_0 , and p_M , respectively D_{eff} , from the MSD-calculations in Figure 15-20 are also used to simulate the pdf of the particle displacement after 100 s of Brownian and Fickian diffusion in sputum from CF patients, which is shown in Figure 21 and 22, respectively. The pdf is helpful to calculate the percentage of particles passing a specific mucus layer with a certain thickness.

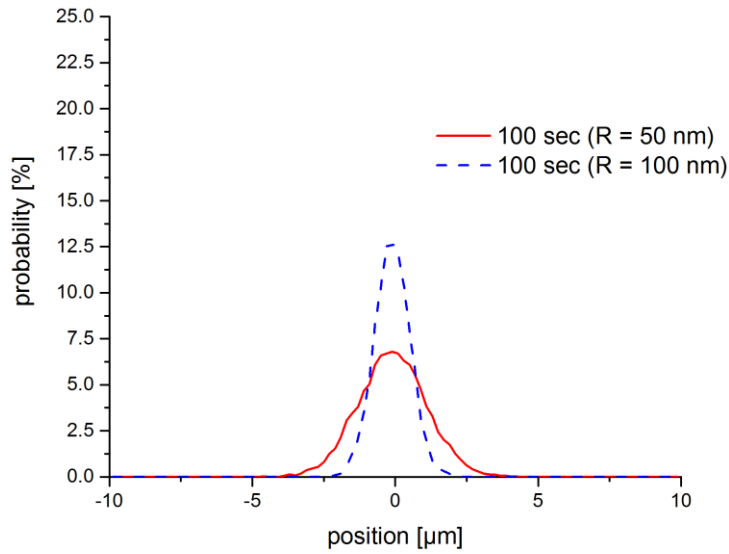


Figure 21: Calculated pdf for various parameters with particle diameters of 100 nm (red solid line) and 200 nm (blue dashed line), as well as a membrane distance $L = 0.5 \mu\text{m}$ for the 100nm-particles and $L = 0.2 \mu\text{m}$ for 200nm-particles. The parameters of D_0 , D_{eff}/D_0 , p_M are given as (top to bottom) $(0.013 \mu\text{m}^2/\text{s}, 0.88, 0.5)$, $(0.007 \mu\text{m}^2/\text{s}, 0.35, 0.3)$.

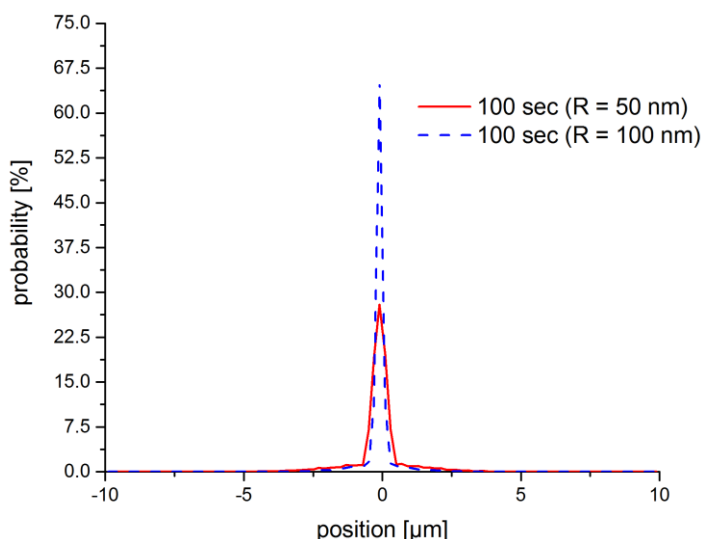


Figure 22: Calculated pdf for various parameters with particle diameters of 100 nm (red solid line) and 200 nm (blue dashed line), as well as a membrane distance $L = 0.5 \mu\text{m}$ for the 100nm-particles and $L = 0.2 \mu\text{m}$ for 200nm-particles. The parameters of D_0 , D_{eff}/D_0 , p_M are given as (top to bottom) $(0.013 \mu\text{m}^2/\text{s}, 0.7, 8)$, $(0.007 \mu\text{m}^2/\text{s}, 0.45, 5)$

We could show that, 50% and 0.03% of the 100nm-particles overcome a distance of 1 μm and 5 μm , respectively, after 100 s. Even 20% of the 200nm-particles overcome a distance of 1 μm within this time. In case of Fickian diffusion (Figure 22), 16% and 0.12% of the 100nm-particles overcome a distance of 1 μm and 5 μm , respectively, after 100 s. 7% of the 200nm-particles overcome a distance of 1 μm within this time. Surprisingly, a higher number of particles overcome a distance of 5 μm by Fickian diffusion, compared to Brownian diffusion, whereas less particles overcome a distance of 1 μm by Fickian diffusion.

The parameters from the simulation of the MSD of carboxylated and PEGylated particles, diffusing in pulmonary mucus are used to simulate the pdf of the displacement of these particles after 100 s. The results are shown in Figure 23 and Figure 24 for the Brownian and Fickian diffusion of carboxylated particles, respectively, and in Figure 25 and Figure 26 for the Brownian and Fickian diffusion of PEGylated particles, respectively. The pdf allows to calculate the percentage of particles passing a mucus layer with a thickness of 1 μm and 5 μm .

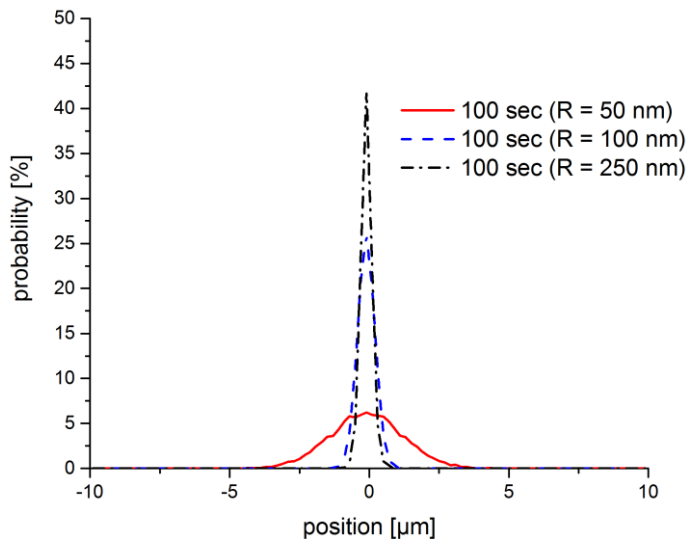


Figure 23: Calculated pdf for various parameters with carboxylated particle diameters of 100 nm (red solid line), 200 nm (blue dashed line), and 500 nm (black dash-dotted line) as well as a membrane distance $L = 0.5 \mu\text{m}$ for the 100nm-particles and $L = 0.15 \mu\text{m}$ for 200nm- and 500nm-particles. The parameters of D_0 , D_{eff}/D_0 , p_M are given as (top to bottom) (0.017 $\mu\text{m}^2/\text{s}$, 0.4, 0.5), (0.004 $\mu\text{m}^2/\text{s}$, 0.09, 0.1), (0.002 $\mu\text{m}^2/\text{s}$, 0.09, 0.05).

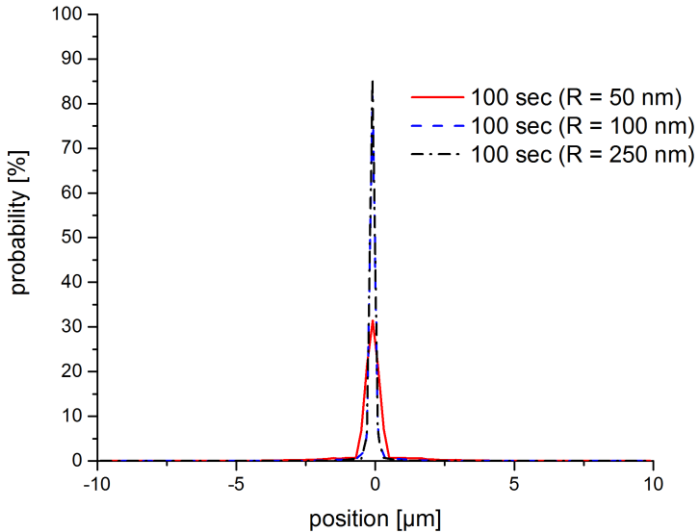


Figure 24: Calculated pdf for various parameters with carboxylated particle diameters of 100 nm (red solid line), 200 nm (blue dashed line), and 500 nm (black dash-dotted line) as well as a membrane distance $L = 0.5 \mu\text{m}$ for the 100nm-particles and $L = 0.15 \mu\text{m}$ for 200nm- and 500nm-particles. The parameters of D_0 , D_{eff}/D_0 , p_M are given as (top to bottom) $(0.017 \mu\text{m}^2/\text{s}, 0.18, 5)$, $(0.004 \mu\text{m}^2/\text{s}, 0.08, 3)$, $(0.002 \mu\text{m}^2/\text{s}, 0.05, 1.5)$.

We show that, after a carboxylation of particles, only 54% and 0.13% of the 100nm-particles overcome a distance of 1 μm and 5 μm , respectively, after 100 s. Compared to the PEGylated particles (see Figures 25 and 26), due to the charged coating (COOH), less (only 2%) of the 200nm-particles overcome a distance of 1 μm after 100 s. However, even 0.03% of the 500nm-particles overcome a distance of 1 μm within this time. In case of Fickian diffusion (Figure 24), 11% and 0.23% of the carboxylated 100nm-particles overcome a distance of 1 μm and 5 μm , respectively, after 100 s. Similar to Brownian diffusion, only 3% of the 200nm-particles overcome a distance of 1 μm after 100 s, whereas significantly more 500nm-particles (0.9 %) overcome a distance of 1 μm within this time. As it is obvious for the uncoated particles in CF sputum (Figures 21 and 22), also a higher number of coated particles overcome a distance of 5 μm by Fickian diffusion, compared to Brownian diffusion, whereas less particles overcome a distance of 1 μm by Fickian diffusion.

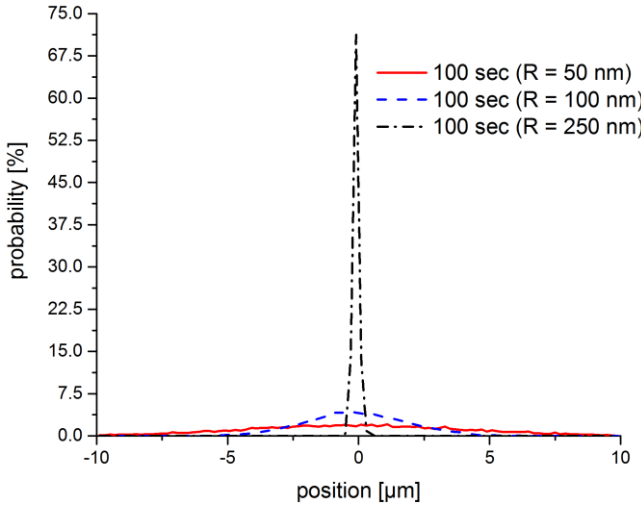


Figure 25: Calculated pdf for various parameters with PEGylated particle diameters of 100 nm (red solid line), 200 nm (blue dashed line), and 500 nm (black dash-dotted line) as well as a membrane distance $L = 0.5 \mu\text{m}$ for the 100nm- and 200nm-particles and $L = 0.15 \mu\text{m}$ for 500nm-particles. The parameters of D_0 , D_{eff}/D_0 , p_M are given as (top to bottom) $(0.1 \mu\text{m}^2/\text{s}, 0.9, 10)$, $(0.05 \mu\text{m}^2/\text{s}, 0.4, 0.5)$, $(0.002 \mu\text{m}^2/\text{s}, 0.2, 0.01)$.

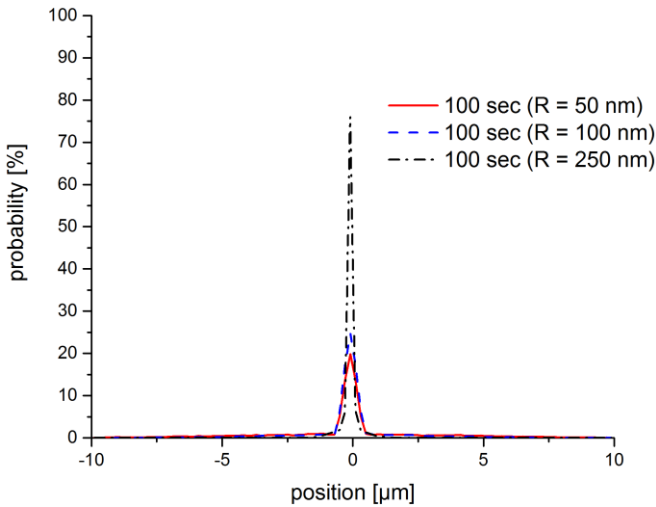


Figure 26: Calculated pdf for various parameters with PEGylated particle diameters of 100 nm (red solid line), 200 nm (blue dashed line), and 500 nm (black dash-dotted line) as well as a membrane distance $L = 0.5 \mu\text{m}$ for the 100nm- and 200nm-particles and $L = 0.15 \mu\text{m}$ for 500nm-particles. The parameters of D_0 , D_{eff}/D_0 , p_M are given as (top to bottom) $(0.1 \mu\text{m}^2/\text{s}, 0.5, 15)$, $(0.05 \mu\text{m}^2/\text{s}, 0.4, 10)$, $(0.002 \mu\text{m}^2/\text{s}, 0.2, 3)$.

Contrary, after PEGylation of particles, 83% and 28% of the 100nm-particles overcome a distance of 1 μm and 5 μm , respectively, after 100 s. Even 68% and 2% of the 200nm-particles overcome a distance of 1 μm and 5 μm , respectively, within this time. Surprisingly, the carboxylation of the 500nm-particles (see Figures 23 and 24) seem to increase the diffusivity, compared to the PEGylated particles. However, the PEGylation of the 100nm-particles lead to an increase of the diffusivity: 0.13 % of these particles overcome a distance

of 10 μm after 100 seconds. In case of Fickian diffusion (Figure 26), 39% and 14% of the 100nm-particles overcome a distance of 1 μm and 5 μm , respectively, after 100 s. 25% and 5% of the 200nm-particles overcome a distance of 1 μm and 5 μm , respectively, within this time. Also for the Fickian diffusion, the PEGylation of particles increases the diffusivity (4 % of the 500nm-particles overcome a distance of 1 μm and 0.08 % of the 100nm-particles even overcome a distance of 10 μm after 100 seconds), compared to a carboxylation.

Finally, we are able to estimate the mean passage time τ_p for particles to pass the mucus layer of $d_m = 55 \mu\text{m}$ thickness, which is given by Eq. 20. We used the D_{eff} from the previously mentioned simulations and some normal diffusion coefficients D_0 to estimate the mean passage time for different sized particles with various coatings, diffusing in healthy mucus and sputum from CF patients. In Table 3, all mean passage times are presented.

Table 3:Summary of the diffusion coefficients, the mean passage times (to overcome a distance of 55 μm), the simulation parameters, the mucus- and the particle properties of the experiments and simulations, which are shown in the Figures 15-26 (the rows in red are from simulated Fickian diffusion).

	$D_0 [\mu\text{m}^2/\text{s}]$	$D_{\text{eff}} [\mu\text{m}^2/\text{s}]$	Mucus	Particle size [μm]	Particle coating	$\tau_p(D_0)$	$\tau_p(D_{\text{eff}})$
R = 50 nm $\eta = 1 \text{ mPas}$	4.54	-	Fluid	0.1	-	5.6 min	-
R = 50 nm $\eta = 10 \text{ mPas}$	0.45	-	Fluid	0.1	-	55.5 min	-
R = 100 nm $\eta = 10 \text{ mPas}$	0.23	-	Fluid	0.2	-	111 min	-
R = 250 nm $\eta = 10 \text{ mPas}$	0.09	-	Fluid	0.5	-	278 min	-
$p_M = 0.01$ $L = 0.15 \mu\text{m}$	0.002	0.0005	Pulmon.	0.5	PEG	210 h	840 h
$p_M = 0.05$ $L = 0.15 \mu\text{m}$	0.002	0.0002	Pulmon.	0.5	COOH	210 h	2100 h
$p_M = 0.1$ $L = 0.15 \mu\text{m}$	0.004	0.0003	Pulmon.	0.2	COOH	105 h	1400 h
$p_M = 0.3$ $L = 0.2 \mu\text{m}$	0.007	0.002	CF	0.2	-	60 h	210 h
$p_M = 0.5$ $L = 0.5 \mu\text{m}$	0.013	0.012	CF	0.1	-	32 h	35 h
$p_M = 0.5$ $L = 0.5 \mu\text{m}$	0.017	0.007	Pulmon.	0.1	COOH	25 h	60 h

$p_M = 0.5$ $L = 0.5 \mu\text{m}$	0.05	0.02	Pulmon.	0.2	PEG	8 h	21 h
$p_M = 10$ $L = 0.5 \mu\text{m}$	0.1	0.09	Pulmon.	0.1	PEG	4 h	5 h
$p_M = 3$ $L = 0.15 \mu\text{m}$	0.002	0.0004	Pulmon.	0.5	PEG	210 h	1050 h
$p_M = 1.5$ $L = 0.15 \mu\text{m}$	0.002	0.0001	Pulmon.	0.5	COOH	210 h	4200 h
$p_M = 3$ $L = 0.15 \mu\text{m}$	0.004	0.0003	Pulmon.	0.2	COOH	105 h	1400 h
$p_M = 5$ $L = 0.2 \mu\text{m}$	0.007	0.003	CF	0.2	-	60 h	140 h
$p_M = 8$ $L = 0.5 \mu\text{m}$	0.013	0.009	CF	0.1	-	32 h	47 h
$p_M = 3$ $L = 0.5 \mu\text{m}$	0.017	0.003	Pulmon.	0.1	COOH	25 h	140 h
$p_M = 10$ $L = 0.5 \mu\text{m}$	0.05	0.02	Pulmon.	0.2	PEG	8 h	21 h
$p_M = 15$ $L = 0.5 \mu\text{m}$	0.1	0.04	Pulmon.	0.1	PEG	4 h	11 h

As obvious, the mean passage times of all particles in mucus are significantly higher than the mucociliary clearance time, which is assumed to be 15 minutes. So, none of these -uncoated or coated- particles are able to overcome a mucus layer of 55 μm before being transported out of the lung. However, the mucus turnover time is significantly higher in case of cystic fibrosis mucus, which maybe lead to comparable mean passage times.

Furthermore, we calculate the maximal diameter of a particle, which can pass a fluid layer with a viscosity of 1mPas and a thickness of 55 μm within the mucus turnover time of 15 min. Additionally, we also calculate the maximal viscosity of the fluid, which allows a particle with a diameter of 100nm to overcome a distance of 55 μm within the mucociliary clearance time of 15 min. Only extremely small particles with a diameter below 300 nm can overcome a fluid layer with a thickness of 55 μm (no restrictions due to apertures or membranes) within the mucus clearance time, if the fluid viscosity is that of water. 100nm-particles can overcome this distance within 15 min only if the fluid viscosity is not higher than 3 mPas. Due to the fact, that we simulated passive Brownian motion, some active movement processes of the particles should increase the diffusivity. However, in case of cystic fibrosis sputum, the mucus clearance time is significantly higher, which leads to comparable mean passage times.

4.3 Modeling and Simulation of Fickian diffusion based on concentration gradients and comparison with a Brownian diffusion model

4.3.1 Introduction

The former presented models are based on random particle trajectories and permeable membranes [see Fig.6 (B)], however the following one is based on concentration gradients and rigid walls with apertures [see Fig.6 (A)]. The aim of simulating the diffusion in this aperture-model is to compare it with the membrane-model and subsequently to achieve a relation between the physically interpretable aperture- or pore-size and the abstracted permeability of the membranes.

In contrast to the former models, here we do not solve stochastic differential equations based on the Langevin equation, namely Brownian diffusion, but we solve partial differential equations (PDE) based on the Fickian law, namely Fickian diffusion. The discretization is done by the Finite Element Method, which will be presented in the following section. So, for each time step we yield the concentration profile of the particles as diluted species within the presented geometry. Therefore, a mesh has to be generated and the PDE has to be solved in each mesh cell for each time step. Contrary to the former models, which are considered in one spatial dimension, here we have to consider a two-dimensional model, due to the fact, that we assume the diffusion in y-direction to be totally restricted, but in the x-direction we assume a partially restricted diffusion. The meshing of the geometry and simulation of the Fickian diffusion is done with Comsol Multiphysics.

4.3.2 Fickian and Brownian diffusion models

The Finite Element Method (FEM) was initially developed to analyze problems in structural mechanics. Currently, the FEM is used in many fields of science and engineering, such as mechanics, fluid dynamics, chemical engineering, and heat transfer problems. To apply the FEM, some initializing has to be done, which are the computer-aided design (CAD) of the geometry, the choice of the essential system of equations with specified boundary conditions, the meshing of the geometry, and the choice of the appropriate solver. There are several assumptions to make before solving the mathematical equations, e.g. concerning the geometry, the material laws, the boundary conditions, and the meshing. In particular, the latter

is very important to achieve reliable results, as a finer mesh leads to a higher accuracy of the solution, but also to a higher computation time. Contrary, if the mesh is too coarse, the solution may not converge. There are further problems in executing FEM-simulations, which can appear: in case of missing boundary conditions, the solution also may not converge, and if the time step in the time-dependent solver is too small, this leads to an excess of the necessary memory capacity of the processor. So, all these assumptions have to be made before starting the computation by the processor. The processor itself has to discretize the domains of the geometry (pre-processing), build the system of equations with the respective boundary conditions, and finally solve them. The post-processing means the visualization and evaluation of the results. Detailed information of the theoretical fundamentals of FEM, such as the use of appropriate test and initial functions, can be found in several references, e.g. [61-64]. For each shown simulation, which is based on the FEM, we used the optimal mesh element size, as the elements are small enough to achieve a convergence of the solution, but not too fine to avoid extremely high computation times and necessary memory capacities. We found a maximal mesh element size of approximately two thirds of the minimal geometry size. The optimal mesh element size is approx. one third of the minimal size of the geometry.

The diffusion of diluted species -here, the diluted species are the particles in the interstitial fluid- is given by the 2nd Fickian law:

$$\frac{\partial c}{\partial t} + \nabla(-D_0 \nabla c) = 0 \quad (21)$$

with the concentration c of the diluted species in a fluid, respectively the concentration of particles in the interstitial fluid.

To simulate the restricted Fickian diffusion in a confined geometry, two models will be applied in this work, which are shown in Fig. 27 and Fig. 28. The first model has been realized by two infinitely thin impermeable walls with a gap distance d_p , which accords to the size of the open windows [see Fig. 6 (A)]. The second model represents an array of squared cells with length L , each cell with a different diffusion coefficient D_{eff} , and separated by thin (thickness $A = 10$ nm) diffusion barriers without any gap, respectively permeable membranes [see Fig. 6 (B)].

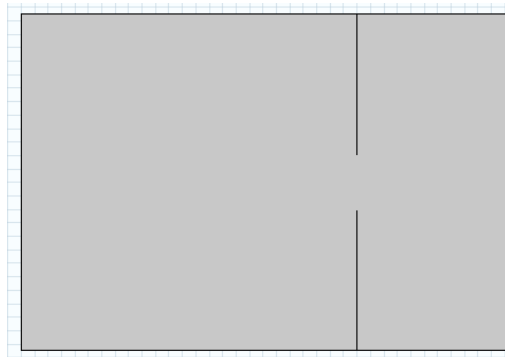


Figure 27: Cell-window model of the mucus to simulate particle diffusion in a cell with one open window and thin impermeable walls.



Figure 28: Cell-array model of the mucus to simulate particle diffusion in a cell with an array of thin diffusion barriers, each with different diffusion coefficients, shown as different shades of grey (the darker the grey, the higher is the assumed diffusion coefficient).

We discriminate two forms of the cell-array model, which differ from the regions with the assumed diffusion coefficients: one model contains different diffusion coefficients in the cells as well as in the walls (lower Figure in Fig. 28) and the second model contains different diffusion coefficients only in the walls, respectively the diffusion barriers (upper Figure in Fig. 28).

The initial concentration at the left boundary as source of diffusion has been set to a value of 1 mol m^{-3} . A mesh with homogeneous triangular elements and an element size between minimum 1 and maximum 10 nm is built. To solve the differential equation system, a parallel sparse direct time dependent solver -with a discrete time step $\Delta t = 10 \text{ ms}$ - is used.

4.3.3 Results & Discussion

In a first model of mucus we assume a squared box -namely the mucus cell- with a single open window -namely the mucus pore- in one spatial dimension (see Fig. 27). By varying the size of this window, the probability of a particle to pass one mucus cell is expected to change. In this section, we simulate the Fickian diffusion of particles in a 500 nm-sized cell with one pore. We used pore sizes of $d_p = 100$ nm, 200 nm, 300 nm, and 400 nm. The diffusion coefficient inside each mucus cell is assumed to be $0.32 \mu\text{m}^2 \text{s}^{-1}$.

We determine the concentration of 200 nm-particles as diluted species in a distance to the window of 50 nm at each position in front of and behind the window (+ and -), and the difference of the (+)- and the (-)-concentration. We expect the time dependent difference of the concentrations to approximate different constant values, dependent on the size of the mucus pore d_p . So, the higher d_p , the lower the difference should be, because there will be a compensation of the concentration in the front of (+) and behind (-) the pore.

The Figure 29 shows the concentration profile of the 200 nm-particles as diluted species in a 500 nm-sized cell after 10 sec. The pore size d_p is set to a value of 100 nm.

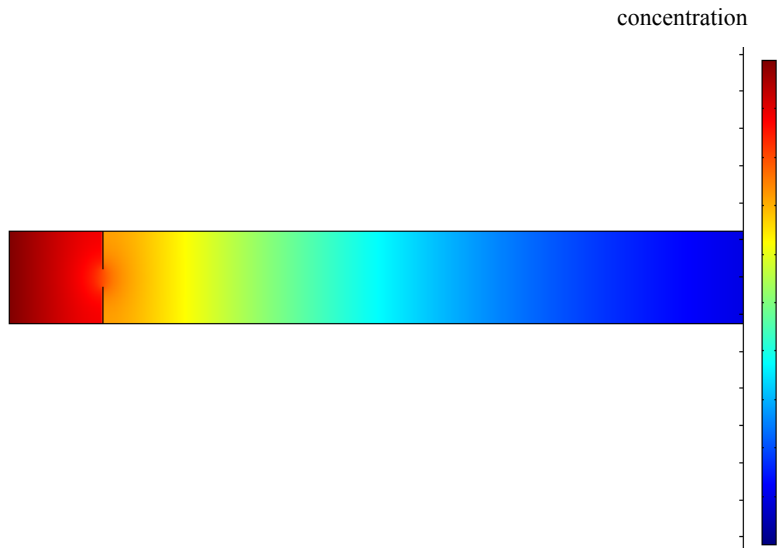


Figure 29: Concentration profile in a cell-window model with $D_0 = 0.32 \mu\text{m}^2/\text{s}$, $L = 500$ nm, and $d_p = 100$ nm after $\tau = 10$ s.

In Fig. 30 the difference of the (+)- and the (-)-concentration is plotted against the diffusion time for different pore sizes d_p . Here, the approximation to a constant value is obvious, particularly for larger d_p , whereby the difference will be zero for $d_p = L$.

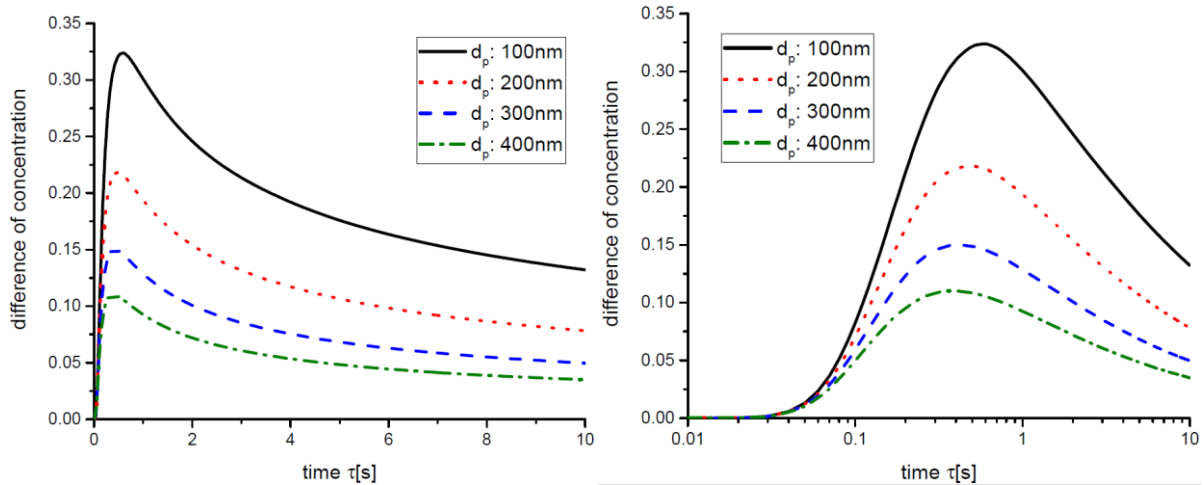


Figure 30: The time-dependent difference of the concentration at the left (-) and at the right (+) side of the window in a cell-window model ($D_0 = 0.32 \mu\text{m}^2/\text{s}$, $L = 500 \text{ nm}$) for different window sizes d_p .

To compare the pore size d_p , used in these simulations, with a transmission probability, respectively a permeability p_M , of particles to pass a permeable membrane, we also did some numerical simulations of the Brownian and Fickian diffusion (see chapter 4.1). The results of this comparison are shown later in this section.

Additionally, we calculate the mean squared displacement (MSD) of the particles as diluted species, as given by:

$$MSD_c = c(x)x^2 \quad (22)$$

with the concentration $c(x)$ at position x .

For short times ($\tau \rightarrow 0$) and length scales, the slope of the MSD curve should be equal to one in a double logarithmic plot. We expect the slope to decrease, if the mucus pore becomes smaller, whereas the slope should increase again after awhile, due to the unrestricted diffusion beyond the mucus pore.

The following Figures 31 and 32 show what happens, if we increase the number of the windows in our cell-window model. The size of the cells stay constant, but we inserted additional neighbored cells, respectively windows, in the geometry, shown in Figure 27. The influence of the repetition of the cells and windows is obvious in Figures 31 and 32.

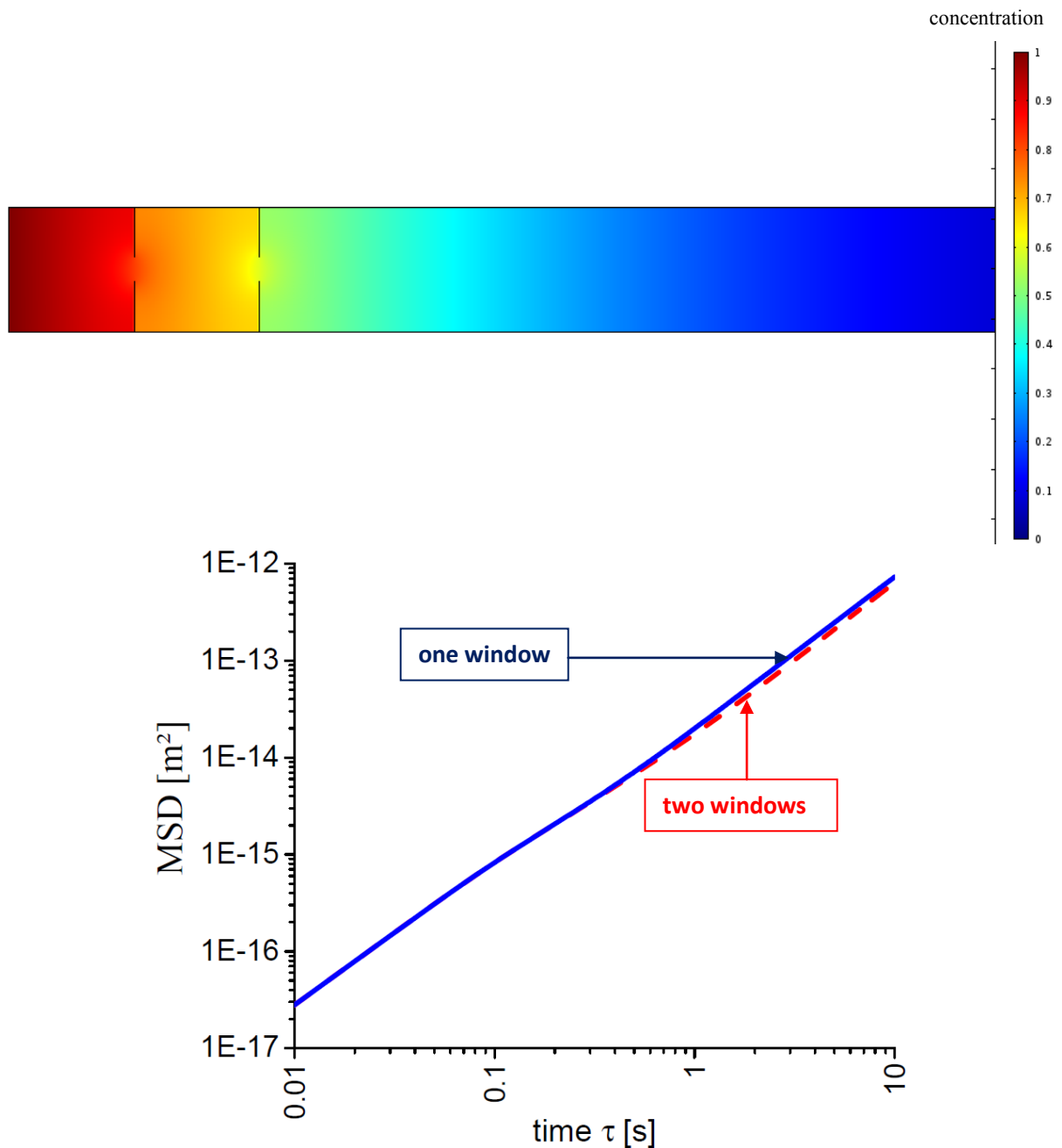


Figure 31: Concentration profile with $D_0 = 0.32 \mu\text{m}^2/\text{s}$, $L = 500 \text{ nm}$, and $d_p = 100 \text{ nm}$ after $\tau = 10 \text{ s}$ and MSD of the particles as diluted species in a cell-window model with two windows ($D_0 = 0.32 \mu\text{m}^2/\text{s}$, $L = 500 \text{ nm}$, $d_p = 100 \text{ nm}$).

Here, the blue line shows the MSD ($D_0 = 0.32 \mu\text{m}^2/\text{s}$) with one window ($d_p = 100 \text{ nm}$), whereas the green line shows the MSD with two windows. As obvious, the MSD decreases with a higher number of restrictions, represented as walls with windows. In Fig. 32, this effect becomes more significant. Approximately after 0.2 seconds, the diffusion is no longer free (decreased slope of the MSD curve), but becomes more restricted due to the walls between the cells. After approx. 2 seconds, the slope of the MSD curve again approximates to unity. The transient regime between 0.2 and 2 seconds is therefore called "subdiffusive".

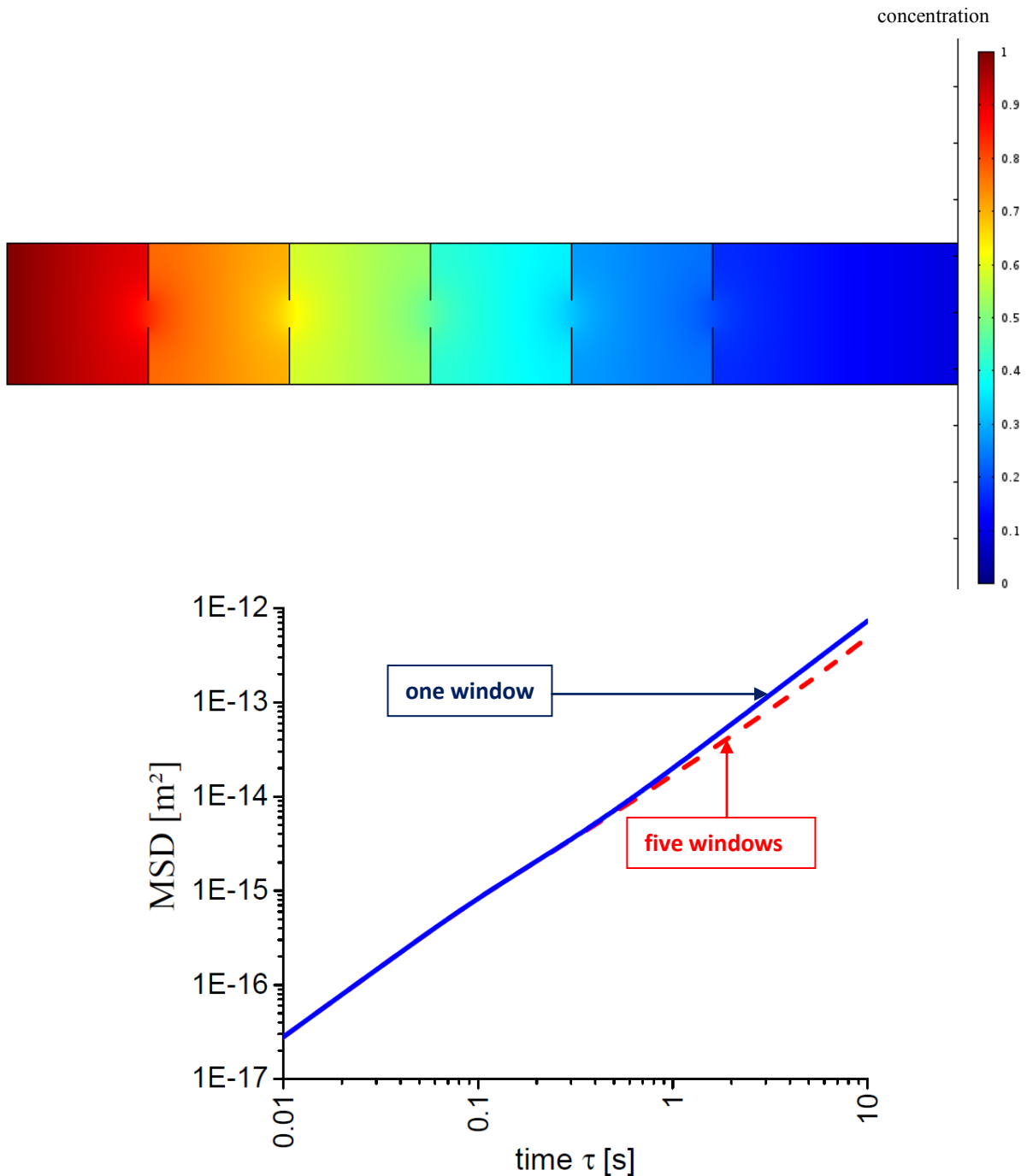


Figure 32: Concentration profile with $D_0 = 0.32 \mu\text{m}^2/\text{s}$, $L = 500 \text{ nm}$, and $d_p = 100 \text{ nm}$ after $\tau = 10 \text{ s}$ and MSD of the particles as diluted species in a cell-window model with five windows ($D_0 = 0.32 \mu\text{m}^2/\text{s}$, $L = 500 \text{ nm}$, $d_p = 100 \text{ nm}$).

Here, we use five walls with windows as restrictions to a free diffusion. With a higher number of cells and windows, the "subdiffusive" regime becomes more obvious, due to the reduced slope of the MSD curve, but after awhile, this slope begins to increase again to a value of one. So, this "subdiffusive" regime is transient, as the diffusion will be normally again with a slope of one, but with a significantly lower diffusion coefficient D_{eff} , resulting in a lower MSD, compared to a free diffusion ($\text{MSD} \sim D_{\text{eff}}$ instead of $\text{MSD} \sim D_0$).

So, a realistic model of the cell-window geometry can be achieved by periodically appearing windows. In Fig. 33, the MSD of 200nm-particles as diluted species ($D_0 = 0.32 \mu\text{m}^2 \text{s}^{-1}$) in a cell with different sized windows is shown. Here, we use totally 15 walls and windows to simulate a more realistic partially restricted diffusion.

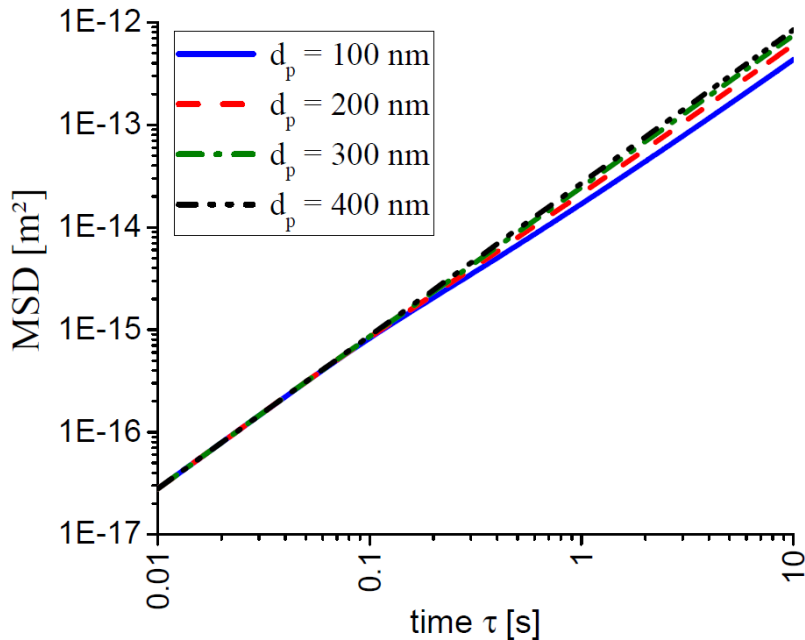


Figure 33: MSD of the particles as diluted species in a cell-window model with different values of the window size d_p
 $(D_0 = 0.32 \mu\text{m}^2/\text{s}, L = 500 \text{ nm})$.

Here, the influence of the window size is obvious. The smaller the window, the lower the effective diffusion coefficient at $\tau \rightarrow \infty$. After 0.2 sec, the slope of the MSD curve is significantly lower than one, which can be interpreted as a "subdiffusive" behavior. However, after 2 sec, the behavior is normally again, so the "subdiffusive" behavior is a transient effect.

Additionally, in a further model we assume the mucus to be an array of cells in one spatial dimension, each restricted by a thin ($A = 10 \text{ nm}$) diffusion barrier (Fig. 28) with different effective diffusion coefficients, decreasing in direction of the concentration gradient. At first, we assume the diffusion coefficient inside each mucus cell to be $0.32 \mu\text{m}^2 \text{s}^{-1}$ with decreasing effective diffusion coefficients within the diffusive barrier (upper Figure in Fig. 28). Despite this assumption, in a second model, we also assume the diffusion coefficient inside the cells to decrease (lower Figure in Fig. 28). Consequently, we assume the effective diffusion coefficient inside the mucus cell being equal to the diffusion coefficient within the corresponding diffusion barrier.

We will determine the time dependent concentration profile of the 200nm-particles as diluted species in a 500 nm-sized cell (Figure 34 and Figure 35), as well as the mean squared displacement of these particles (Figure 36).

If we assume a decreasing diffusion coefficient only within the diffusive barriers, the concentration profile is shaped, similar to a Gaussian distribution (Figure 34). In contrast, if we assume decreasing diffusion coefficients in the diffusive barriers, as well as in the cells, the shape of the concentration profile is totally different for longer time scales (Figure 35). However, there are several sudden drops of the concentration and the drops become more sharp for longer length and time scales. Furthermore, in Figure 35 the unstable course of the concentration profile for longer time scales is obvious, compared to the smooth course in Fig. 34. However, the concentration profile in Fig. 35 is more realistic for a restricted diffusion, as similar to the cell-window model, here we have a significant difference in the concentration on the left side and on the right side of each window or diffusive barrier. So, if we compare the MSD-course of the cell-array model with it from the cell-window model, the appearing anomalous behavior is obvious for both models and is expected to be periodically in time, since the restrictions appear periodically in the geometry.

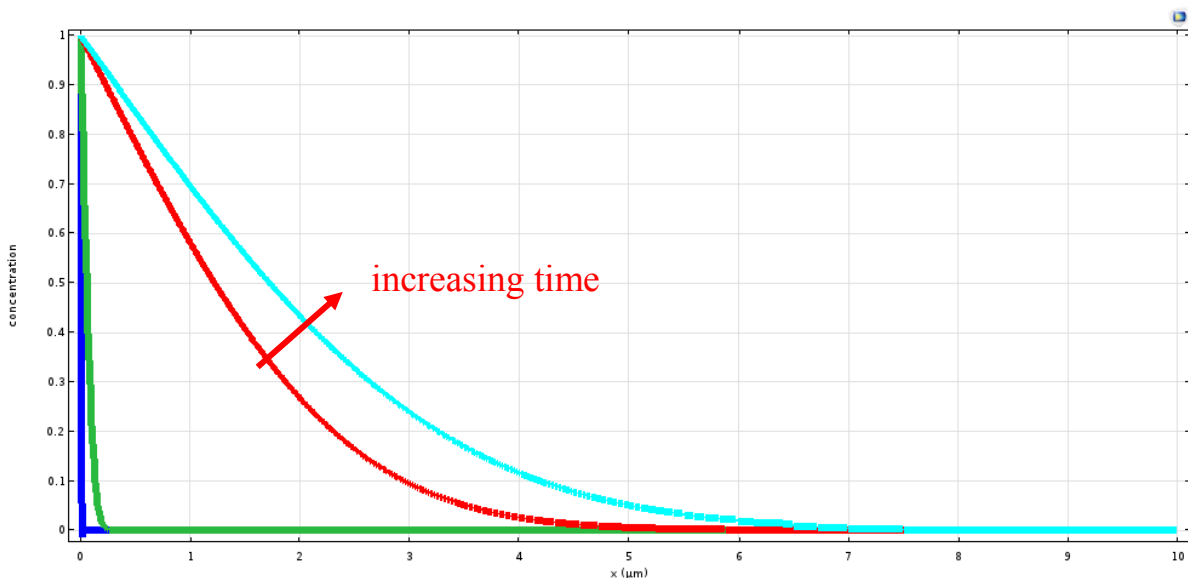


Figure 34: Time-dependent concentration profile of a cell-array model with $D_0 = 0.32 \mu\text{m}^2/\text{s}$ ($L = 500 \text{ nm}$) in each cell and decreasing diffusion coefficients ($L = 500 \text{ nm}$) only in the diffusive barriers for the following times: $\tau = 0, 0.01, 5, 10 \text{ sec.}$

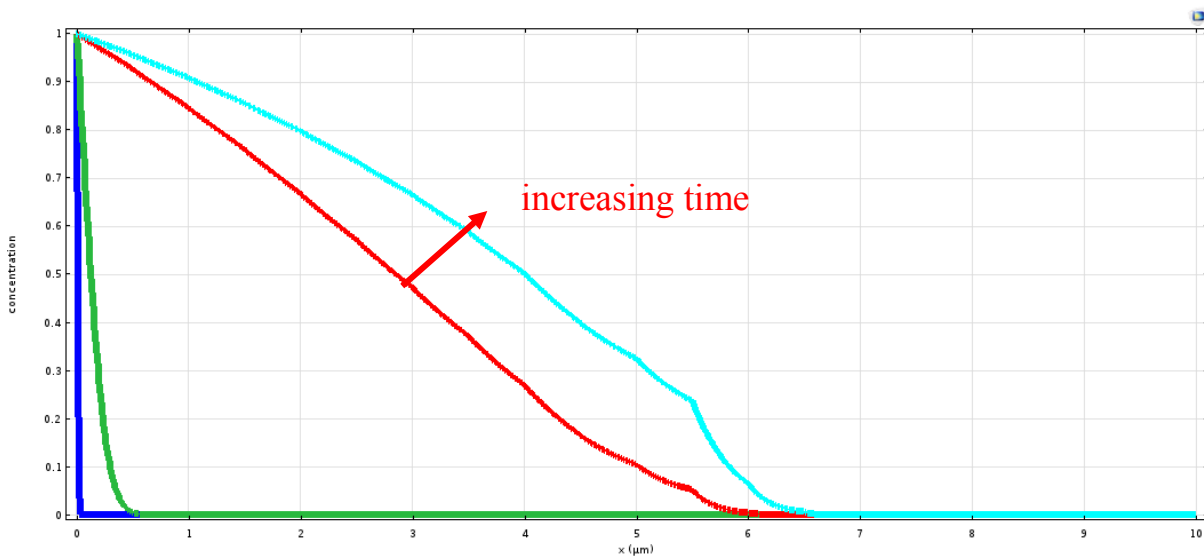


Figure 35: Time-dependent concentration profile of a cell-array model with decreasing diffusion coefficients ($L = 500 \text{ nm}$) in the diffusive barriers and in the cells for the following times: $\tau = 0, 0.01, 5, 10 \text{ sec}$.

We expect the mean squared displacement to increase over time, but with a lower slope of the curve, plotted in a double logarithmic way, compared to a free diffusion without any diffusion barriers. The Figure 36 shows the MSD of 200nm-particles as diluted species, calculated by the concentration profile from Figure 34 (red dashed line) and Figure 35 (blue straight line), respectively. A simulation time of totally 10 sec (left Figure) and 100 sec (right Figure) was used.

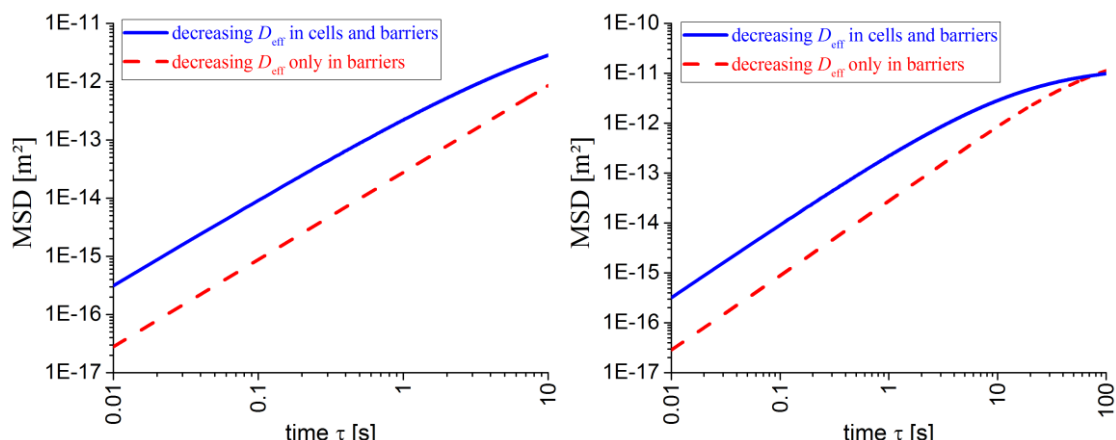


Figure 36: MSD of a cell-array model with $D_0 = 0.32 \mu\text{m}^2/\text{s}$ ($L = 500 \text{ nm}$) in each cell and decreasing diffusion coefficients only in the diffusive barriers (red dashed line), and MSD of a cell-array model with decreasing diffusion coefficients ($L = 500 \text{ nm}$) in the diffusive barriers and in the cells (blue straight line). A simulation time of totally 10 sec (left Figure) and 100 sec (right Figure) was used.

In this cell-array model, it seems, that the MSD will be constant for $\tau \rightarrow \infty$, if the diffusion coefficient decreases in the cells and in the diffusive barriers as well (blue solid lines). The same holds true, if the diffusion coefficient decreases only within the diffusive barriers (red dashed lines), however, this will be obvious for significant longer time scales (see right Figure in Fig. 36). So, contrary to the cell-window model, here the transition from a "subdiffusive" to a normal diffusive regime (with $D_{\text{eff}} < D_0$, $\alpha \leq 1$) does not appear, but the effective diffusion coefficient will be zero for $\tau \rightarrow \infty$ (similar to $d_p = 0$ in the cell-window model).

If the diffusion coefficient decreases in the cells and in the diffusive barriers as well, as it is shown in Fig. 35 and Fig. 36 (blue straight lines), the assumed diffusion coefficient in the first half of the cell-array is higher than the assumed diffusion coefficient of $0.32 \mu\text{m}^2 \text{s}^{-1}$ in the cells of the model with decreasing diffusion coefficients only within the diffusive barriers, as it is shown in Fig. 34 and in Fig. 36 (red dashed lines), whereas in the second half of the cell-array it is lower. This is the reason, why the MSD-values and the diffusion coefficient for short times are significantly lower, but the slope of this MSD-curve as well as the absolute value of the MSD for large time scales are higher in the latter model (red dashed lines in Fig. 36) than that of the former (blue straight lines in Fig. 36).

As shown in the MSD-plots of these two cell-array models, to get a realistic model, we have to combine these cell-array models. So, a realistic model of the cell-array geometry would contain only two different diffusion coefficients, whereat these coefficients have to be defined inside the cells, as well as in the diffusion barriers. The first half of the cell-array has to be provided with one constant diffusion coefficient D_0 and the second half of the cell-array has to be provided with a lower (constant) effective diffusion coefficient D_{eff} . This would yield the same transient "subdiffusive" effect, as it is obvious in the cell-window model. For short times, the diffusion is free with $\text{MSD} \sim D_0$ and for longer times, the diffusion is partially restricted, but also with a slope of the MSD curve equal to one (normal diffusion with $\text{MSD} \sim D_{\text{eff}}$). So, we have to assume a free diffusion with a diffusion coefficient D_0 for short times, a restricted diffusion with an effective diffusion coefficient of $D_{\text{eff}} < D_0$ for longer times, and naturally a transient "subdiffusive" regime, where a transition of the diffusion coefficients appears.

Finally, we are able to achieve a qualitatively relation between the permeability p_M from the numerical simulation of the diffusion as a random walk (Brownian motion) of particles, based on permeable membranes, and the window size d_p from the numerical simulation of the Fickian diffusion with diluted species, based on concentration gradients.

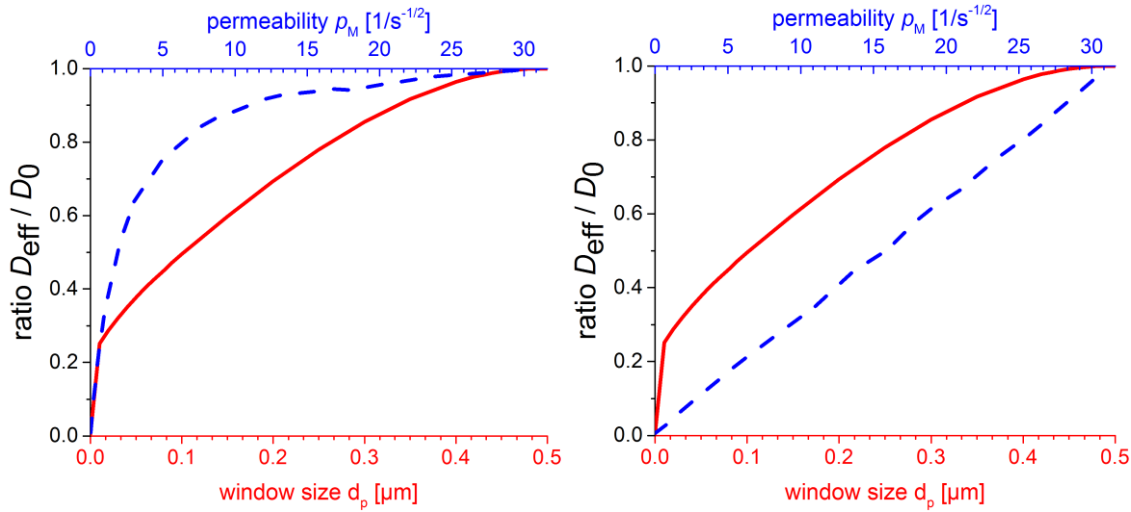


Figure 37: Ratio of D_{eff} and D_0 for different values of p_M (numerical simulation of the diffusion, based on permeable membranes with $L = 500$ nm and $D_0 = 0.32 \mu\text{m}^2/\text{s}$; blue dashed line), compared with the results of the numerical simulation with different sized windows, based on concentration gradients (red straight line). The permeability is defined from 0 to 31.6 for $\Delta t = 1$ ms and the window size is defined from 0 to $L = 500$ nm (left Figure: numerical simulation of Brownian diffusion; right Figure: numerical simulation of Fickian diffusion; both based on permeable membranes).

In Fig. 37, surprisingly, the agreement between the two diffusion models (based on permeable membranes and based on concentration gradients) is obviously higher for the numerical simulation of the Brownian diffusion (left Figure). However, we expected the agreement between these two models being higher for the numerical simulation of the Fickian diffusion, based on permeable membranes, as it is closer to the assumption of the cell-window model, based on concentration gradients.

Nevertheless, we could show that there is a relation between the physically interpretable window-, respectively pore-size of the cell-window model, which represents the mucus-pore structure, and the permeability of the membranes in our abstracted numerical model.

The following Figures 38 and 39 show the resulting MSD from numerical simulations of the Fickian and the Brownian diffusion, respectively, with different p_M , equivalent to the results from the cell-window model in Fig. 33. In addition, the differences in concentration -here, concentration means the number of particles in relation to the total particle number- are presented for the simulated Fickian and Brownian diffusion (right Figures). Hereby, difference means the difference of the relative particle number in a distance to the permeable membrane of 50 nm at the positive (+) and negative (-) position, equivalent to the results from the cell-window model in Fig. 30.

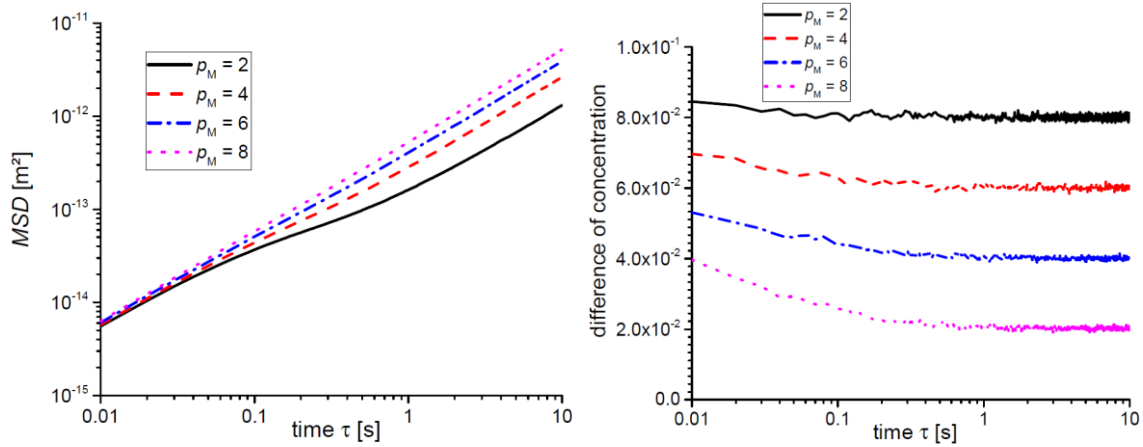


Figure 38: Simulated MSD (left Figure) and the difference of concentration, respectively relative number of particles (right Figure), for Fickian diffusion of 200nm-sized particles with $D_0 = 0.32 \mu\text{m}^2/\text{s}$, $L = 500 \text{ nm}$, and different permeabilities. The time-dependent difference of the concentration (here, concentration means the relative number of particles, compared to their total number) has been calculated from the concentration at the left (-) and at the right (+) side of the permeable membrane.

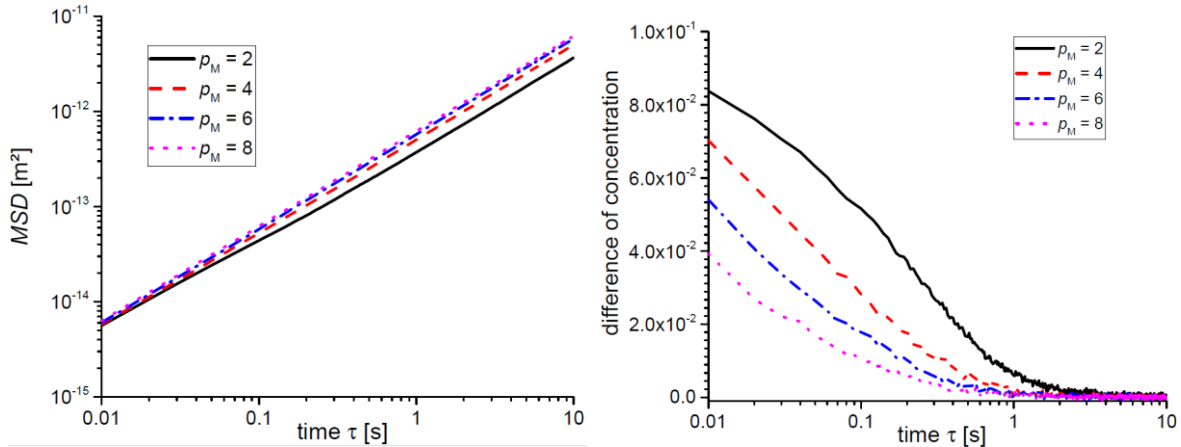


Figure 39: Simulated MSD (left Figure) and the difference of concentration, respectively relative number of particles (right Figure), for Brownian diffusion of 200nm-sized particles with $D_0 = 0.32 \mu\text{m}^2/\text{s}$, $L = 500 \text{ nm}$, and different permeabilities. The time-dependent difference of the concentration (here, concentration means the relative number of particles, compared to their total number) has been calculated from the concentration at the left (-) and at the right (+) side of the permeable membrane.

Here, the transient anomalous ("subdiffusive") behavior becomes more obvious for the Fickian diffusion, compared to the Brownian diffusion.

As already shown in Fig. 30, also here the difference of the concentration approximates to a constant value for $\tau \rightarrow \infty$ and will be zero for $p_M = \infty$ (equivalent to $d_p = L$), in case of the simulated Fickian diffusion. The simulation of the Brownian diffusion results in a difference of zero for $\tau \rightarrow \infty$, independent on the permeability of the membrane, which only affects the values at $\tau \rightarrow 0$.

4.4 Conclusions

We presented a model based on a cellular structure with permeable membranes [27] to explain the experimental observed transient "subdiffusive" behavior of nanoparticles in mucus. We applied this model to reproduce the MSD-curves from published particle tracking experiments.

We showed that it is possible to predict the particle diffusivity in mucus for short and long time limits by an in-silico model, based on permeable membranes. Therefore, we have to assume only three parameters, which are the distance of the membranes L , the diffusion coefficient for short time limits D_0 , and the permeability of the membranes p_M , resulting in a diffusion coefficient for long time limits D_{eff} . We are able to replace particle-tracking experiments by numerical simulations, if we know the properties of the particles and the investigated mucus. Different particle coatings and particle sizes, as well as the mucus properties lead to specific permeabilities p_M , and the mucus pore-, respectively mesh-size is related to the mean cavity size L . Naturally, the particle size and the permeability affects the diffusion coefficient for short D_0 and long D_{eff} time limits, respectively.

Additionally, we showed different mean passage times and percentages of particles, passing the mucus layer for various assumptions of L and p_M , as well as for certain particle and mucus properties. The advantage in using our model is obviously, that we are able to calculate the MSD and to determine the corresponding pdf for the short and long time limits, which is currently not possible with experimental methods. In experiments, the MSD only in a short time range is measureable and the measurement of the pdf is still a current topic. However, by the usage of our model, one can compute the MSD and the pdf, both in large time ranges and just by assuming only three essential parameters. These parameters contain all physical and chemical properties of mucus and of the particles.

Due to its confined geometry, mucus is shown to be an excellent heterogeneous material model to predict the transient "subdiffusive" regime within the experimentally measurable time range. The model includes two physically interpretable diffusion coefficients $D_0(\eta;R)$ for shorter times and $D_{eff}(p_M)$ for longer times, as well as the distance L between the membranes. The assumed viscosity of the interstitial fluid is similar to that of water. The permeability of the membranes is characterized by p_M , affecting D_{eff} . We discussed a heuristic analytic approximation formula for the $MSD(\tau)$ with the parameters D_0 , D_{eff} , and L . The approximation was substantiated by detailed numerical simulations based on permeable

membranes in analogy to Robin boundary conditions. The model predicts a normal diffusive behavior for short and long times. A "subdiffusive" regime appears only in between these times, if the impermeability of the membranes is dominant. In agreement with experimental data, we can conclude that particles with a diameter lower than 40 nm are able to pass through the tracheobronchial mucus layer (thickness $d_m \approx 55 \mu\text{m}$, interstitial fluid viscosity $\eta = 7 \text{ mPas}$) within a clearance time of 15 min by passive Brownian motion. Only extremely small particles with a diameter below 300 nm can overcome a fluid layer with a thickness of 55 μm within the mucus clearance time, if the fluid viscosity is that of water. 100nm-particles can overcome this distance within 15 min only if the fluid viscosity is not higher than 3 mPas. To enable the mucopenetration of particles, as reported for some viruses or some drug delivery systems [1,2,3], other transport mechanisms and effects must be involved. Patients with cystic fibrosis suffer from a significantly reduced mucociliary clearance, due to higher viscosities [7,13,14,19,23-25]. Consequently, the probability for inhaled particles to overcome the CF mucus layer is significantly higher.

In the last part of this section, we developed two two-dimensional models, based on a cell array, on the one hand with periodic open windows and on the other hand with periodic diffusion barriers. These models are based on a concentration gradient diffusion (Fickian diffusion) and we concluded, that both models can be reduced to the first presented one-dimensional model, based on permeable membranes. Additionally, we could show the relation between the permeability p_M and the open window size d_p , whereat the former is easy to handle to simulate the diffusion process, whereas the latter is more interpretable, since d_p can be achieved more easily from microscopic images of mucus.

5 Mechanical and Rheological Properties of Mucus

5.1 Introduction

5.1.1 Macro- and microrheology of mucus

Mucus is a biological hydrogel with a highly inhomogeneous and complex structure with unique viscoelastic properties [3,9,65-68]. As a consequence mucus represents also an important biological barrier that prevents immediate access to the surface of mucosal epithelial cells which holds for both molecules as well as particles. Macrorheological properties, which are expressed by the elastic storage and the viscous loss modules, G' and G'' respectively, can be determined for the entire mucus structure as a consequence of a reshape and reorientation of the mucin fibers. Both parameters are generally determined by frequency- and amplitude-sweeps in a rheometer. Microrheological properties are expressed by the viscosity of the interstitial fluid and the elasticity of single mucin fibers. Latter can be determined by active measurements, using optical tweezer, whereas the viscosity of the interstitial fluid is determined by passive Brownian motion. In rarely cases, also a meso-phase rheology is described by the retarded movement of Brownian particles due to steric hindrances [3]. This restricted movement of particles by topological properties of the mucus mesh has been investigated in the first part of this work.

5.1.2 Viscoelastic properties of mucus

In the same way as mucus function may differ from organ to organ (e.g., lubrication, protection, etc.), its viscoelastic properties are also likely to be different according to the respective biological needs. In order to address this hypothesis, we have chosen to compare mucus from the intestinal and the respiratory tract as mucus from either organ has to perform rather different functions. The pig was chosen as mucus from this source can be obtained relatively easily, also considering ethical aspects. To compare the viscoelastic properties, the elastic storage as well as the viscous loss modules will be measured by different methods, regarding micro- and macroscopic length scales. The elastic storage module G' describes the elastic part -similar to a spring constant- of the mucin fibers, whereas the viscous loss module G'' describes the viscous, dampening part of the fluid.

In the first part of this thesis, we assumed the fluid to be purely viscous, which is expressed by a constant fluid viscosity, independent on the shear rate (see Fig.1 in [3]), and we also assumed the permeable membranes to be rigid. These assumptions were made to simulate the Brownian motion of freely diffusing particles inside the mucus mesh (microscopic rheology). To simulate the mechanical behavior of the mucin fibers, respectively the entire mucus structure (macroscopic rheology), we assume the fibers to be linear elastic, which is expressed by constant Young's modules, linear dependent on the shear rate (see Fig.1 in [3]). These assumptions are in good agreement with the real viscoelastic properties of mucus, where the mucin fibers are known to be semiflexible, and the interstitial fluid is known to be purely viscous with a viscosity, similar to that of water, typically in the order of few mPas. However, the entire mucus structure has viscoelastic properties.

The following Table 4 shows different values for the G' and G'' , as well as different macrorheological viscosities of mucus from various species and organs.

Table 4: Exemplary rheological studies of mucus from different species and organs.

Ref.	Species	Organ	Macro η [Pas]	G' [Pa]	G'' [Pa]
[11]	Human	Lung	10 at 1 rad/s	10 at 1 rad/s	4 at 1 rad/s
[14]	Human	Lung (CF)	70 at 0.1 s^{-1}	-	-
[18]	Human	Cervical	1 at 1 s^{-1}	-	-
[13]	Human	Lung (CF)	-	95 at 1 rad/s	22 at 1 rad/s
[13]	Human	Lung (COPD)	-	3 at 1 rad/s	1 at 1 rad/s
[3]	Human	Cervical	40 at 1 rad/s	-	-
[3]	Human	Lung	5 at 1 rad/s	-	-
[3]	Human	Lung (Bronchitis)	10 at 1 rad/s	-	-
[3]	Human	Lung (CF)	20 at 1 rad/s	7 at 1 rad/s	3 at 1 rad/s
[3]	Dog	Subglottis	1-20 at 1 rad/s	5-63 at 1 rad/s	1-20 at 1 rad/s
[3]	Pig	Intestinal	0.1-5 at 1 rad/s	0.2-10 at 1 rad/s	0.1-6 at 1 rad/s
[3]	Rat	Trachea	0.01-3 at 10 rad/s	2-8 at 10 rad/s	0.2-6 at 10 rad/s
[3]	Horse	Trachea	0.6-1 at 10 rad/s	18-34 at 10 rad/s	6-12 at 10 rad/s
[3]	Rabbit	Trachea	35-130 at 1 rad/s	-	-
[3]	Ferret	Trachea	12-110 at 1 rad/s	-	-
[69]	Pig	Trachea	-	3 at 1 s^{-1}	2 at 1 s^{-1}
[70]	Pig	Gastric	10-100 at 1 rad/s	20-200 at 1 rad/s	3-30 at 1 rad/s

The rheological properties, in particular the macrorheological parameters G' and G'' , are important to calculate the deformation of the mucin fibers due to the particle impact. Therefore, we need to simulate the fluid dynamics in the lung and compute the resulting kinetic energy of inhaled particles. After comparing this energy with the necessary deformation energy to expand the mucus pores -after a deformation of the mucin fibers- we will qualitatively determine the possibility of a particle to penetrate one mucus pore.

5.2 Macro- and microrheological properties of native porcine respiratory and intestinal mucus

Parts of this chapter have been published in Bokkasam H., M. Ernst, M. Günther, C. Wagner, U. F. Schäfer, and C.-M. Lehr (2016). Different macro- and micro-rheological properties of native porcine respiratory and intestinal mucus. International Journal of Pharmaceutics 510(1):1-12.

5.2.1 Materials & Methods

Mucus was collected from pigs used for experimental surgery studies, which had to be killed afterwards. Therefore, no animals had to suffer or to be sacrificed to obtain this biological material, in line with the 3R-concept. Care was taken that the preceding surgery experiments had no influence on the organs relevant to our studies. Mucus was collected within 30 minutes after euthanasia. The trachea was cut into halves [68] and mucus was obtained by carefully scratching. Intestinal mucus was harvested from the ileum and duodenum of the same animal after a short rinse with water [67].

For comparison, HEC gels of 1 and 2 % (w/v) were prepared using NatrosolHHX 250 (Hercules Aqualon, Düsseldorf, Germany).

Macrorheological studies of storage and loss module (G' and G'') were performed with a 25 mm plate-plate geometry in a MARS II rheometer (ThermoHaake, Karlsruhe, Germany) as used in previous studies [66,67]. The volume of the mucus samples, put in the rheometer, was between 20 and 30 μL , resulting in a gap distance between 40 and 60 μm . Measurements at 1 Hz were used for comparison.

Passive and active microbead rheology with optical tweezers provides a promising laser-based method for investigating the Brownian motion and induced movement of microparticles in a laser trap [8,71]. A Tweez250i system from Aresis (Ljubljana, Slovenia) was utilized. Melamine resin beads of 2.86 and 6 μm diameter were purchased from Microparticles GmbH (Berlin, Germany). Sample preparation was performed for both mucus and HEC gels as described in previous experimental studies [8].

Passive microbead rheology was studied by recording the restricted Brownian motion of microparticles at a frame rate of approx. 670 fps. Based on the experimental conditions,

mainly the viscosity of the interstitial fluid in the mucus pores is measured by this method. For more details see supplementary material.

Active microbead rheology was performed by applying a sine wave (Frequency = 0.1 Hz and Amplitude = 1 μm) to microparticles. The amplitude of particle movement (output displacement response) to an input displacement of 1 μm is measured from the displacement of the particle over time. As the amplitude of this active particle movement is at least 10times larger than the movement in passive microbead rheology measurements, additional macrorheological effects cannot be excluded.

OriginPro 2015 (Northampton, USA) and One-way ANOVA were used for Box-and-whisker plots as well as for statistical calculations. Moreover the Scheffé's method as post hoc analysis was applied. The level of statistical significance is indicated by the corresponding p-value.

5.2.2 Results & Discussion

Viscoelastic properties of porcine mucus from ileum, duodenum and trachea are depicted in Fig. 41. One-way ANOVA reveals statistically significant ($p < 0.05$) differences between intestinal and respiratory mucus, but there is no significant difference between mucus from ileum and duodenum. In Figure 40 the frequency sweep of the rheometric measurements from Figure 41 is shown. We used a frequency of 1 Hz (6.3 rad/s) to compare the results from the rheometry with them of the active and passive microbead rheology measurements with optical tweezer. However, the macrorheological elastic (red solid lines) and viscous (blue dashed lines) modulus strongly depends on the frequency of the rheometer.

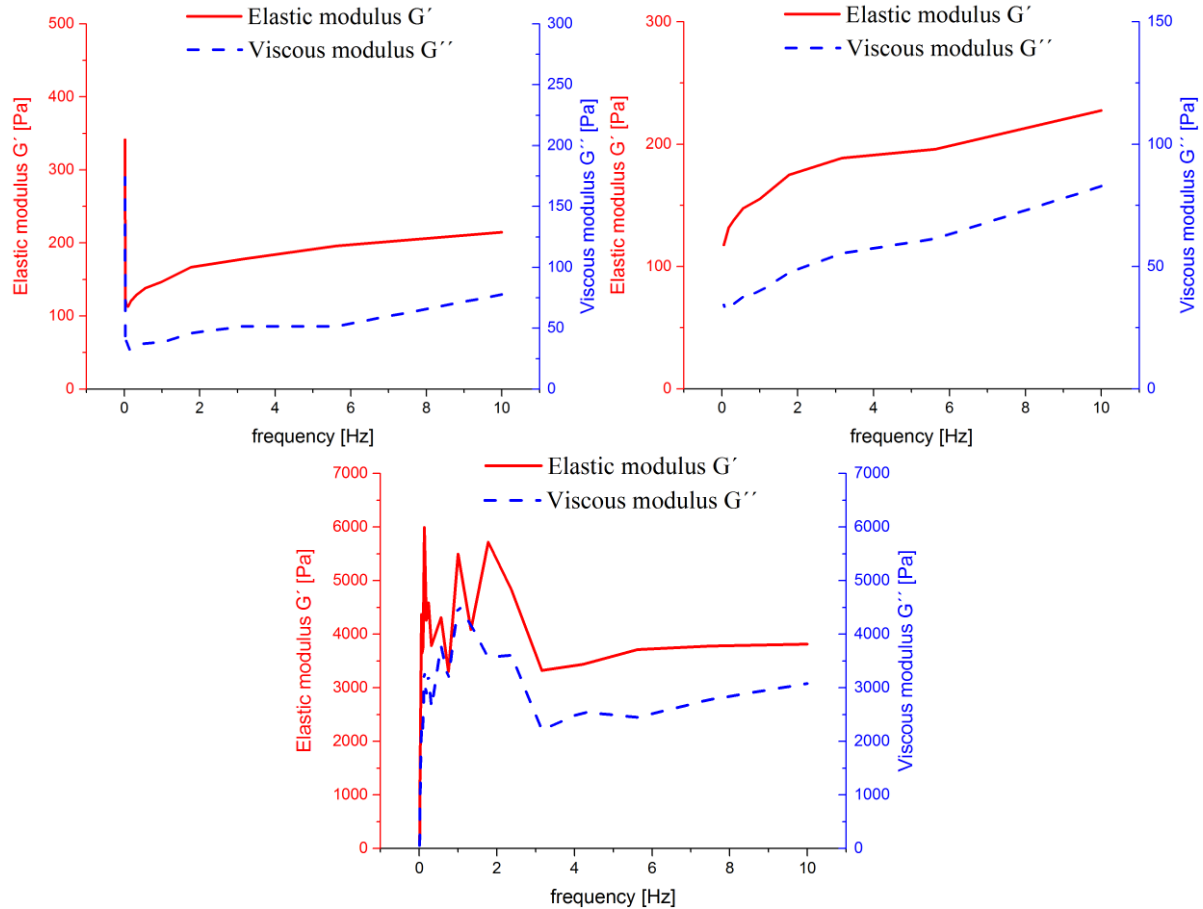


Figure 40: Macrorheological elastic (G' , red solid lines) and viscous moduli (G'' , blue dashed lines) of mucus preparations at various rheometer frequency.

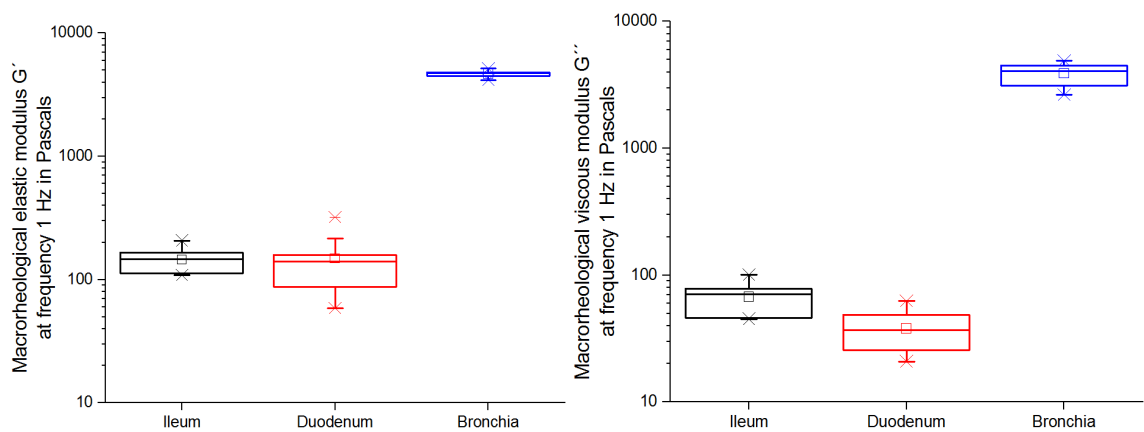


Figure 41: Macrorheological A: elastic (G') and B: viscous moduli (G'') of mucus preparations at 1 Hz. At least 20 measurements were performed for each region.

Fig. 42 shows the results of the elastic storage modulus G' measurements from passive microbead rheological studies by means of optical tweezers for 2.86 and 6 μm particles (for more details see supplementary material). In contrast to the macrorheological investigations, no statistically significant ($p > 0.05$) differences are found between intestinal and respiratory mucus for both 2.86 and 6 μm beads. It can be concluded that there are no microrheological differences between intestinal and respiratory mucus obtained from the same mammalian species (pig).

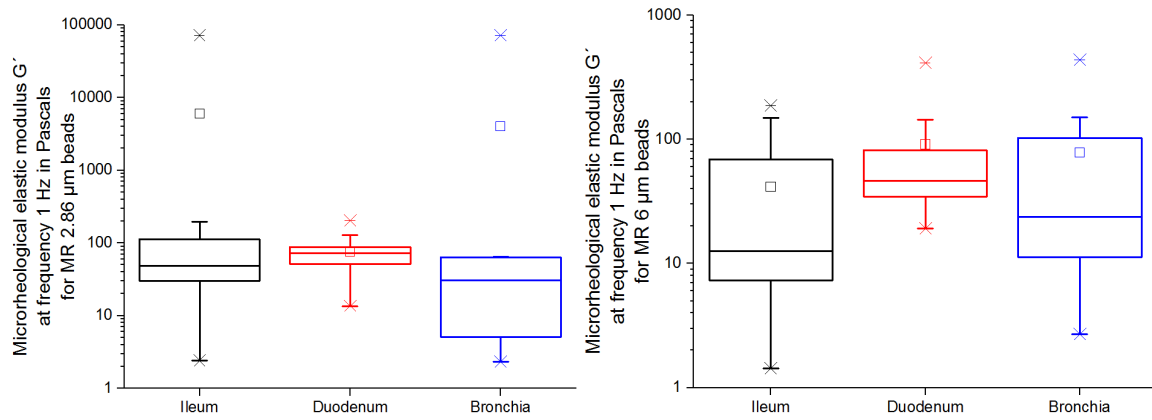


Figure 42: Microrheological elastic moduli (G') with optical tweezers for (A) 2.86 μm and (B) 6 μm beads. At least 20 measurements were performed for each region.

Fig. 43 reveals that microparticle movement in HEC gels (A, B; red dashed line) has similar pattern to particle movement in water (black straight line) but not in either respiratory or intestinal (ileal) mucus (C, D; red dashed line). Here, 6 μm particle movement is shown as an instance of the motion of (micro)particles in complex structures and the same holds true for 2.86 μm particles. These findings correlate with previous studies on equine respiratory tract mucus preparations with optical tweezers [8].

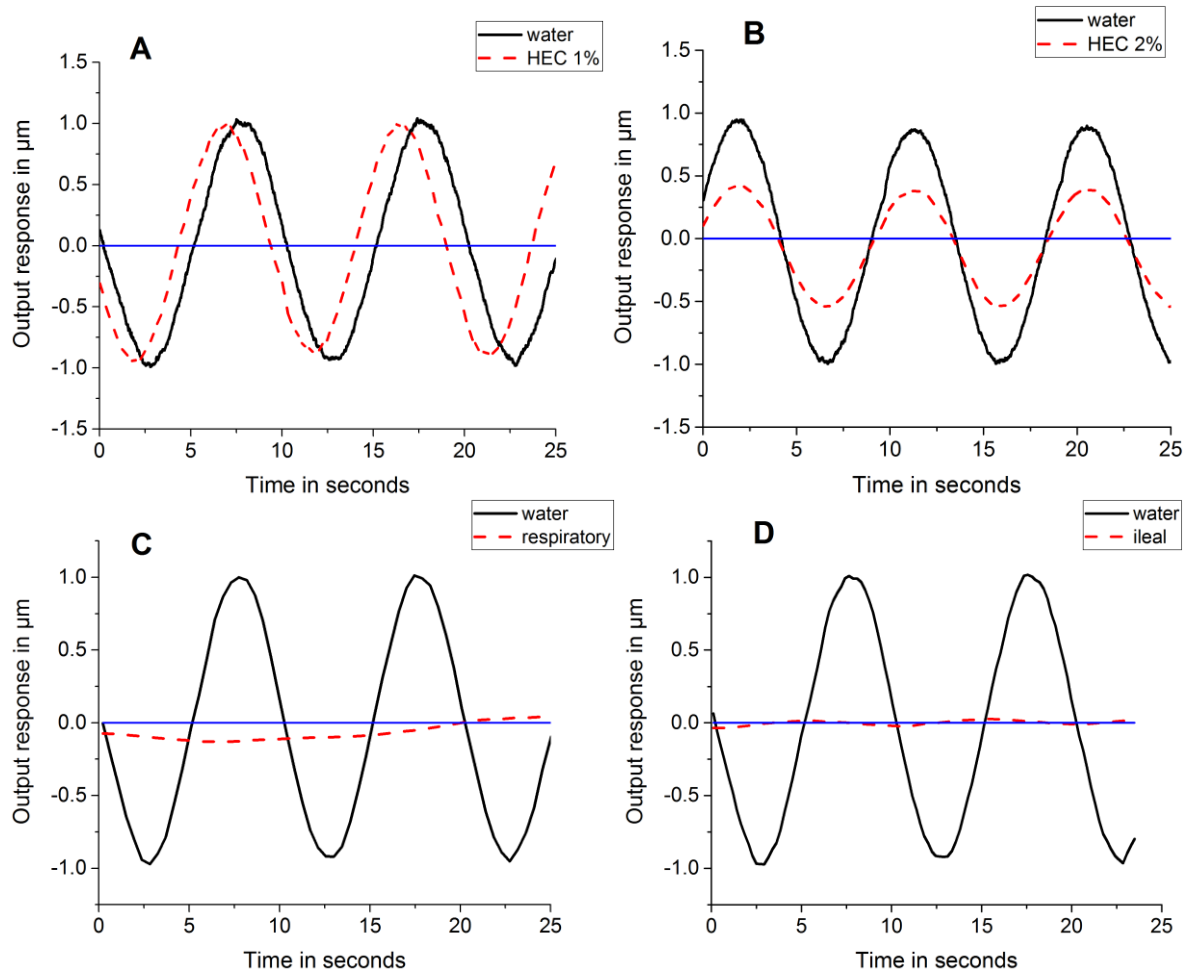


Figure 43: Optical trap displacement in μm of a $6 \mu\text{m}$ particle in (A) HEC-1%, (B) HEC-2%, (C) respiratory, and (D) ileal mucus (red dashed lines). Displacement of particles in water is shown as a black solid line in each graph for comparison. At least 20 measurements were performed for each region.

Active microbead rheology (output displacement response) measures the force of the beads against single mucin fibers and the resistance to the bead movement. One-Way ANOVA reveals statistically significant differences ($p < 0.05$) between such data for pulmonary and intestinal mucus, whereas no statistically significant differences were found between ileal and duodenal mucus (Fig. 44). The higher output displacement response for 2.86 and $6 \mu\text{m}$ beads, as observed for pulmonary mucus in comparison to intestinal mucus, can be explained by either a lower rigidity of pulmonary mucin fibers or a larger mesh size for the pulmonary mucus network. This finding points to differences in the mucus barrier function between the investigated organs, i.e. intestine and lung, and route of administration.

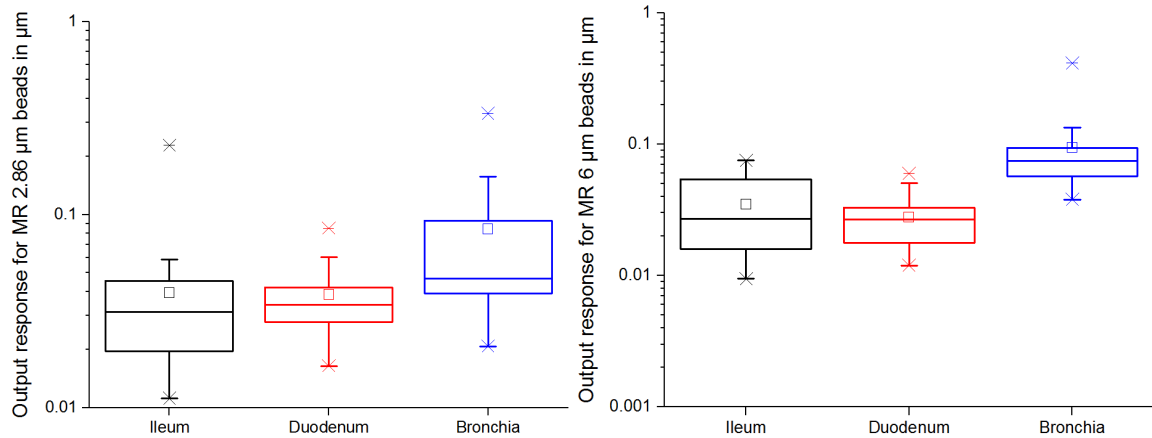


Figure 44: Output displacement response in μm of mucus preparations for (A) 2.86 μm and (B) 6 μm beads. At least 20 measurements were performed for each region.

In Table 5 the measured G' and G'' from our experiments (*) are compared with the corresponding data from other studies, as shown in Table 4. Only the best fitting data from these studies are presented in comparison with our results.

Table 5: Comparison of the experimentally determined rheology parameters (see columns marked with asterisks, red labeled results from passive microbead rheology methods) with the results from previous studies (see Table 4).

Ref.	Species	Organ	Macro η [Pas]	G' [Pa]	G'' [Pa]	G' [Pa] *
[11]	Human	Lung	10 at 1 rad/s	10 at 1 rad/s	4 at 1 rad/s	12
[13]	Human	Lung (CF)	-	95 at 1 rad/s	22 at 1 rad/s	80
[3]	Dog	Subglottis	1-20 at 1 rad/s	5-63 at 1 rad/s	1-20 at 1 rad/s	12 / 24 / 30 / 46 / 50 / 60
[3]	Pig	Intestinal	0.1-5 at 1 rad/s	0.2-10 at 1 rad/s	0.1-6 at 1 rad/s	12
[3]	Horse	Trachea	0.6-1 at 10 rad/s	18-34 at 10 rad/s	6-12 at 10 rad/s	12 / 24 / 30
[70]	Pig	Gastric	10-100 at 1 rad/s	20-200 at 1 rad/s	3-30 at 1 rad/s	24 / 30 / 46 / 50 / 60 / 80 / 150

Here, the red labeled values are measured by passive microbead rheology methods (see Fig. 42), whereas the remaining values are from conventional plate rheometry measurements (see Fig. 41). Surprisingly, the measured G' and G'' of bronchial mucus in the rheometer are extremely high (several thousand Pascal), which may be due to a progressed drying of our

mucus samples or maybe the scratching out of the mucus from the lung epithelial was not carefully enough to avoid some residues of the epithelial in the samples. However, except these extremely high G-values from experiments with bronchial mucus, the measured G'-values from the experiments, which are shown in Fig. 41 (rheometry: $G' = 150$ Pa) and Fig. 42 (optical tweezer: $G' = 12-80$ Pa), are comparable to the results from other studies. Only the G'' -values are significantly higher (40-70 Pa) in our experiments, compared to the results from other studies in Table 4.

5.3 Calculation of the necessary deformation energy to expand the mucus pores

5.3.1 Computation of the deflection and deformation of mucin fibers

To investigate the possibility for inhaled particles to penetrate the mucus layer, the elastic deformation of mucin fibers will be calculated in this section. We assume linear elastic fibers to calculate this deformation by numerically computing the necessary energy to achieve a prescribed deflection, respectively pore expansion, solving the bending equation.

The aim of these calculations is to compute the expansion of the mucus pore, which is modeled as the void between two fibers. Due to the deflection of the fiber, e.g. in the y-direction, there is also a deformation in the x-direction. This effect leads to a symmetrically expansion of the mucus pore, if we assume a particle impact exactly in the center of the pore and also a consistent fiber length, in case of a deflection vertically to the fiber position (see Fig. 45). Finally, we qualitatively determine the possibility of a 200nm-sized particle to move through a 100nm-sized pore.

The order to determine the probability of a particle to pass the mucus pore is first: to compute the needed energy to expand the mucus pore in a way, that allows the particle to completely pass the pore; and: to compare the kinetic energy from the CFD-simulations in the next section with this deformation energy. Additionally, we will also compare the necessary deformation energy with the Brownian kinetic energy of the same particle.

In this section, we first calculate the deflection f of the mucin fibers by solving the general deflection equation, given as follows [72]:

$$f = \frac{1}{E I_M} \sum M(x) s \Delta l \quad (23)$$

with the Young's modulus E , the second moment of area I_M (the product $E \cdot I_M$ is the bending stiffness), the sum of all force moments $\sum M(x)$, the curved section s , and Δl as the distance between the center of s (during deflection) and the end of the mucin fiber.

The second moment of area I_M is defined as follows [72]:

$$I_M(x) = \frac{bh^3}{12} \quad \text{and} \quad I_M(y) = \frac{b^3h}{12} \quad (24)$$

with the width b and the height h of the mucin fiber. To simplify, we assume the fibers to be as wide as high ($h = b$).

Due to the difficulties in determining the curved section s of a deformed object and therefore in calculating the deflection analytically, consequently, we will compute the deflection numerically, using the Finite Element Method.

As we assume a linear elastic material, the Hook's law is valid to calculate the elastic strain ε_{el} , as given by:

$$\varepsilon_{el} = \frac{\sigma_{el}}{E} \quad (25)$$

with the assumed elastic stress σ_{el} . The elastic strain is then computed in the structural mechanics module of Comsol Multiphysics by using the deformation w and numerically solving the following equation:

$$\begin{aligned} \varepsilon_{el} &= \varepsilon - \varepsilon_{inel} \quad \text{with} \\ \varepsilon &= \frac{1}{2} [(\nabla w)^T + \nabla w] \end{aligned} \quad (26)$$

with the inelastic part of the strain ε_{inel} and the total strain ε .

Here, a mesh with homogeneous triangular elements with a size between minimum 0.1 and maximum 1 nm is implemented to discretize the fiber geometry. To solve the differential equations, a parallel sparse direct stationary solver is used.

For the sake of completeness, we also show, how to calculate the deflection by using the theorem of Pythagoras and the analytical solution of the deflection f , assuming the fibers to be linear elastic, as given as follows [72]:

$$\begin{aligned}
 f &= x_0 \frac{Fl^2}{2EI_M} \quad \text{if the fiber is fixed only at one end} \\
 f &= x_0 \frac{Fl^2}{16EI_M} \quad \text{if the fiber is fixed at both ends; with} \\
 x_0 &= \frac{2}{3}l \quad \text{if the fiber is fixed only at one end} \\
 x_0 &= \frac{1}{3}l \quad \text{if the fiber is fixed at both ends.}
 \end{aligned} \tag{27}$$

with the assumed impact force F of the particle and the length of the fiber l .

The expansion of the mucus pore is calculated by using the deflection of the mucin fiber f and the length l of the fiber, which is assumed to stay constant in case of a deflection vertically to the fiber position (see Fig. 45). Thus, the expansion of the pore p_{exp} is given as:

$$p_{\text{exp}} = l - \sqrt{l^2 - f^2} \tag{28}$$

Fig. 45 shows the geometrical model of the mucus pore as a gap between two mucin fibers, which are modeled as two thin beams in this work. Additionally, this Figure summarizes the mentioned assumptions to calculate the expansion of the mucus pore (deformation in blue), as well as the extension of the mucin fiber (deflection in red). It also shows the assumed boundary conditions of the numerical model.

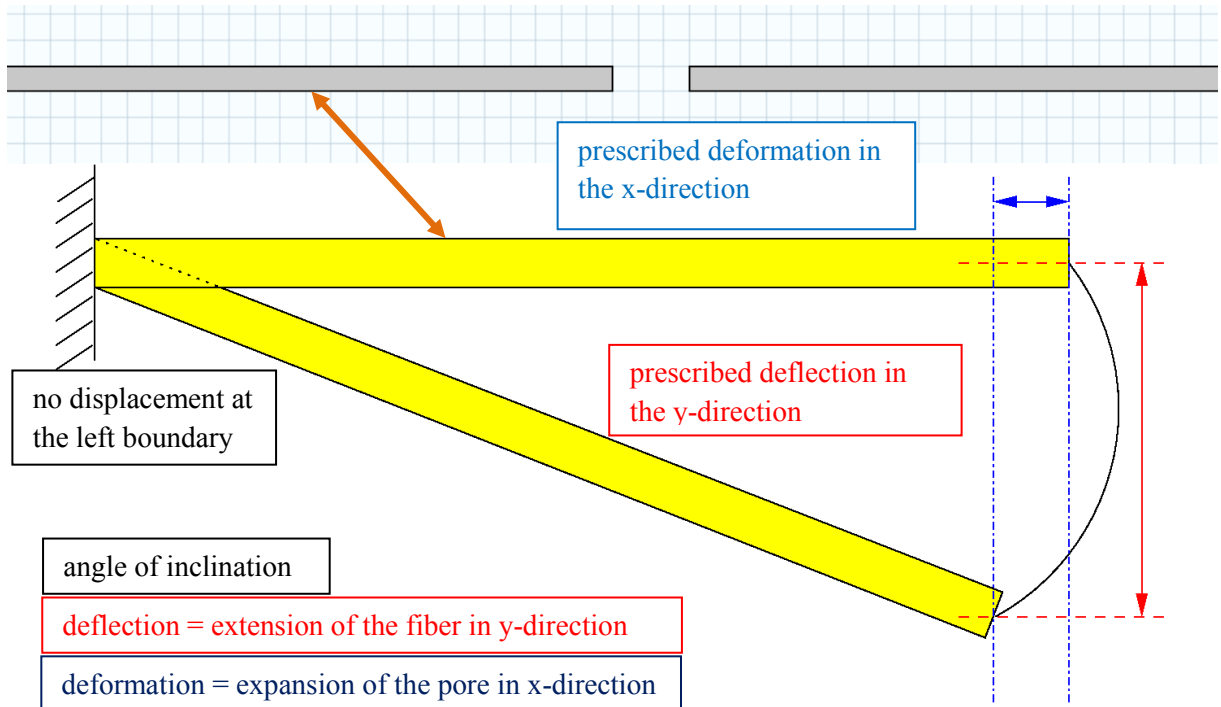


Figure 45: Schematic view of two mucin fibers and one void between these fibers, which is defined to be the mucus pore (upper Figure). The mucus pore has to be expanded to achieve a penetration of a larger particle. Schematic view of the mechanical deformation, leading to an expansion of the mucus pore (blue dash-dotted lines) due to the deflection of the mucin fiber (red dashed lines), and the angle of inclination between the initial fiber position and the position after mechanical load.

As mentioned, after the deflection of the fibers, the size of the void, respectively the mucus pore d_p , should increase to let the particle pass through.

So, we presented two ways to calculate the deflection of a mucin fiber, which are the numerical simulation with the deflection w and the analytical solution with the resulting deflection f . Both values can be achieved by two different methods: We could assume an impact force F of an inhaled particle or we could prescribe the deflection to yield a necessary pore expansion for the particle to pass through. The former method is an iterative process, where we have to find the minimum kinetic energy of a particle to achieve the necessary force F to deform the fiber, resulting in a pore expansion. In the latter method we prescribe the pore expansion to be $p_{\text{exp}} = 2R - d_p$, with the hydrodynamic radius R of the particle. We then compute the necessary deformation energy to achieve the prescribed pore expansion.

We assume a necessary expansion of the pore $p_{\text{exp}} = 100 \text{ nm}$ ($R = 100 \text{ nm}$, $d_p = 100 \text{ nm}$), a Young's modulus of 100 Pa , and a mucin fiber density of 1000 kg/m^3 .

After applying the theorem of Pythagoras $(\sqrt{200^2 - (200-50)^2})$, we calculate a necessary deflection in the y-direction -with a given deformation of one fiber in the x-direction ($p_{exp}/2 = 50 \text{ nm}$) and the fiber length ($l = 200 \text{ nm}$)- of approx. 133 nm. We compute the von-Mises equivalent stress in [N/m^2], which is defined as the stress, needed to change the shape of an object. Commonly, the von-Mises stress is used to compare different stress conditions and it is defined as follows [74]:

$$\sigma_{vM} = \sqrt{\sigma_x^2 + \sigma_y^2 + \sigma_z^2 - \sigma_x\sigma_y - \sigma_x\sigma_z - \sigma_y\sigma_z + 3(\tau_{xy}^2 + \tau_{xz}^2 + \tau_{yz}^2)} \quad (29)$$

with the x-, y-, and z-component of the stress σ and the torsion τ in the xy-, xz-, and yz-plane.

After multiplying the von-Mises stress with the volume of the considered object -here the mucin fiber ($2.0E-23 \text{ m}^3$)-, we achieve the necessary deformation energy in [J]. This energy is needed to deform the mucin fiber in a way that allows the impacted particle to pass the expanded pore.

We calculate the deformation energy, if we prescribe the deformation in the negative x-direction to be 50 nm ($p_{exp}/2$). The Figures 46 and 47 show the prescribed deformation of the edge inside the pore in negative x-direction and the resulting von-Mises stress, respectively.

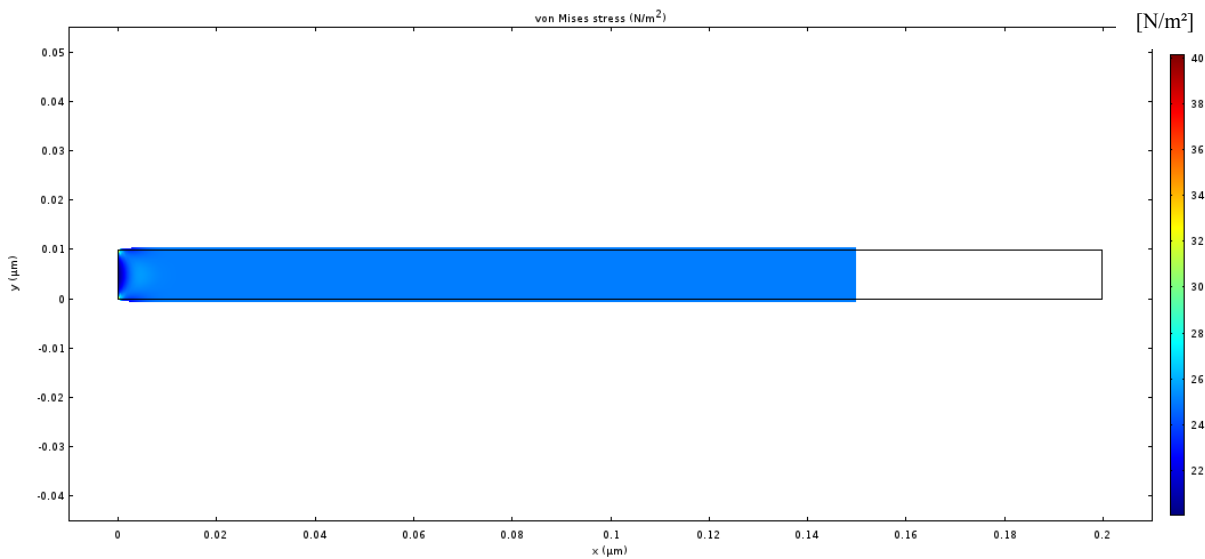


Figure 46: Von-Mises stress profile of one fiber after applying a prescribed deformation of -50 nm of the right edge in the negative x-direction.

To consider the conservation of the fiber volume, the width b , respectively the height h , of the fiber in Figure 46 must increase.

In Fig. 47, the von-Mises stress is shown at the intersection of the fiber at $y = 0.005 \mu\text{m}$.

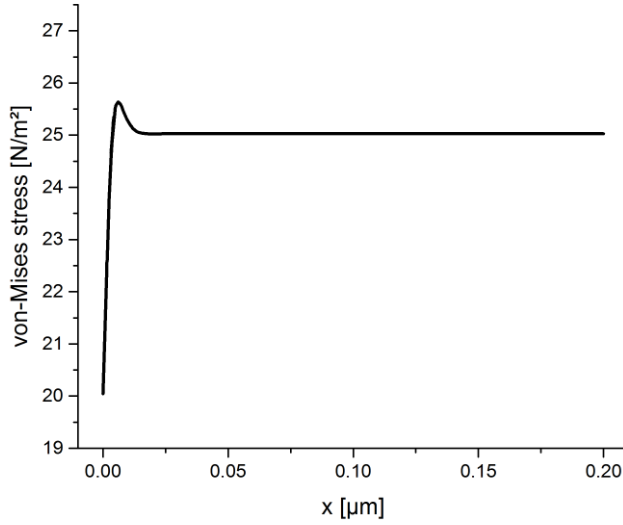


Figure 47: Von-Mises stress at the intersection at $y = 0.005 \mu\text{m}$ in x-direction of one fiber after applying a prescribed deformation of -50 nm of the right edge in the negative x-direction.

In the Figures 48 and 49 the displacement of the middle point of the edge inside the pore is prescribed in the negative y-direction (133 nm), and the resulting von-Mises stress is shown.

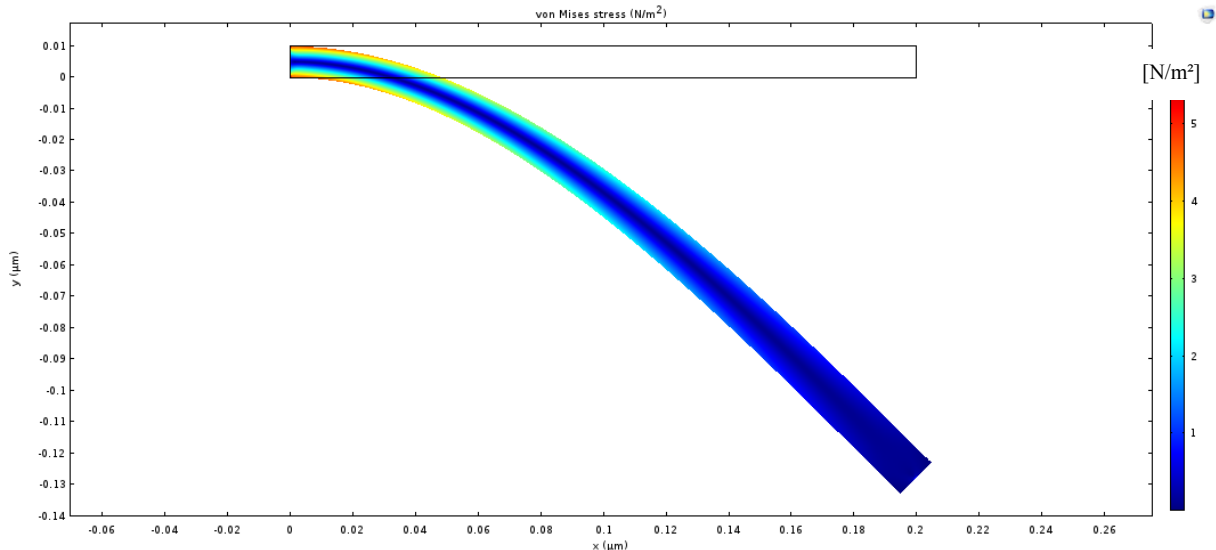


Figure 48: Von-Mises stress profile of one fiber after applying a prescribed deflection of approx. -133 nm of the middle point ($y = 0.005 \mu\text{m}$) of the right edge in the negative y-direction.

To consider the conservation of the fiber volume, the width b , respectively the height h , of the fiber in Figure 48 must decrease. However, the deformation in Fig. 48 is not shown in a proper way, due to the assumption of a constant geometric ratio between the width b , the height h , and the length l of the fiber (see Fig. 45).

In Fig. 49, again the von-Mises stress is shown at the intersection of the fiber at $y = 0.005 \mu\text{m}$.

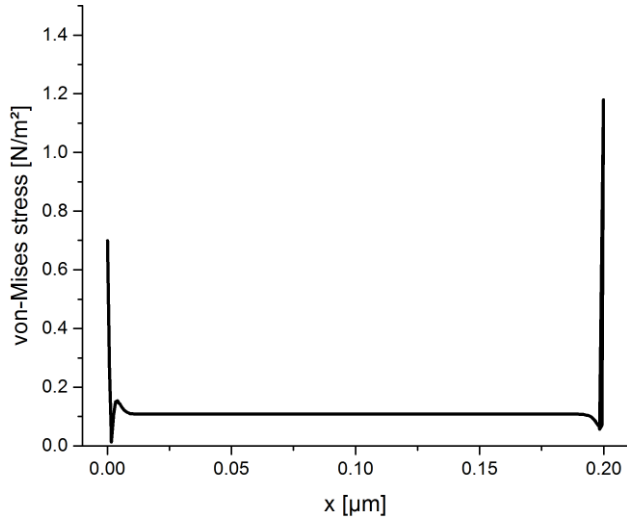


Figure 49: Von-Mises stress at the intersection at $y = 0.005 \mu\text{m}$ in x-direction of one fiber after applying a prescribed deflection of approx. -133 nm of the middle point ($y = 0.005 \mu\text{m}$) of the right edge in the negative y-direction.

All computed values are determined in Joule per cubic meters ($\text{N}/\text{m}^2 = \text{J}/\text{m}^3$), which means the energy in Joule, needed to deform an object with a volume of 1 m^3 . Consequently, to determine the necessary deformation energy of the fiber, we have to multiply the von-Mises stress by the volume of the fiber ($2.0\text{E}-23 \text{ m}^3$). This calculation results in a deformation energy of $2.2\text{E}-24 \text{ J}$ in case of a prescribed deflection in the y-direction (see Figures 48 and 49), and of $5.0\text{E}-22 \text{ J}$ in case of a prescribed deformation in the x-direction (see Figures 46 and 47). As expected, the necessary deformation energy is lower in case of a vertically deflection of the mucin fibers, e.g. by an impaction of an inhaled particle.

In addition, we have to consider the fact that, in case of a doubling of the length of the fiber, the moment M at the edge of the fiber will double, too. However, if the width or the height of the fiber is doubled, the second moment of area I_M will be 8fold higher than before, respectively in case of $h=b$, I_M will be 16fold higher. So, if other geometries and length scales of the fiber will be investigated in future, one has to consider this fact, which will yield in totally different -probably higher- necessary deformation energies.

5.3.2 Brownian diffusive energy and comparison with the necessary deformation energy

The necessary deformation energy, which is computed by the numerical simulations of the deflection of a mucin fiber will be compared with the kinetic energy from convective flow of an aerosol (see Table 9 and Table 10) and also with the kinetic energy of Brownian motion, whereat the latter is given by:

$$E_{Brown} = \frac{3}{2} k_B T \quad (30)$$

Thus, we will check the possibility of a particle to penetrate a mucus pore by either impaction due to the air flow (kinetic energy from CFD-simulations) or by Brownian motion. For a given Boltzmann constant of 1.38E-23 J/K and an assumed absolute temperature of 310.15 K, we yield a Brownian kinetic energy of 6.24E-21 J. So, this energy would be sufficiently high enough to achieve a pore expansion, allowing the particle to pass through this pore, just by Brownian diffusion (with the assumed fiber dimensions and parameters, as described in the prior section).

The Brownian kinetic energy as shown in Eq. 30 contains only the Einstein-component -the thermal energy- of the Stokes-Einstein-relation. If we consider also the Stokes friction force, which is present in case of particle diffusion, the kinetic energy of the Brownian motion will be reduced. As shown in Eq. 12, the Stokes friction force depends on the viscosity of the fluid, the particle size, and the relative velocity of the particle in a flowing fluid. However, the Brownian kinetic energy is higher for smaller particles and in fluids with a lower viscosity. So, as we assume the fluid viscosity to be similar to that of water, extremely small particles in the nm-range yield in a significantly higher Brownian diffusive energy, compared to microparticles. Due to the fact that, the thermal energy of a Brownian particle is at least 10fold higher than the calculated necessary deformation energy, the effects of the Stokes friction force on the Brownian kinetic energy is vanishing.

5.4 Conclusions

Macrorheological investigations (plate–plate viscosimetry) on mucus obtained from the respiratory (trachea) and intestinal tract (ileum and duodenum) of the same species (pig) revealed significant differences in viscoelastic properties for these two organs. Passive microbead rheological measurements (particle tracking of Brownian dynamics), taking place only in the interstitial fluid of the mucus pores, are not able to detect these differences. However, active microbead rheology measurements (induced movement by optical tweezers) again revealed significant differences between respiratory and intestinal mucus, pointing to biomechanical differences in the constituting mucin fibers or structural differences in the resulting hydrogel networks.

We computed the necessary deformation energy of a mucin fiber to achieve a penetration of a particle through an expanded mucus pore. The possibility of such a particle to pass this pore will be qualitatively described in the following section in case of a convective air flow. However, we showed that the Brownian diffusive energy of a particle should be high enough to achieve a vertical deflection of the mucin fiber and even high enough to achieve a horizontal deformation of the fiber, both resulting in an expansion of the pore. The latter case was shown to need a significantly higher energy to yield the required pore expansion, allowing the particle to pass the pore.

6 Computational Fluid Dynamics (CFD) Simulations of the Air Flow in the Human Lung

6.1 Introduction

6.1.1 Structure of the human lung

The human lungs are responsible for the gas exchange between the atmospheric air and the blood. The right lung, pulmo dexter, is larger and consists of three lobes, the superior, the middle and the inferior lobe. The left lung, pulmo sinister, consists only of a superior and an inferior lobe, leaving space for the heart in the chest cavity. Breathing air passes the trachea and flows into the lobes that contain a large system of air-carrying tubes, the respiratory tree [75].

However, in this work only the trachea and the upper part of the respiratory tree, the main bronchi, are considered. The left and right main bronchus, bronchus principalis sinister and bronchus principalis dexter, respectively, are branching off from the trachea. The right bronchus is wider in radius, shorter until it branches out and steeper in the angle, which leads to an asymmetry of the lungs and to a higher accumulation of foreign substances in the right bronchus. The left bronchus is less steep than the right bronchus, again to leave space for the heart cavity. The angle γ_B between the two main bronchi is between 55 and 70° [75,76]. Fig. 50 shows a schematic view of the human lung [77].

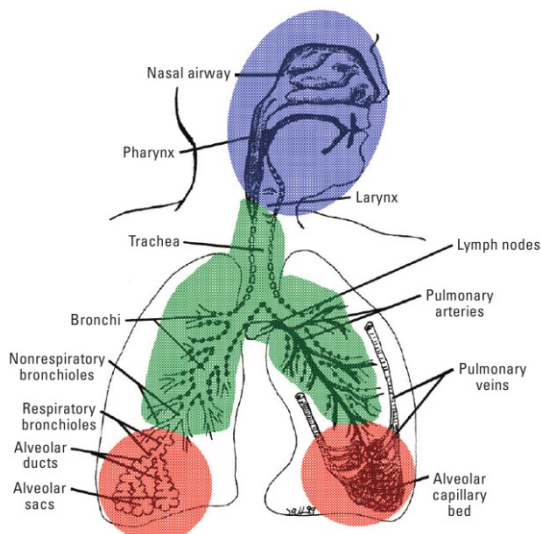


Figure 50: Structure of the human lung with the oral and nasal cavity (blue region), the upper respiratory tract (green region), and the lower respiratory tract (red region), Oberdörster et al. [77].

6.1.2 Development of lung models

Aim of the simulation of the air flow in the upper lung is to determine the velocity profile in different regions of the upper airways and to compute the kinetic energy of inhaled particles, impacting on the mucus layer in these regions.

Air is used as continuous fluid to simulate the flow dynamics in the upper airways, modeled as a simplified symmetrally geometry and as a more realistic non-symmetrally geometry (see Fig. 51 and Fig. 52, respectively). In both Figures, on the right side, the velocity profile is shown for an inlet velocity of 1 m/s.

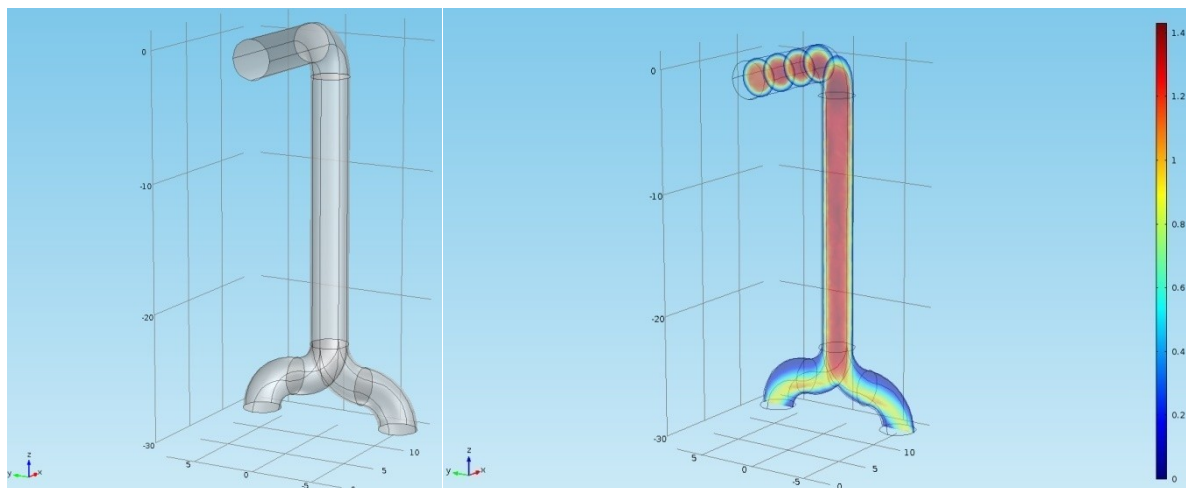


Figure 51: Simplified symmetrical model of the human lung with the velocity profile on the right side (inlet velocity is 1 m/s).

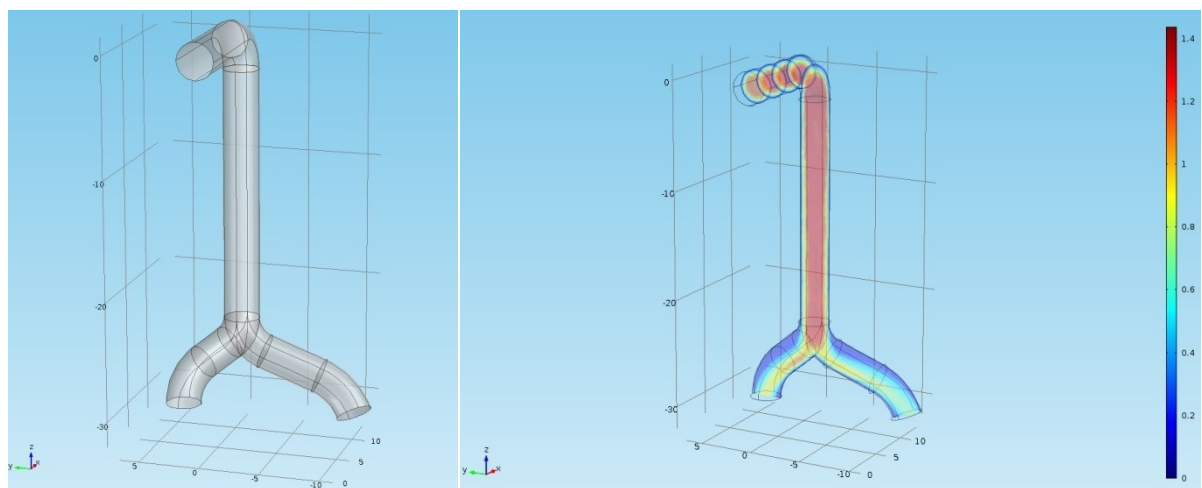


Figure 52: Simplified asymmetrical model of the human lung with the velocity profile on the right side (inlet velocity is 1 m/s).

For the CFD-simulations, in a first geometrical model, the larynx and the trachea are interpreted as a pipe with a diameter of 1.5 cm and with a 90°-turn after 9 cm. After additional 21 cm, the main bronchi, which are also modeled as pipes with a diameter of each 1.5 cm, are branching off in a 90°-turn, followed by a second 90°-turn (see Fig. 51). To improve this model of the upper airways, we also introduce a more realistic non-symmetrically model (see Fig. 52) with a steeper angle for the right bronchi, compared to the left bronchi, resulting in an asymmetry.

To improve our model, we also introduce a further geometrical lung model, which directly considers the mucus layer, as steric hindrances within the trachea (see Fig. 53).

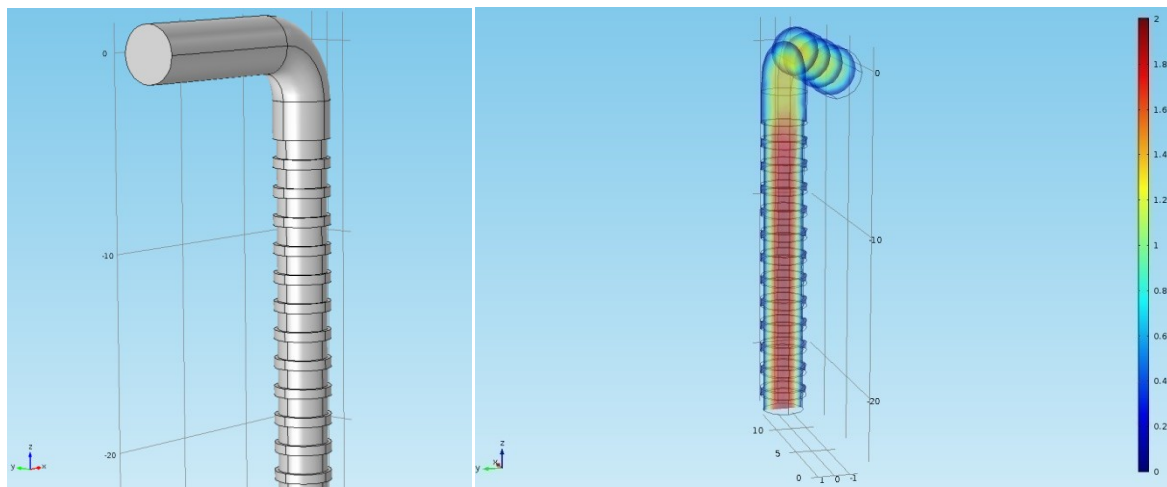


Figure 53: Realistic model of the human trachea with steric hindrances, representing the mucus layer, with the velocity profile on the right side (inlet velocity is 1 m/s).

In general, flow rates between 5 and 15 l min⁻¹ are assumed to simulate the inhalation of an aerosol, which leads to inlet velocities between 0.5 and 1 m s⁻¹, assuming a tube diameter of 1.5 cm. In the FEM-model, a no-slip boundary condition is used, which means that the fluid velocity u is zero at the boundary.

There exist two essential parameters for the flow of aerosols and particulate matter in a fluid, which are the Reynolds and the Stokes number. The former describes the fluid flow regime, whereas the latter describes the drag and the inertia of a particle, which is transported within a fluid by a convective flow. The Stokes number is defined as [75,78,79]:

$$St = \frac{\rho_p (2R)^2 u}{18\mu_f D_L} \quad (31)$$

with the particle density ρ_p , the fluid velocity u , the characteristic length, respectively the characteristic dimension, D_L , and the kinematic viscosity μ_f of the fluid.

The typical mean ventilation rate for a sitting and awake adult man is 150 mL s^{-1} [75], which results in a flow velocity of 0.85 m s^{-1} , assuming an inner diameter of $D_L = 1.5 \text{ cm}$, as referred to our lung model. This leads to a Reynolds number of 750, assuming a fluid density of 1.0 kg m^{-3} and a dynamic viscosity of the air of $17 \mu\text{Pas}$. The Reynolds number describes the regime of a fluid flow (turbulent or laminar flow) and is calculated as given by [75]:

$$\text{Re} = \frac{\rho_f u D_L}{\eta} = \frac{u D_L}{\mu_f} \quad (32)$$

with the fluid density ρ_f , the kinematic viscosity μ_f , and the dynamic viscosity η .

Due to the low Reynolds number of 750, we assume a laminar flow of the air in the upper lung. The essential equation to simulate an incompressible laminar flow is the Navier-Stokes-equation, given as follows [23]:

$$\rho_f (u \nabla) u = \nabla \left[-p_l I + \mu_f (\nabla u + (\nabla u)^T) \right] + F_{\text{ext}} \quad (33)$$

with the pressure p_l inside the lung. Here, no external force F_{ext} are considered.

The discretization of the geometry is done with homogeneous triangular mesh elements with a size between minimum 0.1 and maximum 2 cm and additional homogeneous rectangular mesh elements at the boundary to achieve a high accuracy of the numerical solution in the boundary layer. To solve the differential equation system, a parallel sparse direct stationary solver for the laminar flow is used.

During the inhalation, an absolute pressure of 0.4 kPa at the outlet of the main bronchi is assumed [80]. Due to an increase of the lung volume during the inspiration, the pressure is reduced to a slight vacuum, compared to the atmospheric pressure outside of the lung. So, in our model of the respiratory tract, we define the inlet velocity as shown in Table 8, and the outlet pressure to be 0.4 kPa.

As we assume an overdamped movement of the particles in the air stream, external forces, such as the drag force or the gravity are neglected, so the Stokes-number is no longer needed.

However, in our study we assume the particle velocity v to be identically with the fluid velocity u and to be stationary, which means v is constant over the time. Consequently, we can calculate the kinetic energy of the particles as given by:

$$E_{kin} = \frac{1}{2} m_p v^2 \quad (34)$$

with v and m_p as the particle velocity and mass, respectively. To calculate the kinetic energy of the inhaled particles, we just need the simulated fluid velocity u ($= v$) and the particle mass m_p . We show simulated values of the kinetic energy in Table 8 and we compare them with the necessary deformation energy and the Brownian diffusive energy in the Tables 9 and 10.

As mentioned before in Eq. 30 (definition of the Brownian diffusive energy), also here we did neglect the Stokes friction force, due to the assumption of an overdamped movement. Additionally, if we assume a convective flow of microparticles in air and a Brownian motion of nanosized particles (nanoparticles are released from microparticles) in a fluid with a viscosity similar to that of water, the Stokes friction force is equally for both cases and can be neglected.

6.1.3 Particle deposition processes

There are four main processes, which are relevant to the deposition of particulate matter in the lung: the impaction due to the convective air flow -which will be simulated in the next paragraph-, the sedimentation, the interception, and finally the Brownian motion.

In the upper airways, the diameter of deposited particles differs in each region. In the larynx mostly extremely small particles in the range of few nm and extremely large particles with a diameter of about 1-10 μm can be found. In the tracheobronchial region, the typically particle size is between 1 and 100 nm, but also very large particles in a range of a few μm can deposit in this region [77,81]. In the field of drug delivery, it is common to use particulate matter with a size of several μm as an aerosol, being inhaled in the upper lung. These particles will deposit in the upper trachea by a convective flow and then release significantly smaller particles, which are able to penetrate the mucus layer by diffusion.

Due to the low Reynolds number, we assume a laminar flow in the lung. Additionally, we can also neglect the sedimentation effect of particles, due to their negligible mass. Nevertheless, the particle mass will be considered to calculate the kinetic energy, as shown in Eq. 34, but to simplify, in this study we use impaction as the only essential deposition effect to simulate the particle deposition in the lung. In our model, Brownian motion, which mostly appears in the alveoli, and interception, which is similar to a filtration effect and mainly appears for filamentous particles, also do not play a role for simulating the particle deposition in the upper airways.

There exist studies, which deal with the simulation of the air flow and the particle deposition in the lung. To compare our results, the following Table 6 shows the average velocity in different regions of the human lung and also the size of the particles, which are mostly found in these regions. These values are from different published studies, dealing with the simulation of particle deposition in the lung due to a convective air flow. The inlet velocity, respectively the percentage of deposited particles are shown in brackets.

Table 6: Exemplary studies of CFD in the human lung to simulate the velocity and size distribution of particles in different regions of the lung (the inlet velocity, respectively the percentage of the deposited particles are shown in brackets).

Ref.	Velocity [m/s] in bronchia	Particle size [μm] in larynx	Particle size [μm] in trachea	Particle size [μm] in bronchia
[79]	0.7-0.8 (1.2)	-	10 (35)	8-10 (10-7)
[82]	-	0.001 (6)	0.001 (10)	0.001 (3)
[83]	-	-	0.001 (33)	0.001 (29)
[78]	-	0.001 (36)	0.001 (15-36)	0.001 (15)
[84]	0.1 (2.0)	-	-	-

6.1.4 Computational Fluid Dynamics (CFD)

The assumed laminar flow of the inhaled particles through the upper airways will be simulated by using CFD. The discretization of the three-dimensional domain of the lung geometry with an extremely fine mesh, respectively low mesh size, is very important. In particular, this is due to the computation of the particle velocity near to the boundary, where the mesh size has to be lower than the respective part of the lung geometry, which will be investigated. So, to consider the effects at the boundary layer, a finer rectangular mesh instead of a triangular mesh is used at the boundary domains.

The order of the necessary steps to simulate fluid dynamics is given in Table 7:

Table 7: Order and description of the steps to simulate flow dynamics.

Step-no.	Step description
#1	Building the geometry
#2	Meshing (pre-processing)
#3	Choosing the material / input of the material parameters
#4	Choosing the system equations
#5	Choosing the boundary and initial conditions
#6	Choosing the solver
#7	Solving
#8	Post-processing

Finally, this method allows us to calculate the kinetic energy of the particles, impacting on the mucus surface. This kinetic energy will then be compared with the Brownian diffusive energy and finally with the necessary deformation energy of a mucin fiber, which have been calculated in the prior chapter.

6.2 Computation of the velocity profile and the kinetic energy

6.2.1 Velocity profile

In the Figure 54 the velocity profile, respectively the absolute velocity, in the larynx and the trachea is shown for the symmetrical lung model (upper Figure) and the mucus layer model of the lung (lower Figure).

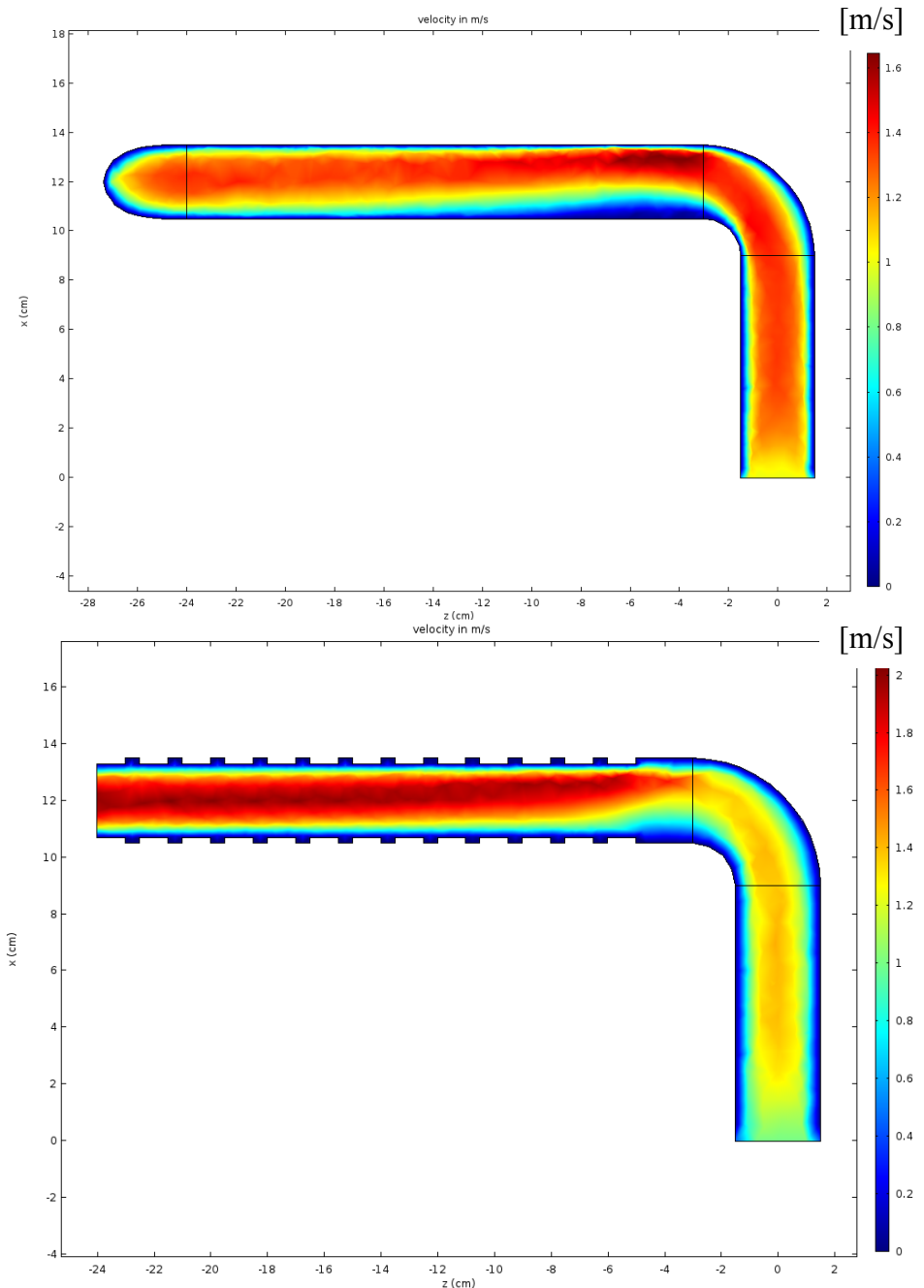


Figure 54: Velocity profile of the larynx and the trachea for the symmetrical lung model (upper Figure) and the mucus layer model of the lung (lower Figure) with an inlet velocity of 1 m/s.

Fig. 55 and Fig. 56 show the velocity profile, respectively the absolute velocity, in the upper and the lower bronchia, respectively, each for the symmetrical (upper Figure) and the asymmetrical (lower Figure) lung model.

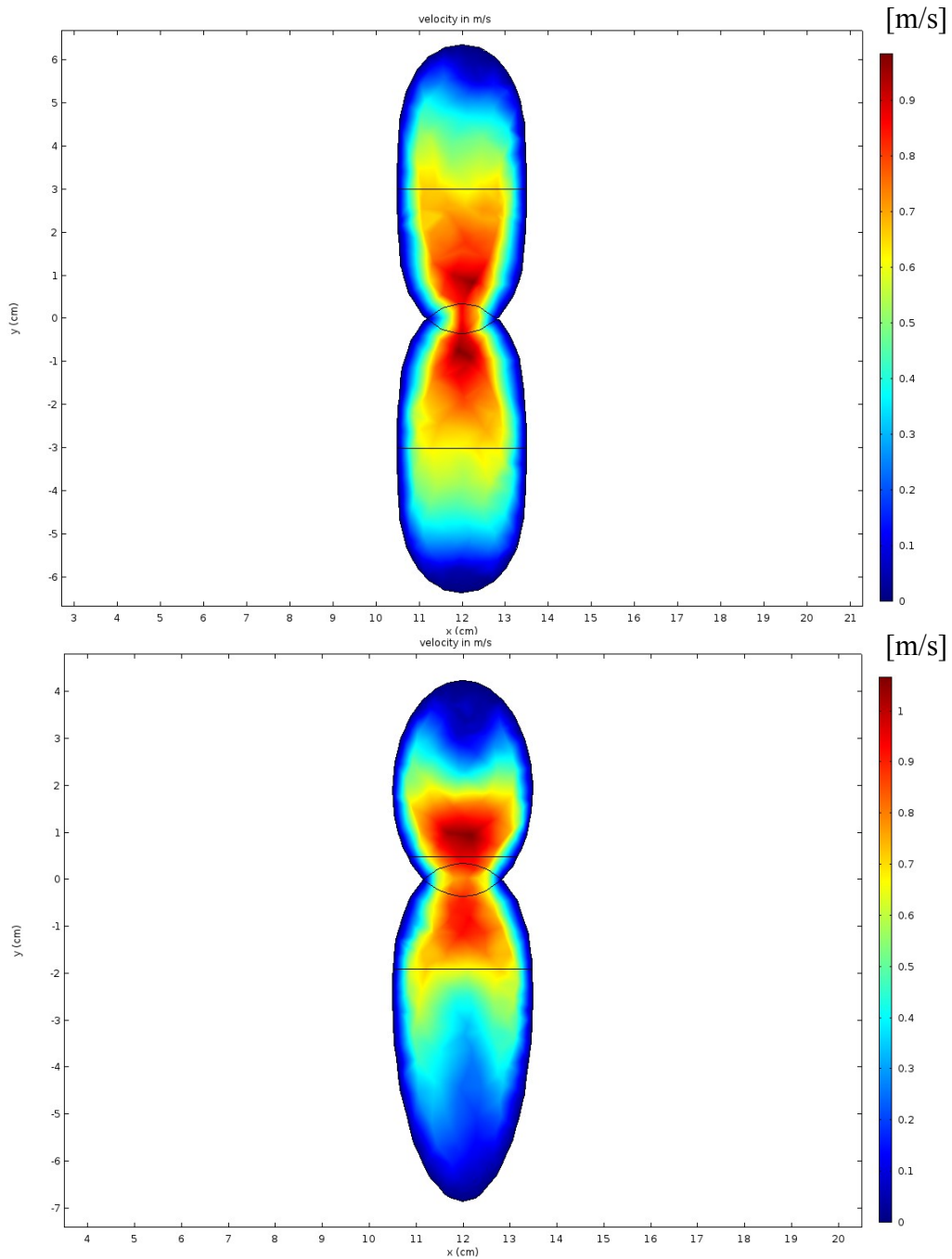


Figure 55: Velocity profile of the upper bronchia for the symmetrical lung model (upper Figure) and the asymmetrical lung model (lower Figure) with an inlet velocity of 1 m/s.

Here, the asymmetrical velocity distribution and hence the asymmetrical distribution of particles in the bronchia become obvious.

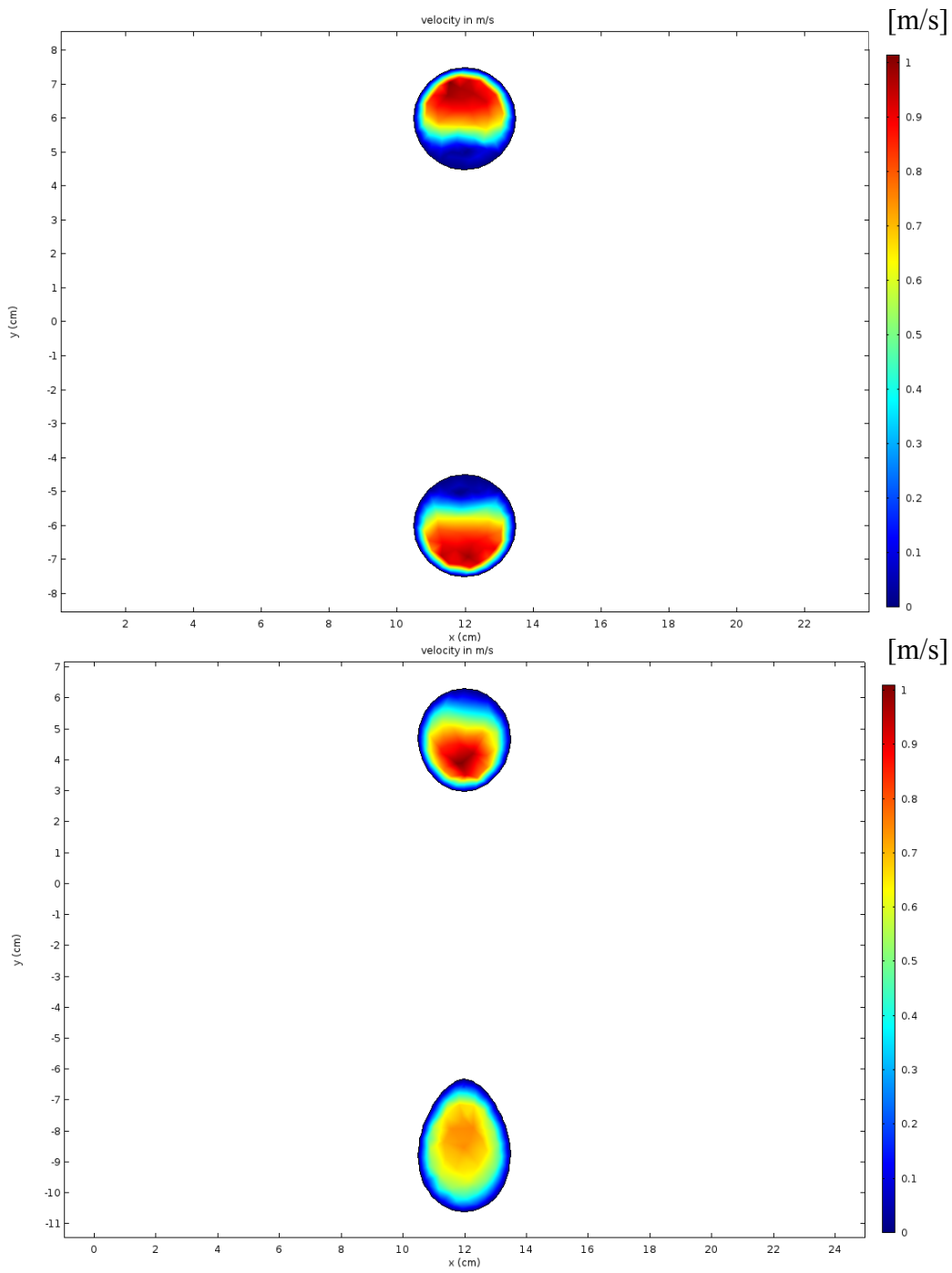


Figure 56: Velocity profile of the lower bronchia for the symmetrical lung model (upper Figure) and the asymmetrical lung model (lower Figure) with an inlet velocity of 1 m/s.

As expected, due to the asymmetrical geometry, in the right bronchia of the lung (lower section in the lower Figure of Fig. 56), the velocity is significantly lower, which leads to a higher accumulation of particles.

6.2.2 Calculation of the kinetic energy and comparison with the necessary deformation energy

The following Table 8 shows the results from the CFD-simulations with the corresponding velocities at the respective region (averaged velocity of the cross section in each region). Additionally, the resulting kinetic energy for exemplary particles with a diameter of 200 nm and a particle density of 1000 kg/m³ is shown.

Table 8: Results of the CFD-simulations (velocity and kinetic energy of the deposited particles) in three regions of the lung for different inlet velocities.

Model	Inlet-velocity [m/s]	Velocity [m/s] in larynx	Velocity [m/s] in trachea	Velocity [m/s] in bronchia	Kin. energy [J] in larynx	Kin. energy [J] in trachea	Kin. energy [J] in bronchia
Sym.	0.5	0.5	0.45	0.23	5.2E-19	4.2E-19	1.1E-19
Asym.	0.5	0.5	0.45	0.23	5.2E-19	4.2E-19	1.1E-19
Mucus	0.5	0.47	0.4	-	4.6E-19	3.4E-19	-
Sym.	0.65	0.65	0.58	0.31	8.9E-19	7.1E-19	2.0E-19
Asym.	0.65	0.65	0.58	0.29	8.9E-19	7.1E-19	1.8E-19
Mucus	0.65	0.61	0.52	-	7.8E-19	5.7E-19	-
Sym.	0.85	0.85	0.76	0.4	1.5E-18	1.2E-18	3.4E-19
Asym.	0.85	0.85	0.77	0.39	1.5E-18	1.2E-18	3.2E-19
Mucus	0.85	0.8	0.67	-	1.3E-18	9.4E-19	-
Sym.	1	1	0.9	0.47	2.1E-18	1.7E-18	4.6E-19
Asym.	1	1	0.9	0.45	2.1E-18	1.7E-18	4.2E-19
Mucus	1	0.94	0.79	-	1.9E-18	1.3E-18	-

After comparing these results with the published data from Table 6, we can conclude that the relative loss of velocity (difference between the inlet velocity and the velocity in the bronchia) in [79] is not that high (37 %) as it is in our simulations (54 %), however in [84], the loss of velocity is significantly higher (95 %) than in our simulations. Surprisingly, the deposited particles with the highest percentage, which has been found in the bronchia, have a diameter of only few nanometers or several micrometers (see Table 6). So, there is a negligible amount of particles with a diameter of a few hundred nanometers in the bronchia. To achieve a drug delivery by particulate matter, particles with a size of several micrometers have to be inhaled, which will then release smaller particles with a size of a few hundred nanometers. These smaller particles can penetrate the mucus layer by Brownian diffusion as shown in chapter 4.

Finally, we also compare the kinetic energy from Brownian motion (see section 5.3.2) and the necessary deformation energy from chapter 5.3 with the computed kinetic energy from Table 8. The results of this comparison are shown in Table 9 and 10. The lowest necessary deformation energy has been determined, if the deformation has been prescribed in the negative y-direction, whereas the highest necessary deformation energy was simulated for the prescribed deformation in the negative x-direction.

Table 9: Comparison of the simulated kinetic energy of the CFD-simulations from Table 8 with the minimal and maximal necessary energy to expand the mucus pore, and the Brownian kinetic energy.

Model	Inlet-velocity [m/s]	Necessary deformation energy [J]	Brownian kin. energy [J]	Kin. energy [J] in larynx	Kin. energy [J] in trachea	Kin. energy [J] in bronchia
Sym.	0.5	2.2E-24 - 5.0E-22	6.42E-21	5.2E-19	4.2E-19	1.1E-19
Asym.	0.5	2.2E-24 - 5.0E-22	6.42E-21	5.2E-19	4.2E-19	1.1E-19
Mucus	0.5	2.2E-24 - 5.0E-22	6.42E-21	4.6E-19	3.4E-19	-
Sym.	0.65	2.2E-24 - 5.0E-22	6.42E-21	8.9E-19	7.1E-19	2.0E-19
Asym.	0.65	2.2E-24 - 5.0E-22	6.42E-21	8.9E-19	7.1E-19	1.8E-19
Mucus	0.65	2.2E-24 - 5.0E-22	6.42E-21	7.8E-19	5.7E-19	-
Sym.	0.85	2.2E-24 - 5.0E-22	6.42E-21	1.5E-18	1.2E-18	3.4E-19
Asym.	0.85	2.2E-24 - 5.0E-22	6.42E-21	1.5E-18	1.2E-18	3.2E-19
Mucus	0.85	2.2E-24 - 5.0E-22	6.42E-21	1.3E-18	9.4E-19	-
Sym.	1	2.2E-24 - 5.0E-22	6.42E-21	2.1E-18	1.7E-18	4.6E-19
Asym.	1	2.2E-24 - 5.0E-22	6.42E-21	2.1E-18	1.7E-18	4.2E-19
Mucus	1	2.2E-24 - 5.0E-22	6.42E-21	1.9E-18	1.3E-18	-

As mentioned before, the volume of one fiber is assumed to be 2E-23 m³ (with a thickness of 10 nm and a length of 200 nm) and is needed to calculate the total necessary deformation energy (in Joule) of an object with this volume.

We also compute the velocity and the kinetic energy of particles directly at the boundary of the trachea in the mucus layer model of the lung (see Fig. 53). The results are shown in Figure 57 and in Table 10. To compare the velocity at the boundary, Fig. 57 also shows the averaged velocity in the trachea of the lung model.

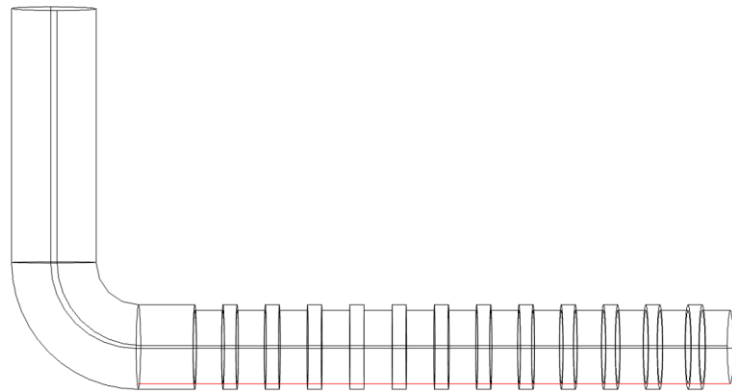
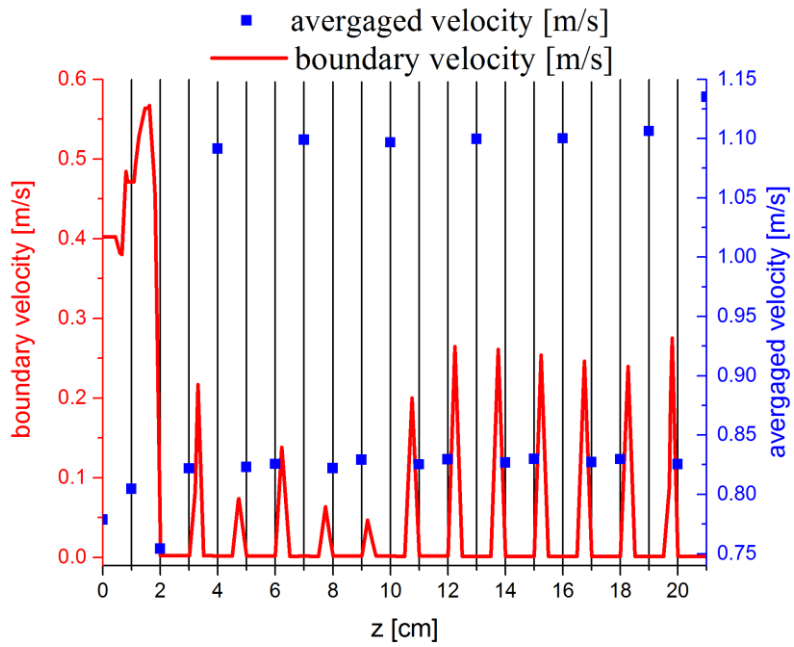


Figure 57: Velocity at the boundary of the trachea (red line) and averaged velocity in the trachea (blue bullets) in the mucus layer model of the lung with an inlet velocity of 1 m/s (lower z-values for the upper trachea and higher z-values for the lower trachea).

The velocity at the boundary is zero, if the mucus layer is present (see sketch in Fig. 57 for the red intersection line at the boundary). Contrary, the averaged velocity at the position, where the mucus layer is reducing the tube diameter is higher than the inlet velocity, due to the reduction of the diameter and the resulting conservation of the volume rate. However, the velocity of the air at the mucus layer is zero (no-slip boundary condition with a velocity of zero at the boundaries), so the particles, which are being transported by this fluid flow, will impact at the mucus layer in case of deceleration, due to their inertia. The resulting kinetic energy is shown in Table 10.

Table 10: Comparison of the simulated kinetic energy from the CFD-simulations of the mucus layer model (velocity at the boundary of the trachea) with the minimal and maximal necessary energy to expand the mucus pore, and the Brownian kinetic energy.

Model	Inlet-velocity [m/s]	Necessary deformation energy [J]	Brownian kin. energy [J]	Velocity [m/s] at the boundary of the trachea	Kin. energy [J] at the boundary of the trachea
Mucus	0.5	2.2E-24 - 5.0E-22	6.42E-21	0.04	3.4E-21
Mucus	0.65	2.2E-24 - 5.0E-22	6.42E-21	0.05	5.2E-21
Mucus	0.85	2.2E-24 - 5.0E-22	6.42E-21	0.07	1.0E-20
Mucus	1	2.2E-24 - 5.0E-22	6.42E-21	0.08	1.3E-20

The kinetic energy of inhaled particles is significantly higher than the necessary deformation energy, whereat the former should be higher, if bigger particles will be inhaled due to the mass dependency of the kinetic energy (see Eq. 34). Also the Brownian diffusive energy of a particle at 37 °C, which is generally lower than the kinetic energy of a 200nm-particle in an air stream, is still high enough for a particle to penetrate the mucus layer. We showed that, the particle size should be high enough to achieve the necessary deformation energy after impaction at the mucus layer and to deposite in the bronchial regions, but only extremely small particles yield in a Brownian diffusive energy, which is high enough to expand the pores. So, as mentioned before, particles in the µm-range should be inhaled and release smaller nanoparticles after impaction, to achieve a penetration of the mucus layer by diffusion.

However, it is possible for a particle, which is bigger than the mucus pore (distance between two mucin fibers), to pass this pore by Brownian motion or inhalation without applying an external force. Although, the mucin fibers have to be very thin (10 nm) to yield the necessary deformation after applying relatively low energies, already particles with a diameter of 80 nm and a velocity of 0.06 m/s achieve the necessary kinetic energy (with the mentioned assumptions: fiber thickness of 10 nm, fiber length of 200 nm, and a Young's modulus of 100 Pa). So, future investigations should deal with the simulation of the necessary deformation energy of mucin fibers with different thicknesses, lengths, and Young's moduli and also considering various pore and particle sizes. Nevertheless, inhaling particles with a size of several micrometers, which are releasing smaller nanoparticles -after impaction on the mucus surface-, could be a very efficient way to deliver drugs and therapeutics to the lung epithelial.

6.3 Conclusions

The air flow simulations of various upper lung models with four different inlet velocities showed that, the resulting kinetic energy is high enough to deform the mucin fibers in a way, that allows deposited particles to penetrate the mucus pores. So, under the given assumptions (fiber length and thickness, rheological and mechanical properties), it is possible for a particle to pass the mucus pore -at the interface between mucus and breathing air- after being inhaled and impacting on the mucus layer. We showed, that there is a higher accumulation in the right bronchia, due to the asymmetrical structure of the upper airways and the resulting lower velocity, as it is in accordance with literature. The loss of velocity in the bronchi is also in good agreement with literature and lies at approx. 50 %. In the mucus model of the lung, where we modeled the mucus layer as a periodic restriction of the tube diameter, the velocity near to the boundary is almost zero, but nevertheless high enough to yield a sufficiently high kinetic energy. In addition, we showed a sufficiently high Brownian diffusive energy to penetrate the mucus pores by passive Brownian motion. Finally, we can conclude, that microparticles, which are inhaled, penetrate the mucus surface by impaction and then, after being dispersed in extremely small nanoparticles, pass the mucus pores by Brownian diffusion to distribute within the mucus network.

7 Fluorescence Recovery after Photobleaching (FRAP) for Studying Particle-Mucus Interactions

7.1 Introduction

The determination of the fluorescence of human pulmonary mucus and polystyrene particles after photobleaching is a very efficient way to measure the diffusivity of these particles over a longer time range (720 s) and larger distances. FRAP means hereby a complete vanishing of the fluorescence at a certain time (photobleaching), after which the recovery of the fluorescence of both investigated materials will be measured, using a confocal laser microscope [69].

The advantages of this method obviously are the very long time range and the large area, in which the bleaching and fluorescence measurements take place, but also the possibility to investigate the particle diffusivity on the one hand and similarly the structure of the mucus on the other hand. One disadvantage is certainly, that the particle diffusion in the z-direction cannot be determined. So, similar to particle tracking experiments, the diffusion in three dimensions will be interpreted as a projected two-dimensional diffusion. However, as being applied in [14], the 3D-MSD will be determined to be the 3/2-fold of the projected 2D-MSD. There are also several problems, appearing during the FRAP-experiments, which are emerging air bubbles, the adhesion of particles at the cover glass, and the missing clear interface between particles and mucus. To avoid these problems, the particle-mucus mixture has to be vortexed before and we used a relatively high particle concentration of 2.4% (v/v).

7.2 Materials & Methods

Native porcine pulmonary mucus was obtained from the tracheas of slaughtered pigs by cutting the trachea and isolating approximately 10 cm of windpipe. The tracheas were stored on ice for mucus extraction and prior to this extraction procedure, the tracheas were cut in half longitudinally. The mucus was gently scratched from the luminal surface (approximately 100–300 µL of mucus per sample). The frozen mucus samples were thawed at 4 °C the day prior to FRAP experiments. The following day, the samples reached room temperature and thereafter 60 µL of mucus was mixed with 1.5 µL of the carboxylated green-fluorescent polystyrene microsphere particle dispersions. The samples were then transferred into adhesive gastight sealing chambers (Gene Frame, Thermo Scientific), and sealed with cover slides. The FRAP experiments were conducted using a LSM 710 Axio Observer confocal laser scanning microscope (Zeiss, Germany) with an Apochromat 40×1.1 objective equipped with a 488 nm laser (LASOS RMC 7812 Z2). The stained mucus was detected in the green channel (excitation 488 nm, detection 467–554 nm) and the fluorescent nanoparticles in the red channel (excitation 561 nm, detection 624–707 nm). The sample temperature was maintained at 37 °C. A time-series analysis was programmed with the following settings: Prebleaching images were recorded at 2% laser transmission, immediately followed by bleaching with the laser transmission set at 100%, and a postbleaching recovery for a duration of 760 s at a frame rate of 30 frames per minute with the laser transmission again set at 2%. The fluorescence intensity after bleaching was defined as zero, and the intensity at t = 0 was subtracted from all values. The intensity values were normalized by dividing each obtained value by the difference between the intensities prior to and directly after bleaching [69].

7.3 Imaging and Evaluation

7.3.1 Imaging of the particle-mucus interaction

Figure 58 shows the fluorescence imaging, using the confocal laser microscope, with the green labeled mucus and the red labeled particles. Most of the particles are trapped in the mucus cells, but nevertheless we see a lot of rapid particle movement in the video sequence of these images . However, this rapid particle movement takes place in very small length scales and therefore, the diffusivity of the particles in mucus seems to be extremely restricted. This restricted diffusion is also obvious in Figure 60 and 61, where the fluorescence intensity seems to approximate to a constant value for longer time scales. As shown in the passive microrheology experiments in section 5.2.2 (Figure 42 and supplementary material) and in the FRAP-experiments (Fig. 60 and 61), the MSD and the fluorescence intensity, respectively, approximates to a constant value, which let us conclude, that the particle diffusion in mucus is totally restricted for longer time and length scales. So, the MSD in particle tracking experiments, respectively the fluorescence intensity in FRAP-experiments, can be easily fitted and predicted by numerical simulations with $p_M = 0$ ($r = 1$), as well as by analytic approximations (see Eq. 7 in section 4.1.2).

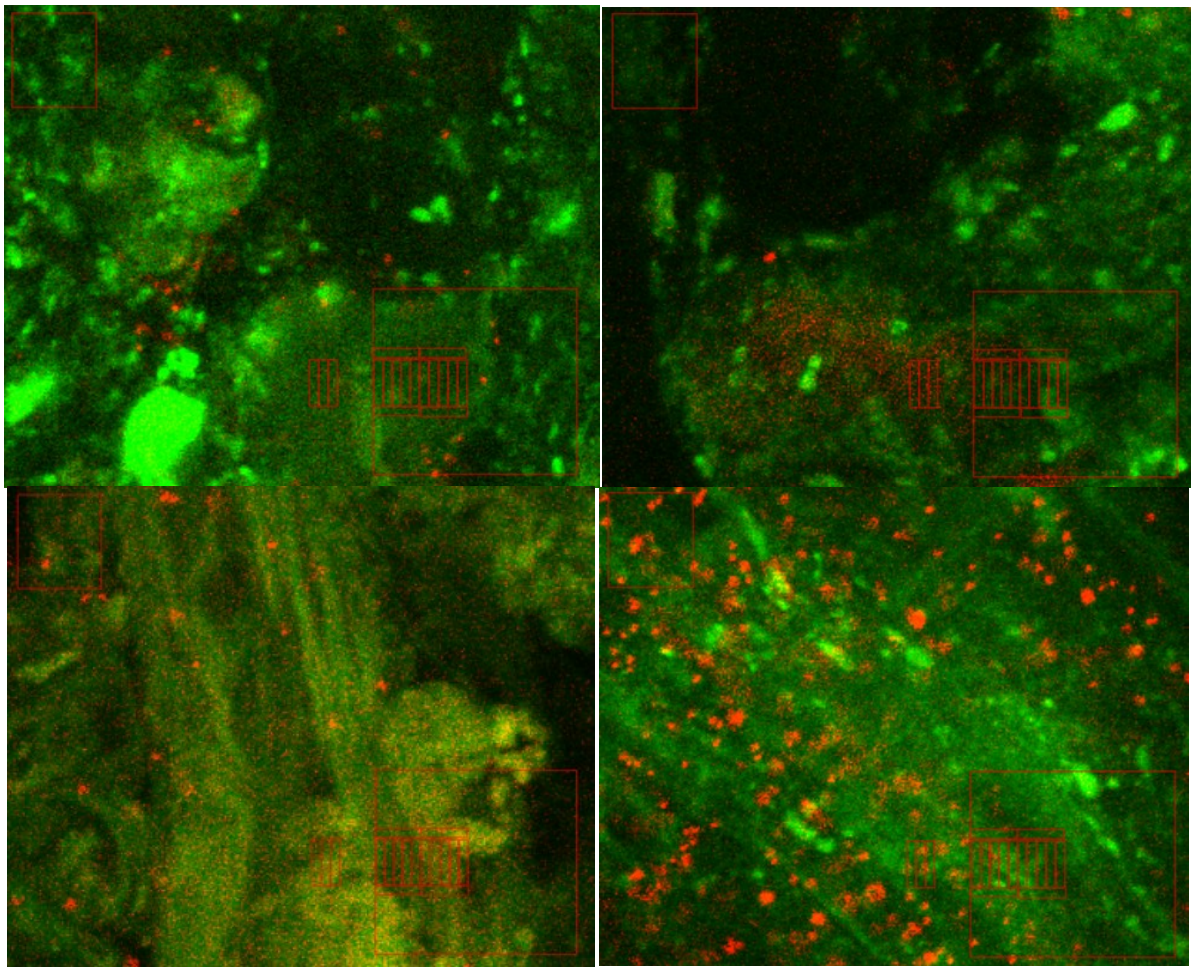


Figure 58: Four different mucus samples (green area) with interacting nanoparticles (red labeled regions).

7.3.2 Evaluation of the particle diffusivity in mucus

To calculate the diffusivity of particles with a diameter of 100 nm in human pulmonary mucus, we use a scaffold with totally 19 regions (see Fig. 59). Here, the regions #1-#10, #16-#19, and #14 will be bleached, whereas the remaining regions serve as control-regions. After approx. 117 s, all regions, except the control regions, are bleached and the fluorescence intensity is determined for 718 s.

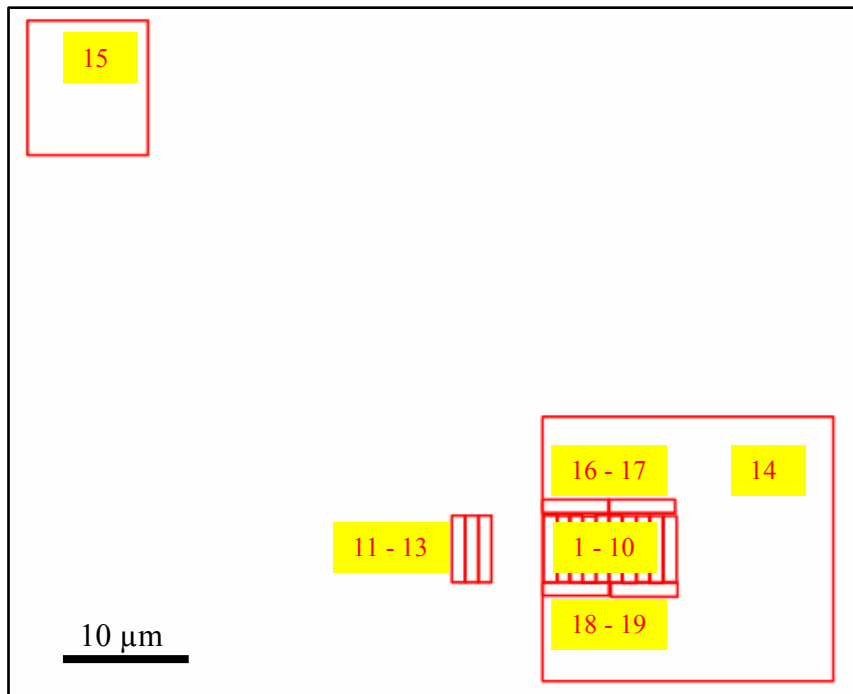


Figure 59: Scaffold for the fluorescence measurements after photobleaching.

Unfortunately, most of the investigated particles are more or less trapped inside a mucus cell and therefore it is hard to determine a long-time diffusion coefficient from the FRAP data. The following Figure 60 shows the normalized fluorescence intensity after the photobleaching of the regions 1-5.

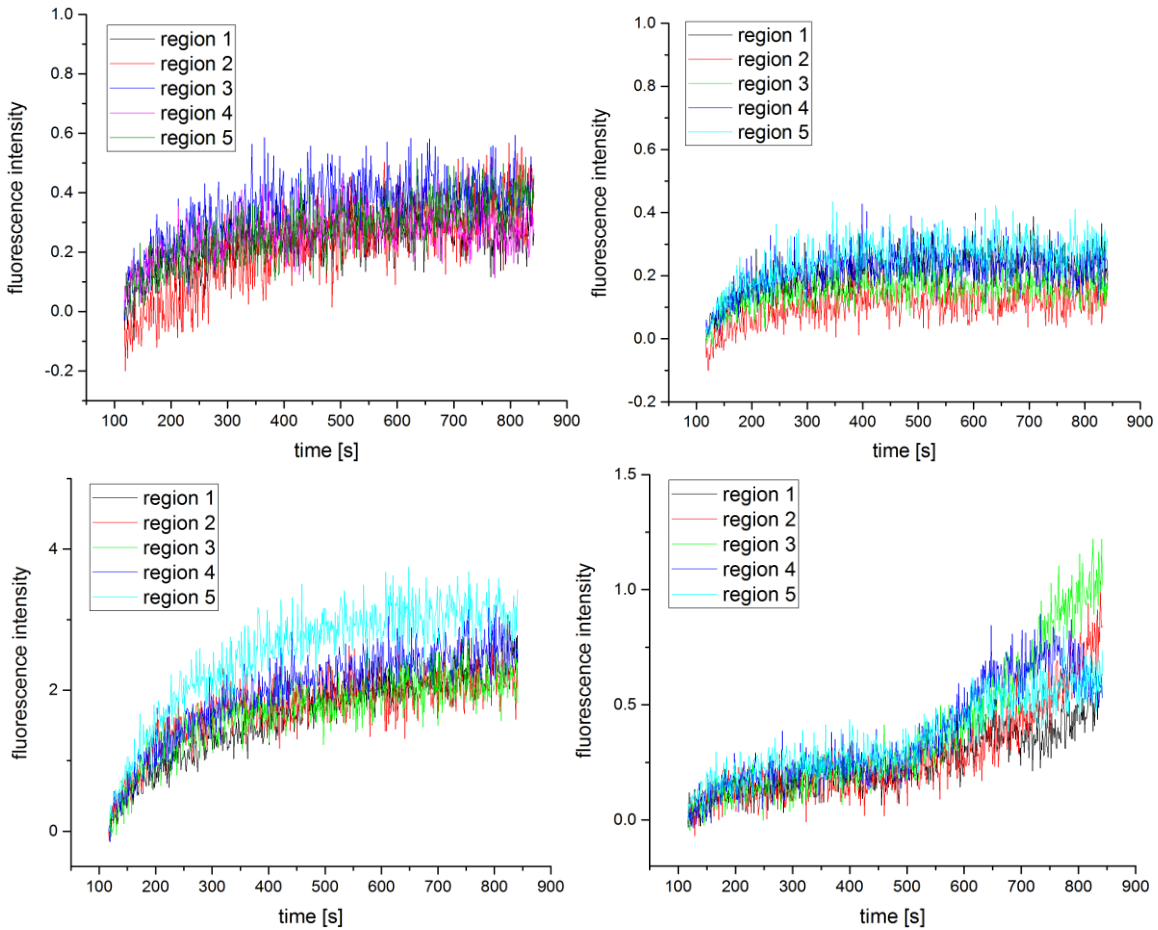


Figure 60: Normalized fluorescence intensity of the regions 1-5 (see Fig. 59) of four different samples.

Here, we can see an obvious increase of the fluorescence with increasing time, whereat there are differences in the slope of the curves, as well as in the normalized values of the fluorescence intensity. Due to the fact, that there is no clear particle concentration gradient between the single regions 1-5, and therefore no clear diffusive direction, it is almost impossible to determine a diffusion coefficient from these results. For this reason and due to the relatively high signal noise (in some extent, the normalized values are higher than 100 %), in the next step, we only use the fluorescence data of region 14 and the control region 15, as shown in Figure 61. As we know the area of each region, we can calculate a diffusion coefficient for region 14 and 15. However, region 15 was not photobleached, thus we use this region as control for the bleached region 14.

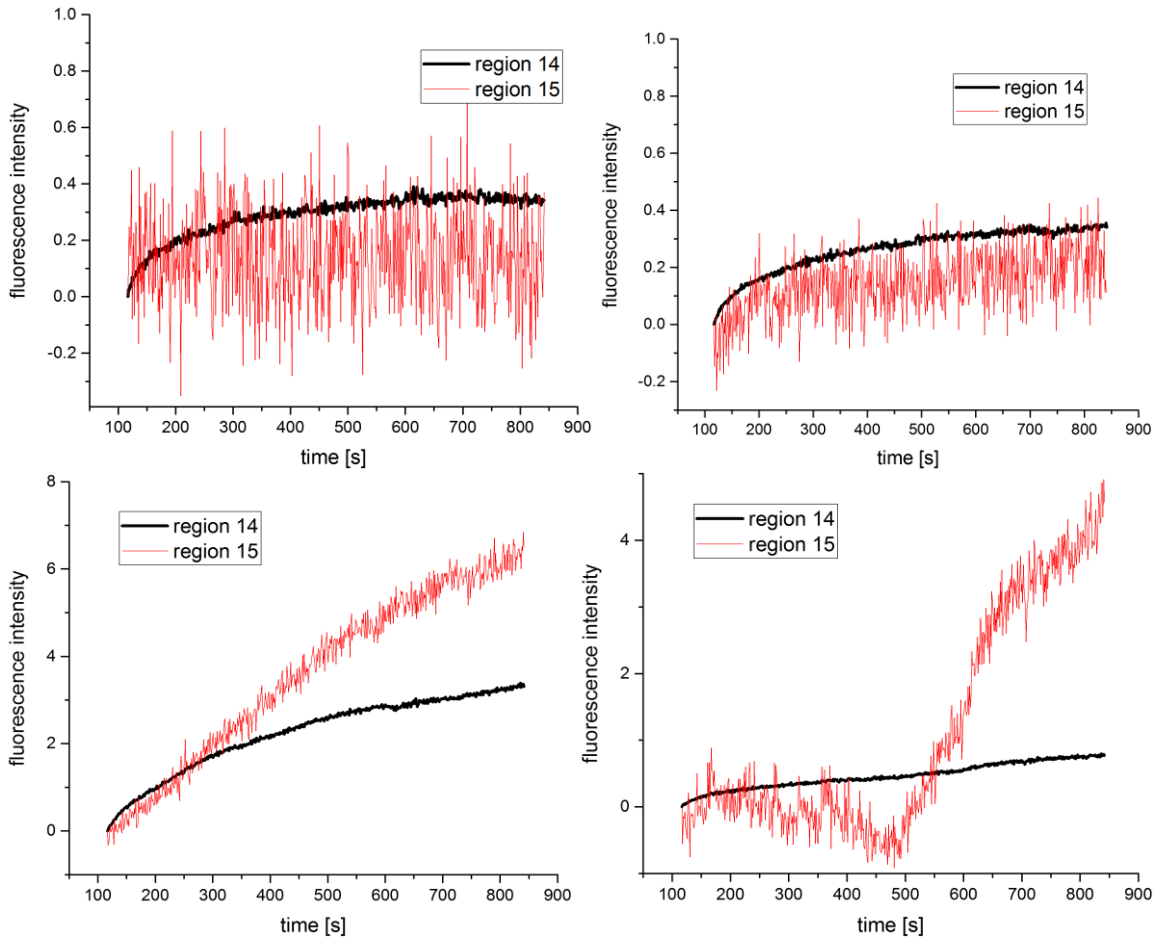


Figure 61: Normalized fluorescence intensity of the regions 14 and 15 (see Fig. 59) of four different samples.

Here, again the differences in the shape of the curves and the normalized values are obvious, but in particular, the results from the samples in the upper row of Figure 61 (#1 and #2 in Table 11) are well suited to calculate a diffusion coefficient, because there is almost no increase of the fluorescence intensity in the control region (region 15). Nevertheless, the normalized value of the fluorescence intensity in region 14 of sample #3 (lower left Figure) is mostly higher than one. In this case, there is a higher fluorescence intensity of the particles than prior to the photobleaching. Subsequently, after the photobleaching there are particles diffusing in the z-direction into the bleached area, leading to an increase of the fluorescence intensity. Consequently, we have to consider this three-dimensional diffusion in the two-dimensional experimental setting.

In Table 11 the calculated diffusion coefficients in [intensity μm^{-2}] after totally 835 s for the regions 14 and 15, and the difference between these two regions are shown. To reduce the diffusive effects of particles, moving in the z-direction, we have to use the difference of intensity between region 14 and the control region 15.

A possibility to consider the diffusion of particles in the z-direction is to calculate the 3D-diffusion from the projected 2D-diffusion (see Suh et al. [14]), as it is shown for region 14. The values in brackets show the time-dependent diffusion coefficient in [intensity $\mu\text{m}^{-2} \text{s}^{-1}$].

Table 11: Diffusion coefficients after 835 s (time-dependent ones in brackets) from the fluorescence recovery after photobleaching in region 14 and 15, as well as the difference between these regions to reduce diffusive effects from particles moving in the z-direction, and the calculated 3D-diffusion from the projected 2D-diffusion in region 14 to consider the diffusion of particles in the z-direction. The upper four rows are calculated with the normalized values of the fluorescence intensity (n.).

Sample	Region 14	Region 15	Difference	Region 14 (3D)
#1 (15D) n.	6.9E-4 (9.5E-7)	3.7E-3 (5.1E-6)	-3.0E-3 (4.2E-6)	1.0E-3 (1.4E-6)
#2 (21A) n.	6.8E-4 (9.4E-7)	1.1E-3 (1.5E-6)	-4.2E-4 (-5.8E-7)	1.0E-3 (1.4E-6)
#3 (21B) n.	6.6E-3 (9.1E-6)	6.5E-2 (9.0E-5)	-5.8E-2 (-8.1E-5)	9.9E-3 (1.4E-5)
#4 (21D) n.	1.6E-3 (2.1E-6)	4.6E-2 (6.3E-5)	-4.4E-2 (-6.1E-5)	2.4E-3 (3.3E-6)
#1 (15D)	6.2E-3 (8.6E-6)	3.7E-3 (5.1E-6)	2.5E-3 (3.5E-6)	9.3E-3 (1.3E-5)
#2 (21A)	5.9E-3 (8.1E-6)	1.1E-3 (1.5E-6)	4.8E-3 (6.6E-6)	8.9E-3 (1.2E-5)
#3 (21B)	3.0E-2 (4.2E-5)	6.5E-2 (9.0E-5)	-3.5E-2 (-4.8E-5)	4.5E-2 (6.2E-5)
#4 (21D)	9.9E-3 (1.4E-5)	4.6E-2 (6.3E-5)	-3.6E-2 (-5.0E-5)	1.5E-2 (2.1E-5)

As shown, in all samples, the area-specific diffusivity in the control region 15 is significantly higher than in the bleached region 14, if the values of the fluorescence intensity are normalized. If the values are not normalized, only in the samples #3 and #4 the diffusivity in the control region 15 is significantly higher than in the bleached region 14. We expected the intensity in the control region to be constant at a value of zero, due to the assumption, that as much particles move in this region as particles move out of the region. As shown in Figure 61, this assumption is only valid for the samples #1 and #2.

Contrary to the simulations of Brownian diffusion (see chapter 4), in these experiments, the subdiffusive behavior of particles in mucus is not a transient effect. So, depending on the experimental setting, the diffusion of particles is totally trapped -reflection probability $r = 1$ in our simulations and a constant MSD, respectively fluorescence intensity (see sample #1)-, subdiffusive -reflection probability $r < 1$ and a MSD, respectively fluorescence intensity, $\sim \alpha$ with $\alpha < 1$ (see sample #2)- or transient subdiffusive.

7.4 Conclusions

The fluorescence recovery after photobleaching is a good method to visualize the extremely heterogeneous and complex structure of mucus. Hence, the particles are mostly trapped inside the single mucus cells and their diffusion is extremely confined, which is expressed by the constant fluorescence values (lower than the initial value before bleaching) even after 15 minutes. The calculation of the diffusivity of 100 nm-particles in mucus showed, that it is very hard to quantitatively describe the diffusion in mucus by this method, due to the 2D-projection of a 3D-movement, as it is also obvious in particle tracking experiments. So, there are several methods to determine the diffusivity of particles in mucus, leading to different conclusions about the type of diffusion (totally trapped, subdiffusive or transient subdiffusive).

8 Assumptions and Hypotheses

To simulate the Brownian motion of particles in a confined geometry, we used a simplified cell-aperture model, which we abstracted to a cavity-membrane model with permeable membranes and certain transmission probabilities. The only essential parameters, needed in this model, are the diffusion coefficients for the short and long time limits, the size of the cavity edge, respectively the distance between the membranes, and the permeability of the membranes. We assumed a regular array of cells and windows, respectively membranes, and mixed boundary conditions to simulate the mucus structure and its properties. So, as we used an isotropic geometry with permeable membranes, the complex model for simulating Brownian motion of particles in a three-dimensional geometry can be reduced to a one-dimensional membrane model. However, we simulated the (Fickian) diffusion of particles, based on concentration gradients to compare it with two (Brownian and Fickian) diffusion models, based on permeable membranes. In case of the Fickian diffusion, based on concentration gradients, we used a two-dimensional cell-window, respectively cell-membrane, model with an array of cells, connected by windows, membranes respectively, only in one direction. In our diffusion models, we assumed the fluid to be purely viscous, the membranes and walls to be rigid, and particles, respectively mucus, without any electrostatic or chemical interactive properties. Nevertheless, we are able to simulate the diffusion of particles with different properties and diameters in mucus from different sources, as well as to predict the time to penetrate a certain distance in the mucus layer. To simulate the concentration-gradient based diffusion, we assumed an equal distribution of particles as diluted species at one boundary and vanishing particles at the opposite boundary in direction of diffusion. The windows in this model represent the mucus pores, which are voids in the mucin fiber network. To determine the necessary deformation energy of such a mucin fiber to achieve a certain expansion of the mentioned void, we assumed the fiber to be an elastic beam with a specified Young's modulus, yielded from rheometry and optical tweezer experiments. One edge of the fiber was assumed to be fixed, whereas the opposite edge was deflected in the y-direction or deformed in the x-direction. Consequently, the void between two ideally identical fibers was expanded in a way, that allows a particle to pass through. The assumption of the fiber, being an elastic beam, is not that realistic, as the mucin fibers are more viscoelastic and semiflexible, but in a first approach it is valid to estimate the deformation energy.

To verify, if the particle impact is high enough to reach the needed deformation of the fibers, we simulated the convective air flow in different lung models. We used various inlet velocities, which result in realistic flow rates during the inhalation of an aerosol. As we assumed an overdamped movement of particles in this aerosol and due to the vanishing particle mass, we neglected the particle movement in the convective air flow. Subsequently, we calculated the kinetic energy of the particles by computing the air velocity in different regions of our lung models. This assumption is only valid for particles with a negligible particle friction force in the air stream. However, our model is very simplified, concerning the particle-air interactions, but nevertheless we used a nearly realistic asymmetrical lung model with comparable inlet flow rates and pressure conditions. So, we are able to determine the kinetic energy of an inhaled particle and compare this energy with the necessary deformation energy of a mucin fiber, considering measured Young's moduli.

9 Summary and Outlook

We developed four diffusion models to simulate the particle movement through a cell array, representing the mucus network. We achieved realistic diffusion models by assuming the mucus to be an array of cells with periodic open windows or with periodic diffusion barriers, each barrier provided with a different diffusion coefficient. Both models were compared with a one-dimensional model, based on periodic permeable membranes, whereat we compared the size of the open windows with the permeability parameter and the diffusion coefficient of the diffusive barriers with the effective diffusion coefficient, respectively. Two one-dimensional models are based on permeable membranes with a certain permeability parameter and either random or constant permeation probabilities of the particles for each investigated time step. The two-dimensional models are based on a concentration gradient and with particles as diluted species, contrary to the random particle walk, which is assumed in the one-dimensional models. The two-dimensional models can be interpreted more easily, since they are based on measureable parameters, such as the size of a mucus cell and of the pores in the mucus network.

We explained the reported subdiffusion of particles in mucus by simulating the Brownian diffusion of particles in a confined geometry, made from permeable membranes in analogy to mixed boundary conditions. A heuristic analytic approximation formula was substantiated by numerical simulations. The applied model predicted a normal diffusive behavior at very short $\tau \rightarrow 0$ and long times $\tau \rightarrow \infty$, as it is observed in several particle tracking experiments. In between these time scales, the "subdiffusive" regime appeared to be a transient effect, $MSD \sim \tau^\alpha$, $\alpha < 1$. The only necessary parameters in the model are the diffusion-coefficients D_0 and D_{eff} , and the distance between the permeable membranes L . Our results were in agreement with published experimental data for realistic assumptions of these parameters. We showed, that particles with a diameter lower than 40 nm are able to pass through a mucus layer with a thickness of approx. 55 μm (interstitial fluid viscosity $\eta = 7 \text{ mPas}$) within a clearance time of 15 min by passive Brownian motion.

Simulations of the probability density function of the particle displacement showed that, even 500nm-particles pass a specific mucus layer thickness. Consequently, these big particles are not totally restricted in their movement. None of the investigated uncoated and coated particles with different sizes are totally trapped inside a mucus cell, but their diffusivity is significantly different.

Some of the 100nm-particles are able to overcome a distance of 10 μm already after 100 seconds. After calculating the mean passage time, we concluded, that there is no possibility for any of the investigated particles to overcome a mucus layer of 55 μm thickness within a mucus turnover time of 15 minutes by passive Brownian motion. However, in case of cystic fibrosis mucus, this turnover time is significantly higher. Subsequently, mucus from patients with lung disease can be passed by some particles, if the clearance time is comparable to the mean passage time. Nevertheless, only particles with a diameter of below 300 nm are able to overcome a fluid layer with a viscosity of 1 mPas, respectively the maximal viscosity of a fluid to enable a particle displacement (100nm-particle) of 55 μm within 15 minutes is 3 mPas. Consequently, there have to be some active particle motion processes to achieve a faster particle penetration of mucus by affecting the particle displacement.

To achieve a better insight in the system, an analytic relation between the permeability p_M in $\text{s}^{-1/2}$ and the effective diffusion coefficient $D_{\text{eff}}(p_M)$ will be helpful (see Fig. 10 and Fig. 14). The model predicted normal diffusion for short and long times and therefore, further experiments with a wider range of time lag in the $\text{MSD}(\tau)$ -data could verify our predictions. Additionally, an experimental validation of the Gaussian shape of the probability density function of the particle displacement still remains missing. However, we are able to simulate the probability density function of the particle displacement in mucus by using the assumed values for the three essential parameters $D_{\text{eff}}(p_M)$, D_0 , and L .

We investigated the similarities and differences in the viscoelastic (macro- and microrheological) properties of mucus from pulmonary and intestinal regions of healthy pigs. Our results revealed significant differences between respiratory and intestinal mucus, in the macro- and microscale as well. The measured Young's modulus was used to simulate the necessary deformation energy of a mucus fiber. This fiber deformation yielded in a pore expansion, which allows the particle to pass the mucus layer. The deformation of a mucin fiber can be achieved either by impaction, due to convective particle flow, or by the Brownian diffusive energy. The kinetic energy of an inhaled particle in a convective air flow was computed by simulating the air dynamics in three different lung models. We showed, that the Brownian diffusive energy of a particle, as well as the kinetic energy of an inhaled particle, are high enough to yield a sufficient fiber deformation for the given assumptions. This deformation results in a pore expansion, which allows the particle to pass the mucus pore.

Future investigations of the possibility for particles in a convective flow to penetrate the mucus layer by impaction should deal with a variation of the mucin fiber parameters, such as the Young's modulus, the Poisson number, the density, the length and thickness of the fiber, and also the pore size, as well as the particle size. Furthermore, time-dependent CFD- and deformation-simulations should be executed, as well as flow simulations with integrated particle deposition analysis.

In the last section of this work, we showed by applying fluorescence recovery methods, that particles are mostly trapped inside the mucus structure, as it is also obvious in some particle tracking experiments. Although, the particles are moving rapidly inside a mucus cell, this displacement is within an extremely small area and time lag. Nevertheless, we could discriminate between three different types of diffusion as these are: totally trapped diffusion, subdiffusion, and transient subdiffusion. All of these diffusion types have been detected in the presented experiments and can be predicted by our model simulations.

Due to the projection of the three-dimensional particle movement in mucus to a two-dimensional dataset in experiments (particle tracking and FRAP), a simulation of the projected particle movement in the third dimension should be helpful to quantitatively describe the particle diffusion in non-isotropic materials. However, we must not simulate a 3D diffusion, as we are able to simulate the particle movement through a sequence of permeable membranes in one dimension. By assuming different values of the permeability of the membrane, the distance between the membranes, and the diffusion coefficient in the short time limit, we are able to predict the long-time diffusion in more than one dimension for isotropic models. Subsequently, it is also not necessary to consider physical and chemical properties of the mucus and the particles, as we can put these properties into the three essential parameters $D_{eff}(p_M)$, D_0 , and L .

To close this work, we can finally conclude, that it is possible to simulate the particle impaction at the mucus layer, due to convective air flow, and to compute the resulting kinetic energy, since we developed realistic models of the upper lung. This impaction leads to a pore expansion, which allows the particle to penetrate into the mucus network for given assumptions on the mucin fiber geometry and its mechanical and rheological properties. We developed realistic diffusion models to predict the particle movement inside the mucus structure and to explain the appearing transient "subdiffusive" behavior of the particles.

10 References

- [1] Gehr, P., C. Mühlfeld, B. Rothen-Rutishauser, and F. Blank, 2010. Particle-Lung Interactions Second Edition. informa Healthcare.
- [2] Serda, R. E., 2013. Mass Transport of Nanocarriers. CRC Press.
- [3] Lai, S. K., Y.-Y. Wang, D. Wirtz, and J. Hanes, 2009. Micro and Macrorheology of mucus. *Adv Drug Delivery* 61:86–100.
- [4] Khanvilkar, K., M. D. Donovan, and D. R. Flanagan, 2001. Drug Transfer through mucus. *Advanced Drug Delivery Reviews* 48:173–193.
- [5] Cu, Y., and W. M. Saltzman, 2009. Mathematical modeling of molecular diffusion through mucus. *Adv Drug Delivery* 61:101–114.
- [6] Lieleg, O., and K. Ribbeck, 2011. Biological Hydrogels as Selective Diffusion Barriers. *Trends Cell Biology* 21:543 – 551.
- [7] Lai, S. K., Y.-Y. Wang, and J. Hanes, 2009. Mucus-penetrating nanoparticles for drug and gene delivery to mucosal tissues. *Advanced Drug Delivery Reviews* 61:158–171.
- [8] Kirch, J., A. Schneider, B. Abou, A. Hopf, U. F. Schaefer, M. Schneider, C. Schall, C. Wagner, and C.-M. Lehr, 2012. Optical tweezers reveal relationship between microstructure and nanoparticle penetration of pulmonary mucus. *PNAS* 109:18355.
- [9] Sigurdsson, H. H., J. Kirch, and C.-M. Lehr, 2013. Mucus as a barrier to lipophilic drugs. *International Journal of Pharmaceutics* 453:56–64.
- [10] Boegh, M., and H. M. Nielsen, 2015. Mucus as a Barrier to Drug Delivery Understanding and Mimicking the Barrier Properties. *Basic & Clinical Pharmacology & Toxicology* 116:179–186.
- [11] Schuster, B. S., J. S. Suk, G. F. Woodworth, and J. Hanes, 2013. Nanoparticle diffusion in respiratory mucus from humans without lung disease. *Biomaterials* 34:3439–3446.
- [12] Suk, J. S., Q. Xu, N. Kim, J. Hanes, and L. M. Ensign, 2016. PEGylation as a strategy for improving nanoparticle-based drug and gene delivery. *Advanced Drug Delivery Reviews* 99:28–51.
- [13] Sanders, N. N., S. C. de Smedt, E. van Rompaey, P. Simoens, F. de Baets, and J. Demeester, 2000. Cystic Fibrosis Sputum: A Barrier to the Transport of Nanospheres. *Am J Respir Crit Care Med* 162:1905–1911.
- [14] Suh, J., M. Dawson, and J. Hanes, 2005. Real-time multiple particle tracking: applications to drug and gene delivery. *Advanced Drug Delivery Reviews* 57:63–78.
- [15] Sung, J. C., B. L. Pulliam, and D. A. Edwards, 2007. Nanoparticles for Drug Delivery to the Lungs. *Trends in Biotechnology* 25:563–570.
- [16] Tang, B. C., M. Dawson, S. K. Lai, Y.-Y. Wang, J. S. Suk, M. Yang, P. Zeitlin, M. P. Boylee, J. Fua, and J. Hanes, 2009. Biodegradable polymer nanoparticles that rapidly penetrate the human mucus barrier. *PNAS* 106:19268–19273.

- [17] Suk, J. S., A. J. Kim, K. Trehan, C. S. Schneider, L. Cebotaru, O. M. Woodward, N. J. Boylan, M. P. Boyle, S. K. Lai, W. B. Guggino, and J. Hanes, 2014. Lung gene therapy with highly compacted DNA nanoparticles that overcome the mucus barrier. *Journal of Controlled Release* 178:8–17.
- [18] Lai, S. K., D. E. O'Hanlon, S. Harrold, S. T. Man, Y.-Y. Wang, R. Cone, and J. Hanes, 2007. Rapid transport of large polymeric nanoparticles in fresh undiluted human mucus. *PNAS* 104:1482 – 1487.
- [19] Forier, K., A.-S. Messiaen, K. Raemdonck, H. Deschout, J. Rejman, F. De Baets, H. Nelis, S. C. De Smedt, J. Demeester, T. Coenye, and K. Braeckmans, 2013. Transport of nanoparticles in cystic fibrosis sputum and bacterial biofilms by single-particle tracking microscopy. *Nanomedicine* 8:935–949.
- [20] Lieleg, O., I. Vladescu, and K. Ribbeck, 2010. Characterization of Particle Translocation through Mucin Hydrogels. *Biophysical Journal* 98:1782 – 1789.
- [21] Forier, K., K. Raemdonck, S. C. De Smedt, J. Demeester, T. Coenye, and K. Braeckmans, 2014. Lipid and polymer nanoparticles for drug delivery to bacterial biofilms. *Journal of Controlled Release* 190:607–623.
- [22] Kirch, J., M. Guenther, N. Doshi, U. F. Schaefer, M. Schneider, S. Mitragotri, and C.-M. Lehr, 2012. Mucociliary clearance of micro- and nanoparticles is independent of size, shape and charge: an ex vivo and in silico approach. *Journal of Controlled Release* 159:128–134.
- [23] Bhat, P. G., D. R. Flanagan, and M. D. Donovan, 1996. Drug Diffusion through Cystic Fibrotic Mucus: Steady-State Permeation, Rheologic Properties, and Glycoprotein Morphology. *Journal of Pharmaceutical Sciences* 85:624–630.
- [24] Broughton-Head, V. J., J. R. Smith, J. Shur, and J. K. Shute, 2007. Actin limits enhancement of nanoparticle diffusion through cystic fibrosis sputum by mucolytics. *Pulmonary Pharmacology & Therapeutics* 20:708–717.
- [25] Regnis, J. A., M. Robinson, D. L. Bailey, P. Cook, P. Hooper, H.-K. Chan, I. Gonda, G. Bautovich, and P. T. P. BYE, 1994. Mucociliary Clearance in Patients with Cystic Fibrosis and in Normal Subjects. *Am J Respir Crit Care Med* 150:66–71.
- [26] Dudko, O. K., A. M. Berezhkovskii, and G. H. Weiss, 2004. Diffusion in the presence of periodically spaced permeable membranes. *The Journal of Chemical Physics* 121:1–6.
- [27] Dudko, O. K., A. M. Berezhkovskii, and G. H. Weiss, 2005. Time-Dependent Diffusion Coefficients in Periodic Porous Materials. *Journal of Physical Chemistry B* 109:21296–21299.
- [28] Ditlevsen, S., and A. Samson, 2013. Stochastic Biomathematical Models, Chapter 1 (Introduction to Stochastic Models in Biology). Springer-Verlag.
- [29] Nelson, E., 2001. Dynamical Theories of Brownian Motion. Princeton University Press.
- [30] Muermann, M., 2014. Wahrscheinlichkeitstheorie und Stochastische Prozesse. Springer.
- [31] Harrison, J. M., 1985. Brownian Motion and Stochastic Flow Systems. John Wiley & Sons.
- [32] Beichelt, F., 1997. Stochastische Prozesse für Ingenieure. B.G. Teubner-Verlag.

- [33] Behrends, E., 2013. *Markovprozesse und Stochastische Differentialgleichungen*. Springer-Verlag.
- [34] Schwetlick, H., 1997. *PC-Messtechnik*. Vieweg-Verlag.
- [35] Norris, D. A., and P. J. Sinko, 1997. Effect of Size, Surface Charge, and Hydrophobicity on the Translocation of Polystyrene Microspheres Through Gastrointestinal Mucin. *Journal of Applied Polymer Science* 63:14811492.
- [36] Saltzman, W. M., 2001. *Drug Delivery*. Oxford University Press.
- [37] Erickson, A. M., B. I. Henry, J. M. Murray, P. J. Klasse, and C. N. Angstmann, 2015. Predicting First Traversal Times for Virions and Nanoparticles in Mucus with Slowed Diffusion. *Biophysical Journal* 109:164–172.
- [38] Berezhkovskii, A. M., M. I. Monine, C. B. Muratov, and S. Y. Shvartsman, 2006. Homogenization of boundary conditions for surfaces with regular arrays of traps. *The Journal of Chemical Physics* 124:1–3.
- [39] Makhnovskii, Y., A. Berezhkovskii, and V. Zitserman, 2010. Diffusion in a tube of alternating diameter. *Chemical Physics* 367:110–114.
- [40] Berezhkovskii, A. M., L. Dagdug, and S. M. Bezrukov, 2014. Discriminating between Anomalous Diffusion and Transient Behavior in Microheterogeneous Environments. *Biophysical Journal* 106:L09–L011.
- [41] Berezhkovskii, A. M., L. Dagdug, and S. M. Bezrukov, 2015. Biased diffusion in three-dimensional comb-like structures. *The Journal of Chemical Physics* 142:1–10.
- [42] Berezhkovskii, A. M., L. Dagdug, and S. M. Bezrukov, 2014. From normal to anomalous diffusion in comb-like structures in three dimensions. *The Journal of Chemical Physics* 141:1–7.
- [43] Bezrukov, S., L. Schimansky-Geier, and G. Schmid, 2014. Brownian motion in confined geometries. *The European Physical Journal Special Topics* 223:3021–3025.
- [44] Makhnovskii, Y. A., A. M. Berezhkovskii, and V. Y. Zitserman, 2009. Time-dependent diffusion in tubes with periodic partitions. *The Journal of Chemical Physics* 131:1–5.
- [45] Boukari, H., B. Brichacek, P. Stratton, S. F. Mahoney, J. D. Lifson, L. Margolis, and R. Nossal, 2009. Movements of HIV-Virions in Human Cervical Mucus. *Biomacromolecules* 10:2482–2488.
- [46] Banks, D. S., C. Tressler, R. D. Peters, F. Hofling, and C. Fradin, 2016. Characterizing anomalous diffusion in crowded polymer solutions and gels over decades in time with variable-lengthscale fluorescence correlation spectroscopy. *Soft Matter* 18:1–14.
- [47] Weeks, E. R., and D. A. Weitz, 2002. Subdiffusion and the cage effect studied near the colloidal glass transition. *Chemical Physics* 284:361–367.
- [48] Martin, D. S., M. B. Forstner, and J. A. Käs, 2002. Apparent Subdiffusion Inherent to Single Particle Tracking. *Biophysical Journal* 83:2109–2117.
- [49] Michalet, X., 2010. Mean Square Displacement Analysis of Single-Particle Trajectories with Localization Error: Brownian Motion in Isotropic Medium. *Physical Review E: Statistical, Nonlinear, and Soft Matter Physics* 82:1–26.

- [50] Hansing, J., C. Ciemer, W. K. Kim, X. Zhang, J. E. DeRouchey, and R. R. Netz, 2016. Nanoparticle filtering in charged hydrogels: Effects of particle size, charge asymmetry and salt concentration. *The European Physical Journal E* 39:53.
- [51] Cicuta, P., and A. M. Donald, 2007. Microrheology: a review of the method and applications. *Soft Matter* 3:1449–1455.
- [52] Gillespie, D. T., and E. Seitaridou, 2013. Simple Brownian Diffusion. Oxford University Press.
- [53] Islam, M. A., 2004. Einstein Smoluchowski Diffusion Equation: A Discussion. *Physica Scripta* 70:120–125.
- [54] Kusumi, A., Y. Sako, and M. Yamamoto, 1993. Confined Lateral Diffusion of Membrane Receptors as Studied by Single Particle Tracking (Nanovid Microscopy). Effects of Calcium-induced Differentiation in Cultured Epithelial Cells. *Biophysical Journal* 65:2021–2040.
- [55] Lucena, D., D. Tkachenko, K. Nelissen, V. Misko, W. Ferreira, G. Farias, and F. Peeters, 2012. Transition from single-file to two-dimensional diffusion of interacting particles in a quasi one-dimensional channel. *Physical Review E: Statistical, Nonlinear, and Soft Matter Physics* 85:1–12.
- [56] Nandi, A., D. Heinrich, and B. Lindner, 2012. Distributions of diffusion measures from a local mean-square displacement analysis. *Physical Review E: Statistical, Nonlinear, and Soft Matter Physics* 86:1–13.
- [57] Burada, P. S., P. Hänggi, F. Marchesoni, G. Schmid, and P. Talkner, 2009. Diffusion in Confined Geometries. *Chem Phys Chem* 10:45–54.
- [58] Higham, D. J., 2001. An Algorithmic Introduction to Numerical Simulation of Stochastic Differential Equations. *Society for Industrial and Applied Mathematics* 43:525–546.
- [59] Schuss, Z., 2013. Brownian Dynamics at Boundaries and Interfaces, volume 186. Springer.
- [60] Singer, A., Z. Schuss, A. Osipov, and D. Holcman, 2008. Partially Reflected Diffusion. *SIAM Journal on Applied Mathematics* 68:844/868.
- [61] Bathe, K.-J., 1996. Finite Element Procedures. Prentice-Hall.
- [62] http://www.fachdidaktik.physik.ethz.ch/education/AbgeschlosseneArbeiten/TJenniF_VFiniteElemente.pdf (2011)
- [63] Ripplinger, 2013. Einführung in die Finite Elemente Methode
- [64] Schwarz, H. R., 1980. Methode der finiten Elemente. B. G. Teubner Stuttgart.
- [65] Allen, A., L. A. Sellers, and M. K. Bennett, 1987. The Gastric Mucosal Epithelial Barrier: Role of Mucus and Fibrin. *Scandinavian Journal of Gastroenterology* 22:6–13.
- [66] Taylor, C., A. Allen, P. W. Dettmar, and J. P. Pearson, 2004. Two rheologically different gastric mucus secretions with different putative functions. *Biochimica et Biophysica Acta* 1674:131–138.
- [67] Taylor, C., K. I. Draget, J. P. Pearson, and O. Smidsrød, 2005. Mucous Systems Show a Novel Mechanical Response to Applied Deformation. *Biomacromolecules* 6:1524–1530.

- [68] Kilcoyne, M., J. Q. Gerlach, M. Kane, and L. Joshi, 2012. Construction of a Natural Mucin Microarray and Interrogation for Biologically Relevant Glyco-Epitopes. *Analytical Chemistry* 84:3330–3338.
- [69] Murgia, X., P. Pawelzyk, U. F. Schaefer, C. Wagner, N. Willenbacher, and C.-M. Lehr, 2016. Size-Limited Penetration of Nanoparticles into Porcine Respiratory Mucus after Aerosol Deposition. *Biomacromolecules* 17:1536–1542.
- [70] Lafitte, G., O. Soderman, K. Thuresson, and J. Davies, 2007. PFG-NMR Diffusometry: A Tool for Investigating the Structure and NMR Diffusometry: A Tool Purified Pig Gastric Mucin in a and Dynamics of Noncommercial for Investigating the Structure: Wide Range of Concentrations. *Biopolymers* 86:165–175.
- [71] Capitanio, M., and F. S. Pavone, 2013. Interrogating Biology with Force: Single Molecule High-Resolution Measurements with Optical Tweezers. *Biophysical Journal* 105:1293–1303.
- [72] Böge, A., 2011. Technische Mechanik. Vieweg-Verlag, 29 edition.
- [73] https://lectures.informatik.uni-freiburg.de/portal/download/.../Vorlesung_biegelinie.ppt (2010)
- [74] <http://www.chemie.de/lexikon/Vergleichsspannung.html>.
- [75] Gengenbach, T., 2012. Numerical Simulation of Particle Deposition in the Human Lungs. Ph.D. thesis, Karlsruhe Institut für Technologie Fakultät für Mathematik.
- [76] Schünke, M., E. Schulte, and U. Schumacher, 2005. Prometheus Lernatlas der Anatomie: Hals und Innere Organe. Thieme-Verlag.
- [77] Oberdörster, G., E. Oberdörster, and J. Oberdörster, 2005. Nanotoxicology: An Emerging Discipline Evolving from Studies of Ultrafine Particles. *Environmental Health Perspectives* 113:823 – 839.
- [78] Zhang, Z., C. Kleinstreuer, J. Donohue, and C. Kim, 2005. Comparison of micro- and nano-size particle depositions in a human upper airway model. *Journal of Aerosol Science* 36:211–233.
- [79] Li, Z., C. Kleinstreuer, and Z. Zhang, 2007. Simulation of airflow fields and microparticle deposition in realistic human lung airway models. Part I & II: Airflow patterns & Particle transport and deposition. *European Journal of Mechanics B/Fluids* 26:632–649 & 26:650-668.
- [80] <http://www.spektrum.de/lexikon/biologie/atemmechanik/5742>.
- [81] Hinds, W. C., 1982. *Aerosol Technology*. John Wiley & Sons.
- [82] Yu, G., Z. Zhang, and R. Lessmann, 1998. Fluid Flow and Particle Diffusion in the Human Upper Respiratory System. *Aerosol Science and Technology* 28:146–158.
- [83] Farkas, A., and I. Balashazy, 2008. Quantification of particle deposition in asymmetrical tracheobronchial model geometry. *Computers in Biology and Medicine* 38:508–518.
- [84] Liu, Y., R. So, and C. Zhang, 2002. Modeling the bifurcating flow in a human lung airway. *Journal of Biomechanics* 35:465–473.

11 List of Abbreviations

A	-	barrier thickness
α	-	anomaly exponent
b	-	width of the mucin fiber
c	-	concentration of diluted species in a fluid
d_m	-	mucus layer thickness
d_p	-	size of window, pore
D_L	-	tube diameter / characteristic dimension, length
D_0	-	diffusion coefficient (Stokes-Einstein)
D_{eff}	-	effective diffusion coefficient
Δl	-	distance between the center of the curved section (during deflection) and fiber ending
$\Delta \tau$	-	duration of discrete time step
E	-	Young's modulus
E_{Brown}	-	Brownian diffusive energy
E_{kin}	-	kinetic energy
ε_{el}	-	elastic strain
η	-	dynamic viscosity
F	-	(particle impact) force
F_{ext}	-	external force
F_{thermal}	-	thermal force
F_{Stokes}	-	Stokes force
f	-	deflection
$G^{\prime}, G^{\prime \prime}$	-	elastic, viscous modulus
g	-	Gaussian distributed random number
γ_B	-	bronchial angle
h	-	height of the mucin fiber
I_M	-	second moment of area
k_B	-	Boltzmann constant

L	-	edge size of cell cavity / distance between membranes
l	-	length of the mucin fiber
M	-	force moment
m_p	-	particle mass
mod	-	modulus function
MSD	-	mean squared displacement
μ	-	mean
μ_f	-	kinematic viscosity
N	-	number of time steps, iterations
n	-	number of observations
N_p	-	number of particles
v	-	Poisson number
p	-	statistical significance
p_{exp}	-	pore expansion
pdf	-	probability density function
p_l	-	pressure in the lung
p_M	-	permeability
R	-	hydrodynamic particle radius
r	-	reflection probability
Re	-	Reynolds number
ρ_f	-	fluid density
ρ_p	-	particle density
s	-	curved section during deflection
St	-	Stokes number
σ^2	-	variance
σ_{vM}	-	von-Mises stress
σ_{el}	-	elastic stress
T	-	absolute temperature
τ_{MC}	-	mucociliary clearance time

τ_p	-	mean passage time
τ, t, s	-	time interval, time
u	-	fluid velocity
v	-	particle velocity
w	-	deformation
ω	-	frequency
x	-	(particle) position
X, S	-	system of random variables
ξ	-	standard Gaussian noise

12 List of Tables

- 1 - Examples of particle diffusion in mucus
- 2 - Comparison of effective diffusion coefficients from experiments and simulations
- 3 - Mean passage times and diffusion coefficients for various simulation parameters, particle sizes, mucus properties, and particle coatings
- 4 - Examples of rheological parameters of mucus
- 5 - Comparison of rheological parameters of mucus from own experiments and previous studies
- 6 - Examples of CFD-simulation results of particle flow and deposition in the lung
- 7 - CFD-steps
- 8 - Velocities and kinetic energies of our CFD-simulations
- 9 - Comparison of Brownian diffusive energy, kinetic energy of inhaled particles in the lung, and the necessary deformation energy
- 10 - Comparison of Brownian diffusive energy, kinetic energy of inhaled particles at the boundary of the trachea, and the necessary deformation energy
- 11 - Diffusion coefficients from FRAP-experiments

13 List of Figures

- 1 - Microscopic images of mucus
- 2 - Barrier properties of mucus
- 3 - Diffusion types in mucus
- 4 - Diffusion variants in mucus
- 5 - Mucociliary clearance
- 6 - Representation of the mucus model
- 7 - Calculated MSD and anomaly exponent from simulated Brownian diffusion
- 8 - Relative error between numerical and analytical solutions of Brownian diffusion simulations
- 9 - Relative error versus permeability of the membranes for simulated Brownian diffusion
- 10 - Ratio of D_{eff} and D_0 from simulated Brownian diffusion
- 11 - Calculated MSD and anomaly exponent from simulated Fickian diffusion
- 12 - Relative error between numerical and analytical solutions of Fickian diffusion simulations
- 13 - Relative error versus permeability of the membranes for simulated Fickian diffusion
- 14 - Ratio of D_{eff} and D_0 from simulated Fickian diffusion
- 15 - MSD of uncoated PS-particles in sputum from CF patients from experiments and calculated by Brownian diffusion simulations
- 16 - MSD of uncoated PS-particles in sputum from CF patients from experiments and calculated by Fickian diffusion simulations
- 17 - MSD of carboxylated PS-particles in human pulmonary mucus from experiments and calculated by Brownian diffusion simulations
- 18 - MSD of carboxylated PS-particles in human pulmonary mucus from experiments and calculated by Fickian diffusion simulations
- 19 - MSD of PEGylated PS-particles in human pulmonary mucus from experiments and calculated by Brownian diffusion simulations
- 20 - MSD of PEGylated PS-particles in human pulmonary mucus from experiments and calculated by Fickian diffusion simulations
- 21 - pdf of uncoated PS-particles in sputum from CF patients from experiments and calculated by Brownian diffusion simulations

- 22 - pdf of uncoated PS-particles in sputum from CF patients from experiments and calculated by Fickian diffusion simulations
- 23 - pdf of carboxylated PS-particles in human pulmonary mucus from experiments and calculated by Brownian diffusion simulations
- 24 - pdf of carboxylated PS-particles in human pulmonary mucus from experiments and calculated by Fickian diffusion simulations
- 25 - pdf of PEGylated PS-particles in human pulmonary mucus from experiments and calculated by Brownian diffusion simulations
- 26 - pdf of PEGylated PS-particles in human pulmonary mucus from experiments and calculated by Fickian diffusion simulations
- 27 - Cell-window model of mucus
- 28 - Cell-array model of mucus
- 29 - Concentration profile from simulations, using the cell-window model
- 30 - Time-dependent difference of concentration from simulations, using the cell-window model
- 31 - Concentration profile and MSD from simulations, using the cell-window model with two windows
- 32 - Concentration profile and MSD from simulations, using the cell-window model with five windows
- 33 - MSD for various window sizes from simulations, using the cell-window model
- 34 - Time-dependent concentration profiles from simulations, using the cell-array model (gradient of diffusion coefficient only in diffusion barrier)
- 35 - Time-dependent concentration profiles from simulations, using the cell-array model (gradient of diffusion coefficient in diffusion barrier and cells)
- 36 - MSD from simulations, using the cell-array model
- 37 - Ratio of D_{eff} and D_0 for various window sizes and permeability of the membranes from simulations, using the cell-window model and the model, based on permeable membranes, respectively
- 38 - MSD and the difference of concentration from Fickian diffusion simulations
- 39 - MSD and the difference of concentration from Brownian diffusion simulations
- 40 - G' and G'' in the frequency sweep
- 41 - G' and G'' at a frequency of 1 Hz
- 42 - G' at a frequency of 1 Hz with optical tweezer
- 43 - Optical trap displacement

- 44 - Output response of microbeads
- 45 - Schematic view and sketch of mucin fiber deformation
- 46 - Von-Mises stress profile with prescribed deformation in the x-direction
- 47 - Von-Mises stress with prescribed deformation in the x-direction
- 48 - Von-Mises stress profile with prescribed deflection in the y-direction
- 49 - Von-Mises stress with prescribed deflection in the y-direction
- 50 - Structure of the human lung
- 51 - Velocity profile and structure of the symmetrical lung model
- 52 - Velocity profile and structure of the asymmetrical lung model
- 53 - Velocity profile and structure of the mucus layer model of the lung
- 54 - Velocity profile in the larynx and trachea
- 55 - Velocity profile in the upper bronchia
- 56 - Velocity profile in the lower bronchia
- 57 - Averaged velocity and boundary velocity in the trachea of the mucus layer model
- 58 - Microscopic images of particles in mucus
- 59 - Scaffold for fluorescence measurements
- 60 - Normalized fluorescence intensity of regions 1-5
- 61 - Normalized fluorescence intensity of regions 14 and 15

14 List of Equations

- 1 - Probability density function
- 2 - Diffusion coefficient from Stokes-Einstein relation D_0
- 3 - Variance
- 4 - MSD_{1D}
- 5 - MSD_{pdf}
- 6 - MSD at $\tau \rightarrow 0$
- 7 - MSD_L
- 8 - Effective diffusion coefficient D_{eff}
- 9 - MSD_{app}
- 10 - Anomaly exponent α
- 11 - Langevin-equation
- 12 - Stokes force
- 13 - Thermal force
- 14 - Smoluchowski-approximation
- 15 - Euler-Maruyama method
- 16 - Robin boundary condition
- 17 - Modified iteration scheme
- 18 - $\Delta x_{k,r}$ with modulus-function
- 19 - MSD_{anal}
- 20 - Mean passage time
- 21 - 2nd Fickian law
- 22 - MSD_c
- 23 - General deflection equation
- 24 - 2nd moment of area
- 25 - Hooke's law
- 26 - Elastic strain
- 27 - Deflection

- 28 - Pore expansion
- 29 - Von-Mises stress
- 30 - Brownian diffusive energy
- 31 - Stokes number
- 32 - Reynolds number
- 33 - Navier-Stokes equation
- 34 - Kinetic energy

15 Publications and Presentations

- (1) Bokkasam H., *M. Ernst*, M. Günther, C. Wagner, U. F. Schäfer, and C.-M. Lehr (2016). Different macro- and micro-rheological properties of native porcine respiratory and intestinal mucus. International Journal of Pharmaceutics 510(1):1-12.
- (2) *Ernst, M.*, T. John, M. Günther, C. Wagner, U. F. Schäfer, and C.-M. Lehr (2017). A Model for the Transient Subdiffusive Behavior of Particles in Mucus. The Biophysical Journal 112:172-179.
- (3) CRS German Chapter Basel 2015: Poster Presentation
- (4) BioBarriers & CRS German Chapter Saarbrücken 2016: Poster Presentation
- (5) PBP World Meeting Glasgow 2016: Poster Presentation
- (6) RDD Phoenix 2016: Poster Presentation
- (7) Matlab-EXPO München 2016: Oral Presentation

16 Curriculum Vitae

Name: Matthias Ernst
Address: Uhlandstraße 21, 66894 Bechhofen
Phone: 06372/8033105
Mobil: 0176/26616705
E-Mail: matthias.ernst.1986@freenet.de
Nationality: german
Date of Birth: 26.03.1986
Place of Birth: Neunkirchen (Saar)
Grad. degree: Master of Science

School career:

10.2009 – 12.2011: Master of Science in bioprocess – engineering,
Technical University Kaiserslautern
Focus on bioprocess engineering
09.2006 – 09.2009: Bachelor of Engineering in process – engineering,
University of Applied Sciences Trier
Focus on bio-, environmental- und process – engineering

Practical courses

02.2011 – 04.2011: Flavex Naturextrakte GmbH/Rehlingen
02.2009 – 03.2009: Sulzer Chemtech GmbH/Neunkirchen

Career

since 01.2017: engineer at Ferchau Engineering GmbH in Ludwigshafen
01.2014 - 12.2016: Ph.D. - student at the Helmholtz - Institute of Pharmaceutical Research at the Saarland University & scientific employee at the University of Applied Science in Saarbrücken
01.2012 - 01.2014: engineer at Tebodin Peters Engineering GmbH (Bilfinger) in Ludwigshafen

17 Acknowledgements

This work was funded through PulMoS project (T/1-14.2.1.1- LFFP12/29) by Ministry of Education, Culture and Science, Saarland. Harish Bokkasam, Xabier Murgia, and Thomas John are acknowledged for their great support of planning the experimental settings and for executing most of the experiments. Marco Günther and Thomas John are acknowledged for providing me with simulation tools and for their encouragement in developing the described mathematical models and theoretical findings. Especially, Christian Wagner and Thomas John are acknowledged for valuable discussions and for their great support during the past three years. Claus-Michael Lehr, Ulrich Schäfer, and Marco Günther are acknowledged for giving me the chance to work in this very interesting field of science and for supporting me during my PhD-program.

Finally, I dedicated this work to my family and especially to my wife Simone, who always supported and encouraged me in the last three years.

Supplementary Material

MATLAB/Octave script for exemplary simulations

%% Input

L = 500e-9; % distance between permeable membranes in m

R = 100e-9; % particle radius in m

N = 10000; % number of time steps / iterations

M = 10000; % number of particles

T = 10; % total time in s

ts = T/N; % time step in s

time = ts*(0:N-1); % time in s

pM = 0.5; % permeation parameter in 1/sqrt(s)

r = 1 - pM*sqrt(ts); % reflection probability

V = 0.004; % dynamic viscosity in Pa*s

kb = 1.38e-23; % Boltzmann constant in J/K

Temp = 310.15; % absolute temperature in K

D0 = (kb*Temp)/(6*pi*V*R); % diffusion coefficient (Stokes-Einstein) in m²/s

%% simulation

x_0 = repmat(L*rand(M,1),1,N);

dx = sqrt(2*D0*ts);

xpos = x_0;

for m = 1:M

for n = 1:N-1

step = dx*randn;

xpos(m,n+1) = xpos(m,n) + step;

if mod(xpos(m,n),L) + step > L && rand < r

xpos(m,n+1) = xpos(m,n) - step + 2*L - 2*mod(xpos(m,n),L);

elseif mod(xpos(m,n),L) + step < 0 && rand < r

xpos(m,n+1) = xpos(m,n) - step - 2*mod(xpos(m,n),L);

```

end

end

end

msd = mean((xpos-x_0).^2,1); % mean squared displacement in m

Deff = msd(end)/(2*T); % effective diffusion coefficient in m^2/s

%% Output

% Create figure

figure1 = figure;

% Create axes

axes1 = axes('Parent',figure1,'YScale','log','YMinorTick','on',...
    'XScale','log',...
    'XMinorTick','on');

box(axes1,'on');

hold(axes1,'all');

% Create multiple lines using matrix input to loglog

loglog1 = loglog(time,[msd;2*D0*time;2*Deff*time],'Parent',axes1);

set(loglog1(1),...
    'DisplayName','normal diffusion with D0 and effective diffusion coefficient (r > 0)');

set(loglog1(2),'DisplayName','normal diffusion with D0 and r = 0');

set(loglog1(3),'DisplayName','normal diffusion with Deff');

% Create xlabel

xlabel('time [s]');

% Create ylabel

ylabel('MSD [m^2]');

% Create legend

legend(axes1,'show','Location','NW');

```

Calculation of micro elastic moduli from optical tweezers microbead displacement data

Calculation of the mean squared displacement (msd)

To calculate the msd from the particle trajectories, the x- and y-positions were used.

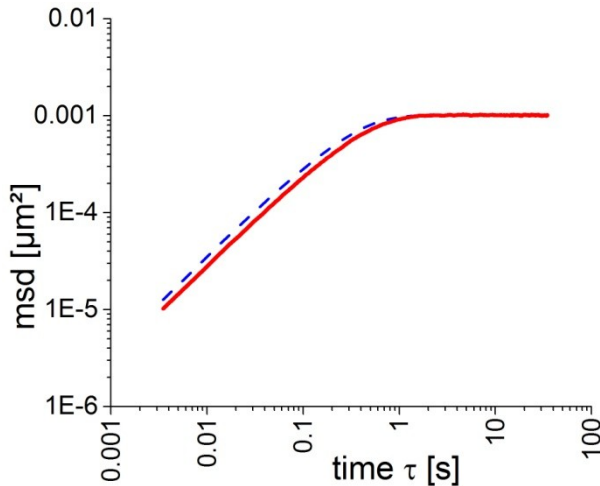


Figure S1: $\text{msd}(\tau)$ of two different trajectories (blue dashed and red solid line)

Calculation of the micro elastic modulus G'

The elastic modulus G' of the mucus in the micro scale has been calculated by using the msd at 1 sec, given by [R1]:

$$G' = \frac{k_B T}{\text{msd}(\tau) R}$$

REFERENCES

- [R1] Köster, S., Lin, Y.-C., Herrmann, H. & Weitz, D., 2010. Nanomechanics of vimentin intermediate filament networks. *Soft Matter* 6:1910-1914.